E.T.S. de Ingeniería Industrial,
Informática y de Telecomunicación

A study of super-oscillatory lenses at high frequencies using metamaterials

Máster Universitario en Ingeniería de Telecomunicación

Trabajo Fin de Máster

Santiago Legaria Lerga

Miguel Beruete Díaz y Victor Pacheco Peña

Pamplona, 29/06/2020

upna Universidad Pública de Navarra
Nafarroako Unibertsitate Publikoa

Agradecimientos

Quiero dedicar este trabajo a mis tres chicas, Ana, Carlota y Sofía, que son mi aliento y mi fuerza. Sin vuestro cariño y amor (y paciencia) no creo que me hubiese atrevido a embarcarme en esta nueva aventura.

También quiero agradecer muy especialmente a mi familia por su apoyo y confianza y por estar siempre ahí. Un recuerdo para mis amigos, que tan cariñosamente han encajado el tener que compartir su tiempo con mis estudios y otro para mis compañeros de trabajo; sois mi segunda familia. Agradezco a todos mis profesores los conocimientos transmitidos y a mis compañeros de clase los momentos vividos.

Finalmente, quiero agradecer a Miguel Beruete y a Victor Pacheco-Peña por su paciencia, por todo lo que he aprendido de ellos y, sobre todo, por su inmensa talla como seres humanos que, sin duda, ha iluminado estos años de duro trabajo.

Acknowledgments

This work is dedicated to my three girls, Ana, Carlota and Sofía, who are my breath and strength. Without your affection and love (and patience) I do not think I would have ever dared to embark on this new adventure.

I also want to especially thank my family for their support and trust and for always being there for me and my girls. Also, a very warm memory for my friends, how lovingly they have fitted having to share their time with my studies. I don´t forget my co-workers; you are my second family. I thank all my teachers for the knowledge transmitted and my classmates for all the memories.

Finally, I want to thank Miguel Beruete and Victor Pacheco-Peña for their patience, for all the things that I have learned from them and, above all, for their immense stature as human beings that have brought light and warmth to all these years of hard work.

Abstract

The first part of this work deals with the design, numerical demonstration and experimental characterization of an ultra-thin super-oscillatory lens (SOL) based on metamaterials (MTMs) at the Terahertz range, with a resolution below the diffraction limit. This SOL is binary and its two different zones are implemented using metasurface concepts with hexagonal unit cells. This way, the transparency and hence efficiency is optimized compared to the conventional transparent-opaque zoning approach that inevitably introduces a high reflection because of the opaque regions. The constructed metalens generates a sharp focal spot with a transversal resolution of $0.37\lambda_0$ ($\approx$2 times below the resolution limit) at the focal length of $14.6\lambda_0$ with relatively high enhancement.

The second part of this work seeks to combine gradient-index (GRIN) and super-oscillation (SO) concepts to improve the binary SOL. The study is carried out through an extense analytical process of optimization. The proposed super-oscillatory pseudogradient-index metalens design technique offers a new approach to match, and even improve, some of the focusing properties that are attainable in the state-of-the-art SOLs.

Resumen

La primera parte de este trabajo versa sobre el diseño, la demostración numérica y la caracterización experimental de una lente en el rango de los Terahercios, ultra-compacta y súper-oscilatoria (SOL), basada en metamateriales (MTMs) que proporciona una resolución que supera el límite clásico de difracción. Las dos zonas de esta lente binaria se implementan utilizando una metasuperficie basada en una celda unidad de tipo hexagonal. Con este enfoque se consigue mejorar la eficiencia de transmission en comparación con el tradicional uso de una máscara de amplitud basada en zonas opacas y transparentes que, inevitablemente, ofrece una alta reflexion en las zonas opacas. La metalente construida es capaz de generar un foco con una resolución transversal de $0.37\lambda_0$ (que supera por un factor $\approx$2 el límite de difracción) en la distancia focal de $14.6\lambda_0$, capaz de concentrar el campo eléctrico que incide en la lente eficientemente.

La segunda parte de este trabajo busca combinar dos conceptos, el gradiente del índice de refracción (GRIN) y las super-oscilaciones (SO) para mejorar la metalente binaria construida en la primera parte de este trabajo. Este estudio se ha basado en un intenso proceso analítico de optimización. La técnica desarrollada para diseñar una metalente superoscilatoria de índice pseudogradual ofrece un nuevo enfoque que iguala, y a veces mejora, algunas propiedades de enfocamiento con respecto a las que se pueden conseguir hoy en día con las lentes super-oscilatorias de última generación.

Key words

Metamaterials, Metasurfaces, Terahertz, metalenses, graded-index, super-oscillation, optimization, photolithography.

Index

1. Introduction and state of the art

1.1 General approach and objectives

The aim of this work is twofold: The first objective is to design, simulate and construct a super-oscillatory lens (SOL) based on metamaterials (MTMs) to enhance the transmission of these lenses usually based on opaque and transparent areas [1], [2], [3]. The design is based on the use of an advanced optimization algorithm: The binary particle swarm optimization [4]. Being our device a binary lens, we show how to design the two particles needed to obtain the required phase at its output to achieve the focusing effect. An ultrathin ($0.04\lambda_0$) MTM SOL is designed and experimentally measured, showing a good agreement with the analytical and numerical results. The manufactured metalens can generate a narrow hotspot with reduced side lobes and high enhancement.

The second part of this work seeks to combine graded-index (GRIN) and super-oscillation (SO) concepts to improve the binary SOL. The study is carried out through an extense analytical process of optimization. The proposed super-oscillatory pseudo-graded-index metalens design offers a new technique to improve the focusing properties of state-of-the-art SOLs.

1.2 Brief study of metamaterials.

The most intuitive way to begin the study of metamaterials is starting from Maxwell's equations that describe all classical electromagnetic (EM) phenomena and that are formulated (in the International System of Units (S.I.)) as follows [5]:

$$\begin{aligned} \nabla \times \boldsymbol{E} &= -\frac{\partial \boldsymbol{B}}{\partial t} \\ \nabla \times \boldsymbol{H} &= \frac{\partial \boldsymbol{D}}{\partial t} + \boldsymbol{J} \\ \nabla \cdot \boldsymbol{D} &= \rho \\ \nabla \cdot \boldsymbol{B} &= 0 \end{aligned} \tag{0.1}$$

where $\boldsymbol{E}$ denotes the electric field, $\boldsymbol{H}$ is the magnetic field, $\boldsymbol{D}$ is the electric displacement, $\boldsymbol{B}$ is the magnetic flux density, $\boldsymbol{J}$ is the free electric current density and ρ is the free charge density [6]. The region of space considered has no free electric charge ($\rho=0$) and it is also free of conduction currents ($\boldsymbol{J} = 0$). In addition, if the medium is isotropic and linear, $\boldsymbol{D}$ and $\boldsymbol{B}$ are related to $\boldsymbol{E}$ and $\boldsymbol{H}$ through the constitutive relations shown below:

$$\begin{aligned} \boldsymbol{D} &= \varepsilon_r \varepsilon_0 \boldsymbol{E} \\ \boldsymbol{B} &= \mu_r \mu_0 \boldsymbol{H} \end{aligned} \tag{1.2}$$

where ε_0 and μ_0 are the electric permittivity and magnetic permeability of vacuum, ε_r is the relative electric permittivity and μ_r is the relative magnetic permeability. These equations indicate that the response of a material to an EM wave is determined mainly by these two constitutive parameters: the permittivity and the permeability. ε describes the behavior of a material when an electric field is applied upon it and μ describes its behavior when a magnetic field is applied.

Permittivity

The permittivity is a physical parameter that describes how an electric field affects and is affected by a medium [7]. It is represented by the Greek letter "epsilon" (ε) and its Absolute value is defined as [8]:

$$\varepsilon = \varepsilon_r \varepsilon_0 \tag{1.3}$$

where ε_0 = 8,854·10^{-12} F/m. ε_r can be dependent on other parameters, such as temperature, direction of propagation (if this happens, the materials can be divided into isotropic or anisotropic, in case of presenting such dependency), frequency or mechanical stresses [9]. The relative permittivity of real materials is a complex number (they always suffer from losses) and it is expressed as follows:

$$\varepsilon_r = \varepsilon' - j\varepsilon'' \tag{1.4}$$

where ε' corresponds to the real part and ε'' corresponds to the imaginary part, and both are, in general, functions of frequency. Rigurously speaking, it must be stated that the equations described are valid for stationary state under phasorial regime. The ratio between the two components is usually denominated as loss tangent:

$$\tan\delta = \frac{\varepsilon''}{\varepsilon'} \tag{1.5}$$

The real part of the permittivity, or dielectric constant, represents a relative measure of the density of EM energy which is stored inside the material. The minimum value ε' can adopt is ε'=1, which corresponds to the vacuum. Its value depends on many different factors: density, humidity, temperature, composition, microstructure, or frequency.

The imaginary part of the permittivity, ε'' or loss factor, is a measure of how dissipative the medium is, that is, it gives an idea of how much the energy of the wave can be attenuated when it propagates through the material. There are two loss mechanisms included in this term:

$$\varepsilon'' = \varepsilon_b + \frac{\sigma}{\omega} \tag{1.6}$$

the first term represents the dielectric losses due to friction and the second are the conduction losses that appear by the movement of free charge carriers, whose magnitude is represented by conductivity σ. For materials with high conductivity, the first term can be neglected.

The air has a relative dielectric constant of about 1.0006, and although most media typically have a relative dielectric constant greater than 1, it is not unusual to observe extreme values of permittivity, for example, in frequencies close to resonance in dispersive mediums.

Permeability

Magnetic permeability is a physical parameter that describes how a material affects and is affected by a magnetic field [10]. It is called with the Greek letter "mu" (μ) and its absolute value defined as:

$$\mu = \mu_r \mu_0 \tag{1.7}$$

where μ_o =4π·10^{-7} H/m. Alike the permittivity, the permeability may be dependent on other parameters, such as temperature, frequency, or direction of propagation [11].

The relative permeability of many materials is a complex number and is expressed as follows:

$$\mu_r = \mu' - j\mu'' \tag{1.8}$$

where μ'corresponds to the real part and μ''corresponds to the imaginary part. The ratio between the two components defines the tangent of losses as:

$$\tan\delta_\mu = \frac{\mu''}{\mu'} \tag{1.9}$$

The real part of the permeability is called elastic magnetic permeability and gives an idea of the magnetic energy that is stored in a material. As noted above, it can be frequency dependent. The imaginary part of the permeability represents the magnetic losses due to various processes such as magnetic currents, hysteresis or viscosity and it is known as magnetic permeability loss factor.

Approaching the concept of metamaterials

Equations (1.1) and (1.2) summarize the whole classical theory of electromagnetics. Given a linear, isotropic and homogeneous without sources ($\boldsymbol{J}$ = ρ = 0), the wave equation (equation 1.10) can be obtained by applying the rotational on both sides of Faraday's law, substituting this result in Ampere's law and finally applying the rotational of the rotational of a field vector:

$$\nabla^2\mathbf{E} - \mu\varepsilon\frac{\partial^2\mathbf{E}}{\partial t^2} = 0 \tag{1.10}$$

Assuming a sinusoidal variation of the field, the solution of this equation is a linear combination of terms of the form:

$$\mathbf{E} = \mathbf{E}_0\cos(kr - \omega t) \tag{1.11}$$

Each of these terms corresponds to a plane wave of angular frequency ω propagating at a speed $v = (\mu\varepsilon)^{-1/2}$ (velocity of light for the medium) in the direction given by the wavenumber k (being vector $\boldsymbol{k} = k\vec{k}$, the wave vector). Introducing solution (1.11) into the wave equation (1.10) the well-known dispersion relation can be obtained [12]:

$$k^2 = \frac{\omega^2 n^2}{c^2} \tag{1.12}$$

Where c accounts for the light speed in vacuum. This equation relates the frequency ω (in rad/s, in accordance with the S.I.) of a monochromatic wave with its wave number k. The refractive index n of a medium is defined as follows:

$$n = \frac{c}{v} = \sqrt{\frac{\varepsilon}{\varepsilon_0}\frac{\mu}{\mu_0}} \tag{1.13}$$

For most materials $\mu=\mu_0$, so n is just the square root of the relative permittivity. The refractive index of a given medium has the physical meaning of the quantity by which c must be divided to obtain the effective velocity of a plane wave propagating in that medium.

Most of the materials that can be found in nature [13] have values of permittivity (ε) and permeability (μ) larger than the free-space values (ε_0, μ_0). For example, common dielectrics have a dominant electric response, exhibiting a finite value of relative electric permittivity larger than one and a relative magnetic permeability equal to one. These EM properties are the result of the macroscopic material response to EM waves due to its microscopic structure (molecules and atoms).

The idea behind MTMs is to tailor a periodic structure of unit cells (or meta-atoms or metamolecules, analogues to the natural atoms or molecules) which are much smaller than the wavelength of the incident EM wave, to obtain the desired macroscopic response of the structure (Fig. 1.1). These artificially engineered subwavelength particles have a specific geometry and are made of natural materials. Since the size of meta-atoms is smaller than wavelength, the EM wave "sees" a continuous medium and its response is defined by the periodic structure of the meta-atoms. Therefore, these artificial materials show EM properties that overcome the limits imposed by natural materials, making possible to tailor the constitutive parameters at will, even achieving extreme parameters such as close to zero or even negative values [14].

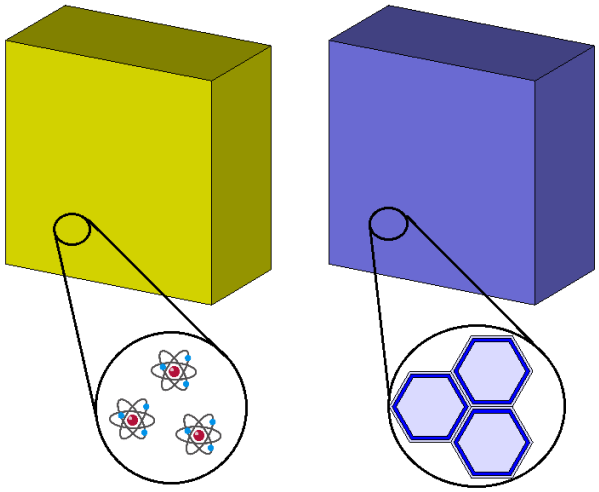

Figure 1.1. The analogy between normal materials (left) which are made of atoms and metamaterials (right) which consist of an array of engineered atom-like structures.

As the operating wavelength is large compared to the meta-atoms, the medium made with MTM is virtually homogeneous for the operating wavelength and the microstructure can be related to μ_{eff} and ε_{eff}. That is: if we assume that the structure is on a scale much shorter than the

wavelength of incident wave, the response can be homogenized and one can speak of an average value for all the fields [15].

In 1968, Veselago [16] conducted a theoretical study of substances having negative permittivity and permeability, corresponding to negative refractive index. Such substances are referred to as 'left-handed' substances as opposed to normal 'right-handed' substances having positive refractive index (the reasons for this notation are explained below).

Following this classification, materials can be divided into different classes depending on their EM properties [13], [17]: a) double positive (DPS) or right-handed media (RHM), b) double negative (DNG) or left-handed media (LHM), c) negative permeability (MNG) media, d) negative permittivity (ENG) media, and e) epsilon-near-zero (ENZ) and mu-near-zero (MNZ) media. A general classification of materials is presented in Fig. 1.2, where μ and ε are used as y and x axis respectively:

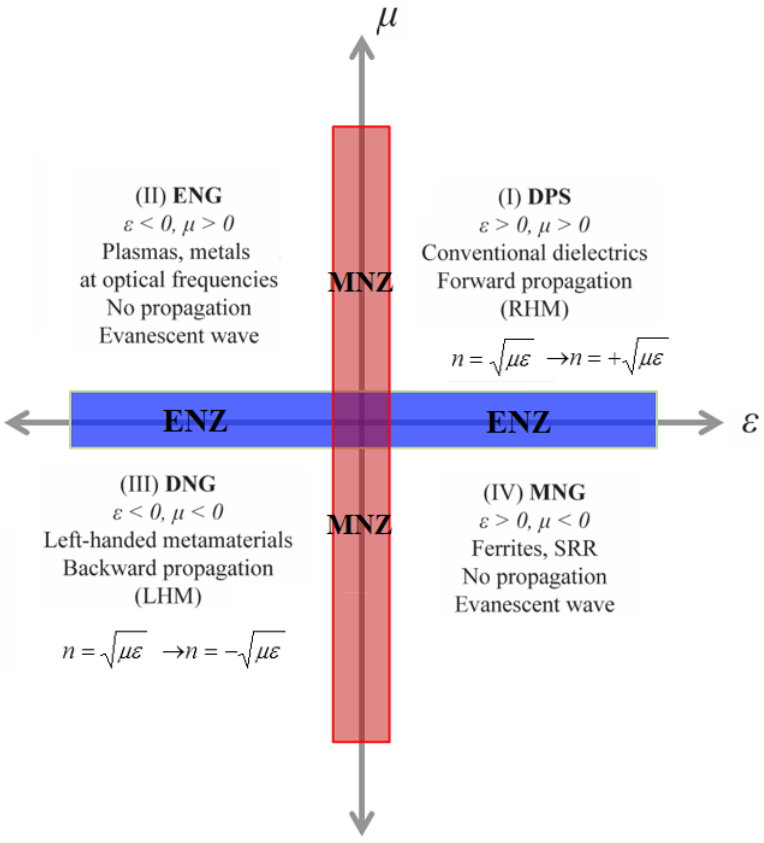

Figure 1.2. Classification of materials based on the values of the constitutive parameters. Based on a figure by Pacheco-Pena ("Pacheco-Pena V 2016 Metamaterials and Plasmonics Applied to Devices Based on Periodic Structures at High Frequencies: Microwaves, Terahertz and Optical Range (Pamplona: Public University of Navarra)".

Double-positive media (DPS)

In DPS media $\varepsilon > 0$ and $\mu > 0$ and thus the index of refraction is positive, $n > 0$. In these materials, the energy (defined upon the pointing vector $\boldsymbol{S}$) propagates in the same direction as the wave vector $\boldsymbol{k}$. In DPS media, the electric ($\boldsymbol{E}$), magnetic field ($\boldsymbol{H}$) vectors and $\boldsymbol{k}$ form a right-handed triplet so DPS are called right-handed media. Most of the dielectrics available in nature can be grouped in this category.

In practice, a wave will propagate through two or more media with different values of *n*. The behavior of the wave at the interface of materials that exhibit different but positive refractive indexes can be described by the well-known Snell's law:

$$n_1 \sin(\theta_1) = n_2 \sin(\theta_2) \tag{1.14}$$

where the pairs (n_1, θ_1) and (n_2, θ_2) are the refractive indexes and angles of the waves in the media 1 and 2, respectively. When a wave propagates from a medium 1 with $n_1 < n_2$ (see Fig. 1.3(a)), it arrives at the interface with an angle (θ_1) and is refracted with angle θ_2 when it enters medium 2, due to the different refractive index. Note that $0 < \theta_2 < \theta_1$. This is because the wavelength inside a medium with a higher refractive index is smaller than the free space wavelength; this implies that the waves will propagate with a lower phase velocity than in free space. For the case when $n_1 > n_2$ a similar behavior is obtained. The only difference is that $\theta_2 > \theta_1$. This behavior has been widely applied in the design of lenses using natural dielectrics [18], [19].

Double-Negative Media (DNG)

In DNG materials $\varepsilon < 0$ and $\mu < 0$, ***E***, ***H*** and ***k*** form a left-handed triplet and ***S*** and ***k*** point in opposite directions. Therefore, the energy flows in the opposite direction to the phase propagation. These media are also called left-handed media [16], negative-index materials (NIM), backward wave media or negative refractive index media (NRI). They were first proposed in 1968 by Veselago, when he studied theoretically the properties of this materials [16]. He predicted that such media would have negative index of refraction and multiple unconventional effects, such as reverse Snell's law, reverse Cerenkov radiation and reverse Doppler Effect. The reverse Snell's law results in the curious phenomenon of negative refraction, which occurs between a RHM and a LHM and is shown in Fig. 1.3 (b).

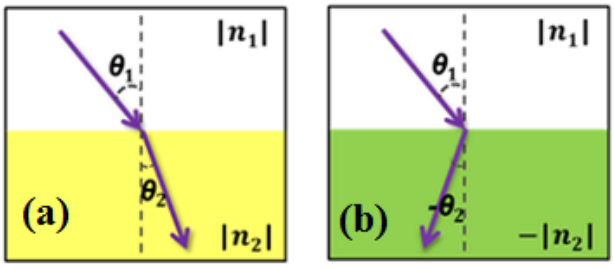

Figure 1.3. Schematic representation of the Snell's law when the first medium is RHM and the second one is RHM (a) or LHM (b). Figure by Pacheco-Pena ("Pacheco-Pena V 2016 Metamaterials and Plasmonics Applied to Devices Based on Periodic Structures at High Frequencies: Microwaves, Terahertz and Optical Range (Pamplona: Public University of Navarra)".

This fascinating property enables the possibility of building a NIM planar lens, which was later found by Pendry to act as a perfect lens [20] when both $\varepsilon = \mu = -1$. The term "perfect lens" refers to an ability of a NIM slab to restore the image with unlimited resolution, which is not possible with conventional lenses. The explanation of such captivating performance lies in the fine details contained in the evanescent components of a wave emitted by a source, which are lost in conventional lenses but amplified in a NIM slab [13], [20].

Epsilon-negative media (ENG)

In ENG media $\varepsilon < 0$ and $\mu > 0$. Therefore, the wave vector $\boldsymbol{k}$ is imaginary, and the waves are evanescent. One of the examples of metamaterials with negative permittivity is a wire medium or a metal close to its plasma frequency [21].

Mu-negative media (MNG)

This type of media has $\varepsilon > 0$ and $\mu < 0$. Analogously to ENG the wave vector $\boldsymbol{k}$ is imaginary and, therefore, fields decay exponentially, forbidding propagation of EM waves. In nature, certain ferrites and some gyrotropic materials can exhibit negative permeability. In the field of metamaterials, the most widely used elementary particle for $\mu < 0$ is the Split Ring Resonator (SRR) [13].

ENZ and MNZ

Looking at equation 1.10, it is clear that if permittivity or permeability are close to zero the wave equation becomes $\nabla^2 E = 0$, which is a static version of the usual wave equation; moreover, the velocity of light inside an ENZ or MNZ medium becomes very high and thus the propagation constant, β, is very low (being $\beta = \omega\sqrt{\mu\varepsilon}$). Consequently, the wavelength is very large and the waves propagating through the ENZ media show, fundamentally, a uniform phase for the entire propagation distance.

Designing MTMs

From the point of view of implementation, metamaterials are usually synthesized by embedding a periodic array of small artificial inclusions at a sufficiently electrically small mutual distance in a specified host medium [22]. Therefore, the design parameters in the synthesis process of a metamaterial (such as the shape, arrangement or alignment of the inclusions) provide a large collection of independent parameters (or degrees of freedom) to engineer an artificial material with a specific controllable EM response different from that obtained by its constitutive materials [22]. The designs found in this work will rely mainly on metamaterials whose unit cell is a ring slot subtracted from a square or hexagonal metal cell deposited over a dielectric of the same shape. These resonant structures allow controlling the effective index of refraction varying certain parameters inside the unit cell; this is basic for focusing purposes, as it will be explained later.

1.3 An overview of lenses

The conventional spatial resolution limit is defined as the minimum distance that allows distinguishing two point-source objects close to each other. This resolution limit, or diffraction limit, is expressed following diverse criteria that differ on the definition they use for "two objects being resolvable from each other", although the differences are usually small.

Due to the diffraction of EM waves, the resolution of conventional focusing systems is restricted to a basic theoretical limit. In 1873, Ernst Abbe discovered a fundamental 'diffraction limit' in optics [23]: whenever an object is imaged by an optical system, such as the lens of a

camera, fine features are permanently lost in the image. For EM waves with a wavelength of λ, in a homogeneous lossless medium with refractive index n, the propagation of light acts as a linear system that filters out all components for which the spatial frequency exceeds n/λ within a distance of several wavelengths. The loss of information (and thus, the limited optical resolution) arises because light emerging from the object's fine features carries components with high spatial frequencies, that is, evanescent waves that decay exponentially, resulting in an imperfect image.

The Abbe diffraction limit given by a lens under scalar field approximation is shown in Equation 1.15, where *NA* (numeric aperture) is calculated from $n\sin\theta$; n is the refractive index between the object and the lens and λ is the wavelength in that medium; the angle θ is related to the focal length *FL* and the external radius of the lens, r_i, through the equation $\tan(\theta) = r_i/FL$. The Rayleigh criterion for the resolution limit is shown in Equation 1.16.

$$res = \frac{0.5\lambda}{NA} = \frac{0.5\lambda}{n\sin(\theta)} \tag{1.15}$$

$$res = \frac{0.61\lambda}{NA} = \frac{0.61\lambda}{n\sin(\theta)} \tag{1.16}$$

Where *res* is the Rayleigh or Abbe resolution limit. For instance, considering a design with r_i = 24.85mm and *FL* = 10mm, the Rayleigh criterion for the diffraction limit would be $res = 0.66\lambda_0$. The Rayleigh criterion will be used in this work as the standard definition of the conventional diffraction limit.

Nowadays, researchers have found many different means to overcome this restriction. To name a few: a) near-field optical-scanning microscopes [24] retrieve higher frequency components from evanescent waves, using probes within a distance of less than one wavelength from the objective surface; b) combined use of dielectric microspheres on sample surfaces and a conventional microscope [25]; c) hyper-lenses, based on anisotropic metamaterials [26] that convert evanescent waves into propagation waves with high wave-numbers; d) structured light illumination microscopes (SLIMs), based on the angular spectrum theory, for which the use of spatially modulated light shifts the high-frequency components of evanescent waves to low-frequency components. Recently, the concept of super-oscillation has been theoretically and experimentally proven able to provide an alternative way to achieve contactless optical superresolution in the far field.

1.3.1 The super-oscillatory lens

Formally, a SOL is a structured lens with the ability to achieve subwavelength focusing [27], providing two major advantages: (i) far-field super-resolution without near-field evanescent waves, and (ii) it is a planar focusing device, facilitating its integration in compact systems. The key feature of the superoscillatory functions is that, although they are "band-limited", they can oscillate at a much higher rate than the highest Fourier component. This can be better understood with the example shown in Fig. 1.4. There, it is observed that in a very narrow zone, the super-oscillating function *f(x)* oscillates at a frequency almost 9 times higher (n = 43.6) than its highest Fourier component (n = 5), where n in this case is an integer accounting for the index of the different Fourier harmonics.

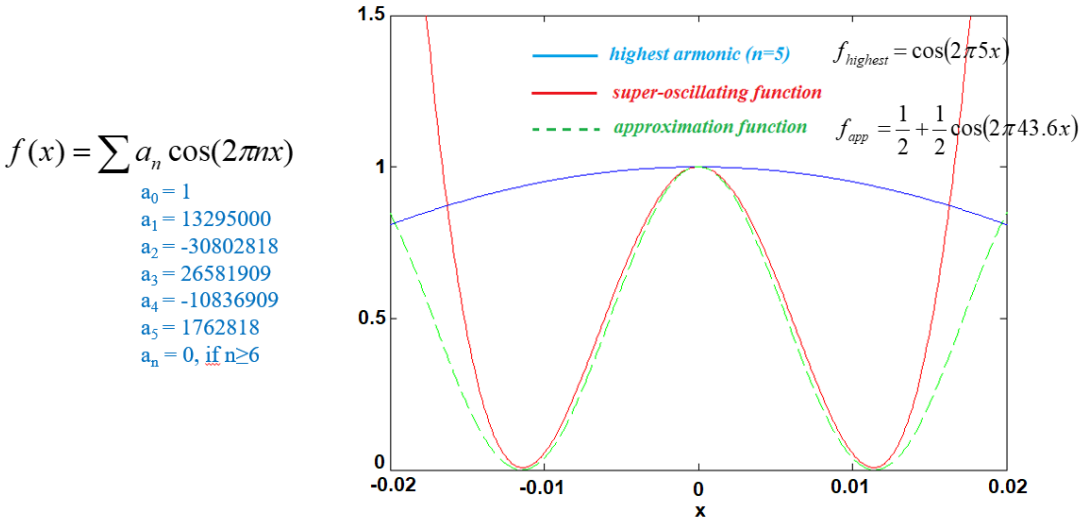

Figure 1.4. Example of a super-oscillatory function, *f (x)*, in red. Its highest harmonic fhighest (*n* = 5) is represented in blue. In a narrow interval around *x* = 0, *f (x)* is approximated by the function f_{app}. Extracted from "Legaria, S.; Pacheco-Peña, V.; Beruete, M. "Super-Oscillatory Metalens at Terahertz for Enhanced Focusing with Reduced Side Lobes". Photonics 2018, 5, 56."

Superoscillation phenomenon allows the formation of arbitrarily small optical features, which can be used for superresolution focusing and imaging. For EM waves, superoscillations correspond to local spatial frequencies (the gradient of the phase distribution) that exceed the wavenumber, and that are associated with phase singularities [28]. In fact, one characteristic of the optical super-oscillatory field is the sharp phase change at the zero E-field amplitudes [29].

To illustrate this, let the electric field $\boldsymbol{E}$ be described by equation 1.17, where vectors $\boldsymbol{A}$ and $\boldsymbol{\phi}$ denote the amplitude and phase, respectively, at each point of the space.

$$\boldsymbol{E} = \boldsymbol{A}e^{i\emptyset} \tag{1.17}$$

The above expression can be substituted into the well-known Helmoltz equation, obtaining the set of equations 1.18 and 1.19 (*k* denoting the wavenumber, as stated before):

$$\begin{cases} \nabla^2\emptyset + \nabla(ln\boldsymbol{A}^2)\nabla\emptyset = 0 & (1.18) \\ \nabla^2\boldsymbol{A} + [k^2 - |\nabla\emptyset|^2]\boldsymbol{A} = 0 & (1.19) \end{cases}$$

The local wavenumber, k_{local}, is derived from the gradient of the phase distribution, $\nabla\emptyset$. When the magnitude of k_{local} ($|\nabla\emptyset|$) is much bigger than *k*, the electric field amplitude $\boldsymbol{A}$ suffers a fast decay (see Equation 1.19) in the neighbouring area that leads to the formation of super-oscillatory features. Thus, a superoscillatory field is identified by phase singularities with large local wavenumbers.

The electric field emerging from a SOL can be characterized by different parameters. A relation of them is represented in Fig. 1.5 and listed below:

a) The focal full width at half maximum (*FWHM*), to define the hotspot size.

b) The enhancement which is a measure of how much the SOL magnifies the magnitude of the electric field at the focal point compared to free-space propagation.

c) *NLPS*, which is the ratio between the intensity peak (I_{peak}) and the maximum sidelobe (I_{sl}).

d) The field of view (*FOV*), usually defined as the distance from the hotspot in which the intensity is $0.25I_{peak}$.

e) The sideband ratio (*SBR*), defined as the ratio between the peak intensity of the main sidelobe within the *FOV* (I_{sl}) and the peak intensity of the maximum sidelobe outside the FOV (I_{sb}).

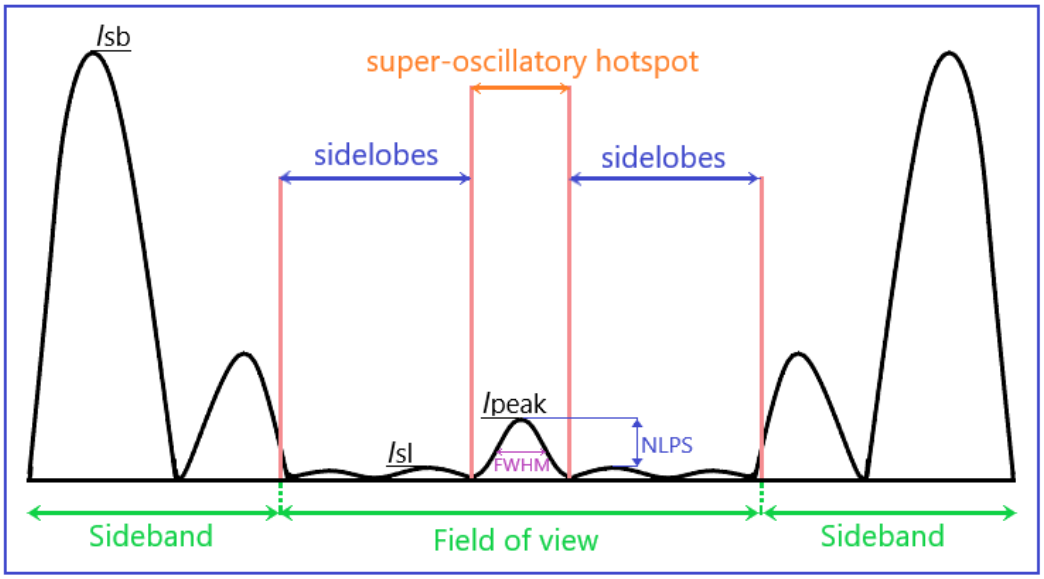

Figure 1.5. Intensity profile of a super-oscillatory focal spot. The distribution is divided into the FOV (super-oscillatory spot and sidelobes) and the sideband area. I_{peak} is the intensity of the super-oscillatory hotspot. I_{sl} is the peak sidelobe level. I_{sb} is the maximum sideband level.

An optimal SOL performance requires minimizing the *FWHM* and *SBR* while at the same time attaining the highest enhancement, *FOV* and *NLPS* possible. In most cases tradeoffs must be made among these parameters, specially when the *FWHM* becomes lower.

Summarizing, superoscillation is a phenomenon in which a signal that is globally band-limited can contain local segments that oscillate faster than its fastest Fourier components. It is well known that the superoscillation in optics is one kind of destructive interference between different beams of light at a limited local range [27]. This implies that one can control the optical superoscillation by precisely tailoring the interference of a large number of beams diffracted from a radial structured mask, as shown in [27].

Traditionally, a SOL is made up of many concentric rings either opaque or transparent (thus, the transmission amplitude is either 0 or 1). One example is related to the first experimental observation of optical superoscillation, that consisted in a metallic hole array acting as a binary amplitude mask [30]. In fact, most of the early studies on superoscillary devices are based on binary amplitude masks because of their robustness and ease of fabrication.

Although there are several other design methods to implement SOLs, all of them can be basically divided into procedures based on optimization and optimization-free approaches.

Among optimization algorithms, the particle swarm optimization (PSO) is one of the most widely used. The algorithm flow starts setting the parameters of the goal electric field (*FWHM, NLPS, DOF*, etc). Next a swarm of different random lenses is generated, and their diffraction pattern is calculated on the target focal plane. The actual difference between the calculated diffraction pattern and the goal field represents the fitness value assigned to each lens. Each iteration ends when the lenses are updated according to its fitness value. This procedure is repeated until the fitness reaches a fixed value or the maximum number of iterations is attained. It is true that using an optimization approach, SOLs can be designed without fully understanding the physics involved and that the PSO can fall into a local solution which is not the global optimal one. This can be alleviated using random mutations in some of the lenses under optimization or combining the PSO with the Genetic Algorithm (GA) [31].

The optimization-free designs are based on describing the super-oscillation optical field as the linear combination of band-limited functions. In the literature there are different set of analytical functions that show a super-oscillatory behavior. One of the better-known families are the prolate spheroidal wavefunctions (PSWFs) [32], that enable the synthesis of arbitrarily tight hotspots by linear superposition at the expense of a dramatic reduction of its confined energy. The corresponding superoscillatory transmission mask is obtained by reverse propagation using the scalar angular spectrum method [33].

One of the most important challenges today is the efficiency: When the spot size gets sharper, the efficiency decreases exponentially. In all the reported cases, the focused waves within the FOV constitute a very low percentage of the total incident energy. One way of improving the focusing efficiency is the use of phase-modulation metasurfaces. On the other hand, the large sidebands associated to small hotspots seem to be unavoidable. Although further efforts are still required to fully understand the physics behind optical superoscillation, it has already proven itself as an interesting tool for engineering far-field superresolution optical devices.

In this work, we use metamaterials to increase the transmissivity, and thus to improve the efficiency and enhancement, of a SOL. To optimize our designs, we will use different techniques: in the first part of this work we use an advanced version of the BPSO, as described in [4]. For the second part an adapted version of the GA will be used instead.

1.3.2 State-of-the-art of metamaterial-inspired lenses

Nowadays, some of the most advanced and novel lenses are based in metamaterials. Researchers from the Universidad Pública de Navarra have contributed largely to metamaterial-based lenses. Several examples are shown in Fig. 1.6.

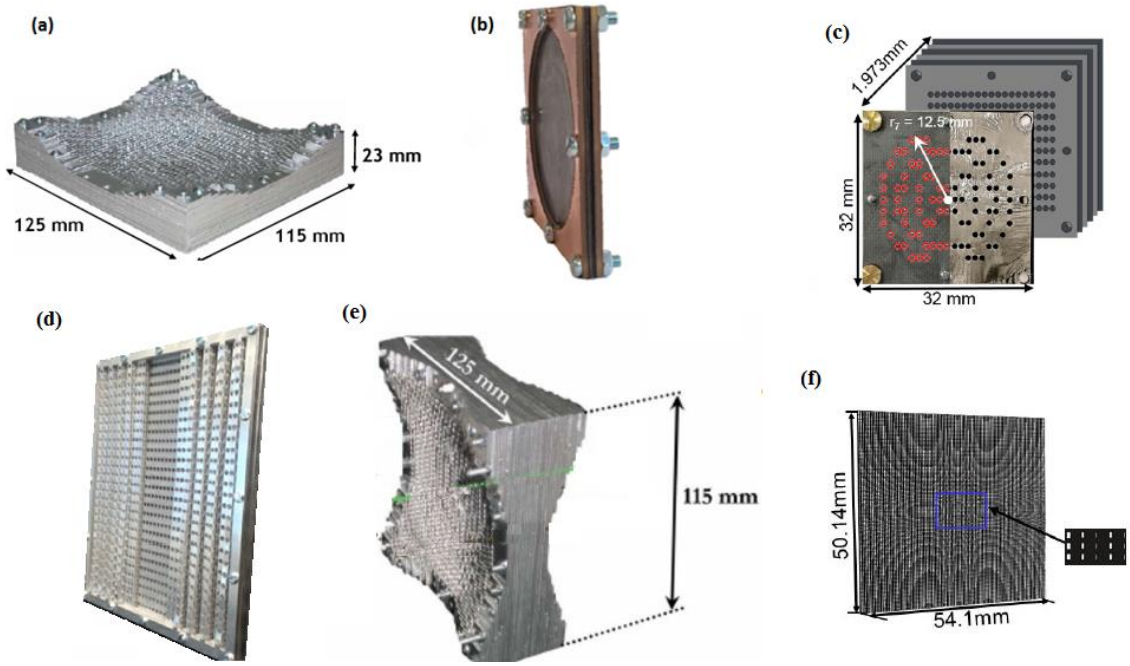

Figure 1.6. (a) Planoconcave lens based in negative refraction of stacked subwavelength hole arrays [34]. (b)Wood zone plate fishnet metalens [35]; (c) Soret fishnet metalens antenna [62]; (d) ultra-compact planoconcave zoned metallic lens based on the fishnet metamaterial [36]; (e) Converging biconcave metallic lens by double-negative extraordinary transmission metamaterial [37] and (f) full ENZ-GRIN lens [13].

The planoconcave parabolic negative index metamaterial lens (Fig. 1.6a) operates at millimeter wavelengths and both simulation and measurement results show an asymmetrical focus. The WZP lens (Fig. 1.7b) uses a fishnet metamaterial to significantly reduce the thickness of the WZPL. The experimental results show a gain of 16.6 dB at the operation frequency f = 99 GHz (k_0 = 3.03 mm) and shows good agreement between analytical, simulation and experimental results.

In the field of super-oscillatory devices, a standard SOL based on a binary amplitude mask [27] was optimized and designed at a wavelength λ = 640nm, with a focal length, $FL = 16.1\lambda$ and a radius of 62.5λ. A hotspot was generated with $FWHM = 0.29\lambda$; however, the focal spot was surrounded by a large sidelobe with almost the same intensity as the spot, which limited the *FOV* to ~0.6λ.

In another recent study [38], the authors state that increasing the number of phase and amplitude values used in the mask can improve the superoscillation focusing performance, enhancing the transmission efficiency, reducing the sidelobes and extending the FOV. This is done in the cited work introducing an additional binary phase (0 and π rads) to the amplitude mask. The measured focal spot had an average *FWHM* of 0.454λ. Sidelobes were clearly suppressed, being *NLPS* = 5.85dB. This technique of using many different phase retardation values will be explored in the second part of this work. Another example of a continuous modulation of phase and amplitude can be found in reference [39]. The authors used a periodic two-layer metallic hole array which results in a theoretically predicted FWHM = 0.319λ and low *NLPS* (≈ 5.30dB).

Some authors have explored the possibility of extending the depth of focus (DOF) of the super-oscillatory hotspots. This means that the focal spots extend along the optical axis with a transverse size that is smaller than the diffraction limit. In [40] an optical needle with an axial

length of 11λ and *FWHM*= 0.42λ was experimentally demonstrated. The design is based on a conventional binary amplitude mask in which the central area is blocked with a circular metallic disk. An alternative method to extend the DOF is the use of optimization, as shown in [41].

In Table 1.1. it is presented a summary of some reported results for super-oscillatory lenses under linear or circular polarization, collected from the review paper found in [42]:

Ref.	λ (nm)	FWHM (λ)	DL(λ)	FL(λ)	NA
[43]	532	0.6	0.63	5.26	0.79
[44]	640	0.289	0.37	16.1	1.35
[45]	532	0.271	0.33	1.88	1.507
[46]	632.8	0.454	0.64	399.5	0.78
[47]	400	0.49	0.61	100	0.82
[48]	632.8	0.379	0.513	41.9	0.976
[49]	632.8	0.406	0.534	148	0.936
[50]	365	0.319	0.50	20	0.996
[51]	632.8	0.316	0.60	21	0.83

Table 1.1 SOL reported results. *DL* represents the Abbe diffraction limit, and *NA* is the numerical aperture of the lenses.

1.4 Outline

This document has been organized as follows:

a) In Chapter 2, the full wave simulator, the technique of photolithography and the measurement system used in this work are explained.

b) In Chapter 3, different metaSOLs are carefully studied.

c) Chapters 4, 5 and 6 refer to the conclusions of this work and future lines of interest, the bibliography used and the author's merits, respectively.

2. Materials and methodology

2.1 Analytical procedures.

2.1.1 The binary swarm particle optimization

Before talking about the BPSO itself, we must introduce the Particle Swarm Optimization (PSO) algorithm; it was developed by Eberhart and Kennedy in 1995 [54] and was inspired by the behavior of a swarm of bees, a flock of birds or a bank of fish during their food-searching activities. Believed to be effective in multidimensional, linear and nonlinear problems, PSO was recently introduced into the antenna community by Robinson and Rahmat-Samii [55]. The PSO has been applied to different EM applications such as antenna pattern synthesis [56]. PSO algorithm is widely used thanks to its simplicity [57]. The different "particles" or "agents" that conform the swarm uses two principles:

a) Principle of communication: All particles communicate its positions to all others.

b) Principle of learning: Each particle learns its best position so far and move towards it.

For particle *i*, its position is denoted by X_i (a vector in the search space). For the different time steps, there is an index "*t*", $X_i(t)$, where $t = 0$ means the beginning of the algorithm. For particle *i*, its velocity is denoted by $V_i(t)$, and describes its movement and the sense of its direction. Each particle has a memory: the personal best position found, $P_i(t)$; the swarm has a best global position: $G(t)$.

The mathematical model of the PSO algorithm is very simple (see Fig. 2.1). On every iteration of PSO, position and velocity of each particle is updated according to this simple mechanism:

-The vector difference from current particle´s position to its current personal best is calculated: $Pi(t)$-$Xi(t)$.

-The vector from current particle´s position to the global best is calculated: $G(t)$-$Xi(t)$.

-The current particle´s velocity vector is also considered: $Vi(t)$.

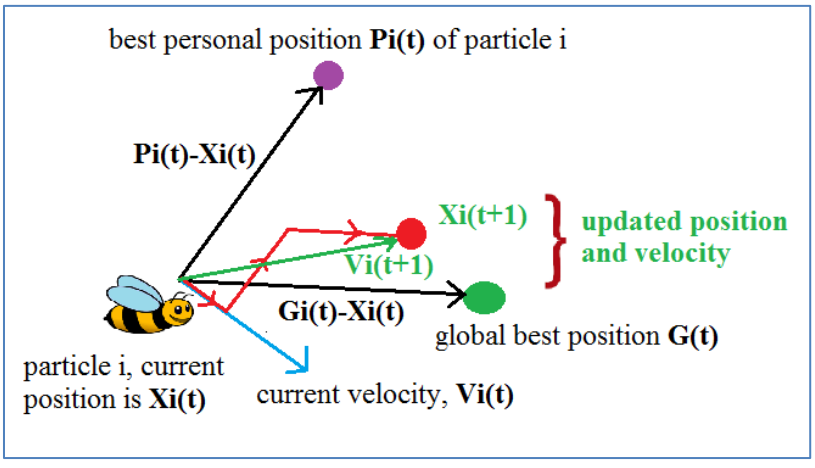

Figure 2.1. Illustration of the PSO algorithm model.

The particle will move, somehow, parallel to those three vectors towards its new updated position, denoted $X_i(t+1)$. this means that a weighted sum of the three vectors is applied to $X_i(t)$ to get the updated position. The mathematical model of motion of particles in the PSO can be described with the equations for updating the velocity $V_{ij}(t+1)$ and position $X_{ij}(t+1)$ of particles:

$$V_{ij}(t+1) = w \cdot V_{ij}(t) + r_1 \cdot C_1 \cdot (P_{ij}(t) - X_{ij}(t)) + r_2 \cdot C_2 \cdot (G_j(t) - X_{ij}(t)) \quad (2.1)$$

$$X_{ij}(t+1) = X_{ij}(t) + V_{ij}(t+1) \quad (2.2)$$

where "*j*" is the corresponding component of velocity/position, r_1 and r_2 are random uniform distributed values between 0 and 1, c_1 and c_2 are the cognitive factor and the social factor respectively, and *w* is the inertial weight.

So far, we have not considered that the solution space is a binary vector of dimension N. The velocity vector, $V_{mn}(t)$, will be a real number between $[-V_{max}, V_{max}]$. Since the particle´s position is a binary N-dimensional vector, it must be updated in an alternative manner to that in equation 2.1. In this work, we will follow the strategy followed by [4], where each particle´s velocity component (V_{mn}) is related to the possibility that each position component (X_{mn}) takes a value of 1 or 0. This is implemented using an intermediate variable, $S(V_{mn}(t))$, via the sigmoid limiting transformation.

The value of $S(V_{mn}(t))$ can be interpreted as a probability threshold, so if a random generated number between 0 and 1, $r_{mn}(t)$, is lower than $S(V_{mn}(t))$, the n_{th} bit of the m_{th} particle will be updated to 1 (and it will be updated to 0 if $r_{mn}(0,1) \geq S(V_{mn}(t))$). A summary of this updating process is shown in equations 2.3 and 2.4:

$$S(V_{mn}(t)) = \frac{1}{1+\lambda^{-Vmn(t)}} \quad (2.3)$$

$$X_{mn}(t) = \begin{cases} 1, & r_{mn}(t) < S(V_{mn}(t)) \\ 0, & r_{mn}(t) \geq S(V_{mn}(t)) \end{cases} \quad (2.4)$$

2.1.2 The genetic algorithm optimization

John Holland introduced this algorithm in 1960 based on the concept of the Darwin's theory of evolution. Afterwards, his student Goldberg extended GA in 1989 [58]. GA can be applied to a large variety of problems, including those in which the goal function is discontinuous, nondifferentiable or highly nonlinear.

The genetic algorithm (GA) is a method for solving optimization problems based on natural selection, the process that drives biological evolution. An individual solution in the GA is called a chromosome. Each chromosome typically contains a set of genes. GA repeatedly modifies a population of individual solutions by selecting individuals from the current population to be parents and deriving children from them to form the next generation. It is expected that, over successive generations, the population evolves toward an optimal solution.

The GA method uses three main types of rules at each step to create the next generation from the current population:

a) Selection rules to select the parents.

b) Mutation rules to apply random changes to individual parents to form children.

c) Crossover rules to combine two parents to form new children.

To start, GA generates a random initial population containing *nPop* chromosomes, each one of them containing a fixed number of genes, *nG*. Each of these chromosomes is evaluated according to a goal function; the chromosomes with the better fitness values are more suited to be candidates for the next population.

Next, GA operators, namely crossover and mutation, generate the next population based on the crossover percentage, *pc*, and the mutation percentage *pm*. Different selection methods can be employed: Roulette Wheel, Tournament, Random… This work uses the Roulette Wheel as the standard selection method, so a new parameter β must be defined to consider the selection pressure.

By repeating the above stages, GA terminates to a near-optimum solution. To end the algorithm, the maximum number of iterations is set. The GA can be summarized in the following steps numbered in Table 2.1:

Step 1	**Initialize randomly the value of the genes of each chromosome.**
Step 2	**Calculate the goal function value of each chromosome.**
Step 2.1	Start.
Step 2.2	Calculate goal function value, also named *cost*.
Step 2.3	Sort the population according to the goal function value.
Step 2.4	End.
Step 3	**Selection (Roulette wheel).**
Step 3.1	Start.
Step 3.2	Calculate selection probabilities of each chromosome, P_i: $$P_i = e^{-\beta \cdot cost_i / WorstCost}$$
Step 3.3	Calculate the cumulative probability vector, C_i. $$C_i = \sum_{1}^{nPop} P_i$$
Step 3.4	Generate random numbers *Ri* in the range 0-1.
Step 3.5	If ($R_i > C_i$ & $R_i < C_{i+1}$) then select parent chromosome C_{i+1}.
Step 3.6	Repeat to obtain pairs of parents, according to the *pc* value defined.
Step 3.9	End.

Step 4	**Crossover.**
Step 4.1	Start.
Step 4.2	Generate a random crossover method and apply it: -*single point crossover*: Two selected chromosomes (parents) will be cut at a crossover point and its gens will be interchanged. -*double point crossover*: There are two crossover points, defining a chromosome section, that will be interchanged between both parents. -*uniform crossover*: The children will be a linear combination of both parents.
Step 4.3	End.
Step 5	**Mutation.**
Step 5.1	Start
Step 5.2	Use mutation percentage parameter, *pm*, to obtain the number of possible mutant chromosomes, and the mutation rate, *mu*, to obtain the number of genes that will be mutated in each mutant.
Step 5.6	Mutated genes at a mutation point are replaced by new genes.
Step 5.7	Obtain new chromosome.
Step 5.8	End.
Step 6	**Continue until the fixed number of iterations is reached.**

Table 2.1. Steps involved in the Genetic Algorithm.

2.1.3 The Taguchi Method

The parameters of a meta-heuristic must be tuned to find an optimal combination of them such that the response (the goal function) is optimized. There are three main methods to calibrate parameters of meta-heuristics: (1) Fractional factorial [59], [60]; (2) response surface methodology [61]; (3) the Taguchi method [62], [63]. This work employs the Taguchi method to tune the parameters of the Genetic Algorithm.

The Taguchi method is based on 5 successive steps. First, parameters with significant effects on the response are determined. It is known that the GA parameters that have potential effects on a solution are the number of chromosomes, *nPop*, the number of iterations, *It*, the crossover percentage, *pc* and the mutation percentage, *pm*.

Second, a trial and error procedure is used to determine levels of the mentioned parameters that provide good goal function values (three different levels are considered for each parameter).

Third, an appropriate orthogonal array must be selected. While there are many standard orthogonal arrays available, each one of them is meant for a specific number of independent

design variables and levels. In the present case, to understand the effect of 4 independent factors each having 3 factor level values, the L_9 orthogonal array is the right choice, because it minimizes the simulation time.

L_9 Orthogonal array					
	Independent Variables				**Goal function Values**
Simulation #	***nPop***	***It***	***pc***	***pm***	
1	Level 1	Level 1	Level 1	Level 1	g_1i, $i = 1…n$
2	Level 1	Level 2	Level 2	Level 2	g_2i, $i = 1…n$
3	Level 1	Level 3	Level 3	Level 3	g_3i, $i = 1…n$
4	Level 2	Level 1	Level 2	Level 3	g_4i, $i = 1…n$
5	Level 2	Level 2	Level 3	Level 1	g_5i, $i = 1…n$
6	Level 2	Level 3	Level 1	Level 2	g_6i, $i = 1…n$
7	Level 3	Level 1	Level 3	Level 2	g_7i, $i = 1…n$
8	Level 3	Level 2	Level 1	Level 3	g_8i, $i = 1…n$
9	Level 3	Level 3	Level 2	Level 1	g_9i, $i = 1…n$

Table 2.2 Layout of the L_9 orthogonal array. Note that each simulation is repeated *n* times.

Fourth, the proposed design is used to carry on the different simulations.

Fifth, for a minimization problem, the Taguchi method aims to maximize the Signal to Noise Ratio (SNR) using equation 2.5:

$$SNR = -10\log_{10}\left(\frac{1}{n}\sum_{i=1}^{n} g_i^2\right) \tag{2.5}$$

Since each simulation is the combination of different factor levels, it is essential to segregate the individual effect of independent variables to find an optimal combination of them such that the response (the goal function) is optimized within the minimum possible time.

2.2 Numerical EM solver: CST Microwave Studio

CST Studio Suite® is a widely known platform to solve EM problems. One of its main features is the integration of various simulation methods. CST Microwave Studio® (CST MWS) is a simulation module inside CST Studio Suite®, and it is a dedicated 3D EM full wave simulation software of high frequency problems. It was founded in 1992 by Thomas Weiland as an evolution of the MAFIA packet software: “solving Maxwell’s equations using the Finite Integration Algorithm”, introduced in 1977, based on the Finite Integration (FIT) technique [64], [65].

CST MWS simplifies the process of creating a structure providing a graphical modeling front-end. After the model has been constructed, an automatic meshing procedure is applied before the simulation engine is started. There is the chance of choosing the simulator and/or mesh type that is best suited to each problem: CST MWS contains several solvers to best suit a given problem class (transient solver, frequency domain solver, eigenmode solver, resonant solver, integral equation solver, asymptotic solver, and TLM solver).

In this work both time and frequency domain solvers are used. The largest simulation flexibility is offered by the time domain solvers, which can obtain the entire broadband spectral response of the simulated device from a single calculation run. This solver is chosen to simulate full lens models or the different cylindrical approximation of the lenses. However, time domain solvers are less efficient for structures that are electrically much smaller than the shortest wavelength of interest. In such cases it may be advantageous to solve the problem by using the frequency domain solver, and this will be the approach to simulate the unit cells that conforms the structure of the different MTM used in the design

To solve an EM problem, the simulation domain is first divided into small cells, where Maxwell's equations are solved. The program offers different meshing options, being the main ones hexahedral and tetrahedral mesh. The hexahedral meshes can be used alone or in combination either with the perfect boundary approximation (PBA) feature, or with the thin sheet technique (TST) extension or with other algorithms that reduce the overall cell count. With the hexahedral mesh, the whole simulation domain is divided into small cubes (either of uniform or varying size). The tetrahedral meshes can be used in the frequency domain and eigenmode solvers and in this kind of meshing only the objects are divided in small tetrahedrons while the rest of the simulation domain is left unmeshed.

With both hexahedral and tetrahedral meshes, two different options can be chosen [66]: (i) Automatic mesh generation: the mesh generator creates automatically a mesh that fits the simulated structure and the EM fields; (ii) adaptive mesh refinement: the software preforms repeated simulations and evaluates different solutions, recognizing regions where the mess needs to be locally refined. Although this option increases the simulation time, it also provides improved accuracy.

Besides, CST MWS allows a parametrical description of the structure to easily change its dimensions. In general, all relevant structural modifications are recorded in the history list. The easiest way to obtain is to use the Parameter Sweep tool after. An extensive use of parameterization will be used to test the different SOL configurations/solutions obtained through optimization [66]. It is also possible to setup specific Result Templates, which allow the definition of various post processing steps which are automatically computed after each simulation run.

2.3 Experimental measurements: Photolithography and the VNA Analyzer

2.3.1 Manufacturing the super-oscillatory lens: The process of photolithography

Photolithography [67], literally meaning light-stone-writing in Greek, is the process by which patterns can be transferred into a substrate. This technique uses light to transfer a geometric pattern from a photomask to a light-sensitive chemical "photoresist" on the substrate. A series of chemical treatments then either engraves the exposure pattern into or enables deposition of a new material in the desired pattern upon, the material underneath the "photoresist".

Photolithography shares some fundamental principles with photography in that the pattern in the etching resist is created by exposing it to light, either directly (without using a mask) or with a projected image using an optical mask. This technique is used because it can create extremely small patterns (down to a few tens of nanometers in size), it affords exact control over the shape and size of the objects it creates, and because it can create patterns over an entire surface cost-effectively. Its main disadvantages are that it requires a flat substrate to start with, it is not very effective at creating shapes that are not flat, it can require extremely clean operating conditions and the mask is usually not cheap. Photolithography implies the use of a clean room.

The metasurface that implements the SOL was lithographically patterned on a 0.6 μm thick copper (Cu) layer sputtered on a polypropylene (PP) film 35 μm thick via a standard contact photolithography technique (CPhLT) as described in [68]. The main stages of PP-based CPhLT are: 1) The PP film is firmly mechanicaly fixed on the bearing glass wafer, that has outer dimensions 102×102 mm. 2) The PP film is treated with a glow discharge in argon atmosphere and then metalized by a 0.6 μm thick copper layer with a thermal vacuum deposition method. 3) A positive photoresist film 0.6 μm thick is spin coated, then air dried and finally thermaly treated at 90ºC. 4) This photoresistive layer is put in close contact with the SOL's "positive" photomask, consisting in a patterned ferric-oxide-film. 5) The photoresist is exposured to monochromatic UV radiation (λ=365 nm) through the photomask to create a latent image which replicates the micro-pattern of the photomask. 6) The latent image is chemically developed in a solution of potassium hydroxide that removes the irradiated (transparent) areas of the photoresist. 7) Afterwards, the developed photoresist is hardened by compressed air drying and thermal treatment at 120ºC, forming a firm resistive mask. 8) Through this hardened mask the Cu-layer is chemically etched. 9) The hardened resistive mask is dissolved with an organic solvent. 10) The PP film with a fabricated metalized micropattern of the SOL is separated from the glass wafer.

The metasurface dimensions were chosen from the conditions imposed by the fabrication and instrumental capabilities, as explained below:

a) The widths of metallic lines and inter-line gaps in the metasurface pattern were required to fall within the range of 10±2 μm. Our metasurface, consequently, is designed with a minimum width value of 26 μm for metallic lines and we also impose a minimal metal-free gap between metallic lines of 17 μm. Also, the metallic thickness is h_m = 0.6 μm.
b) To minimize artifacts on the periphery of the photolithographic field, it is better to work with a diameter of 50 mm or lower. The SOL radius is *r_sol* = 24.90 mm.
c) There are different PP film thickness available: 15, 20, 35, 50, 75, and 100 μm. After some numerical calculations, the dielectric thickness chosen was h_d = 35 μm.

To produce the photomask, it was necessary to prepare a txt-file with the coordinates of all the structures involved in the metasurface. The file created contains the (x,y) coordinates for all knots of the different hexagonal slots (metal-free areas) comprosing the SOL pattern. Thus, each slot is drawn as a closed polyline that is sequentially concatenated following its knots as can be seen in Fig. 2.2.

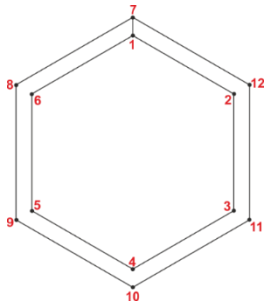

Figure 2.2. Sequentially concatenated knots that define the metal-free hexagonal slots. The polyline is defined with the sequence: 1→2→3→4→5→6→7→8→9→10→11→12→7→1.

The code to obtain the txt-file was programmed with matlab®. The binary metasurface is based on two different unit cells that can be called either type A or B. The code is straight forward: First, the center coordinates of all the unit cells are calculated. Then, depending on the distance between the center of each unit cell and the SOL optical center, each unit cell will be assigned to type A or B. The SOL photomask structure generated is composed of 18783 unit cells covering a ≈ 50 mm diameter area. A schematic view showing the manufactured meta-SOL is depicted in Fig. 2.3.

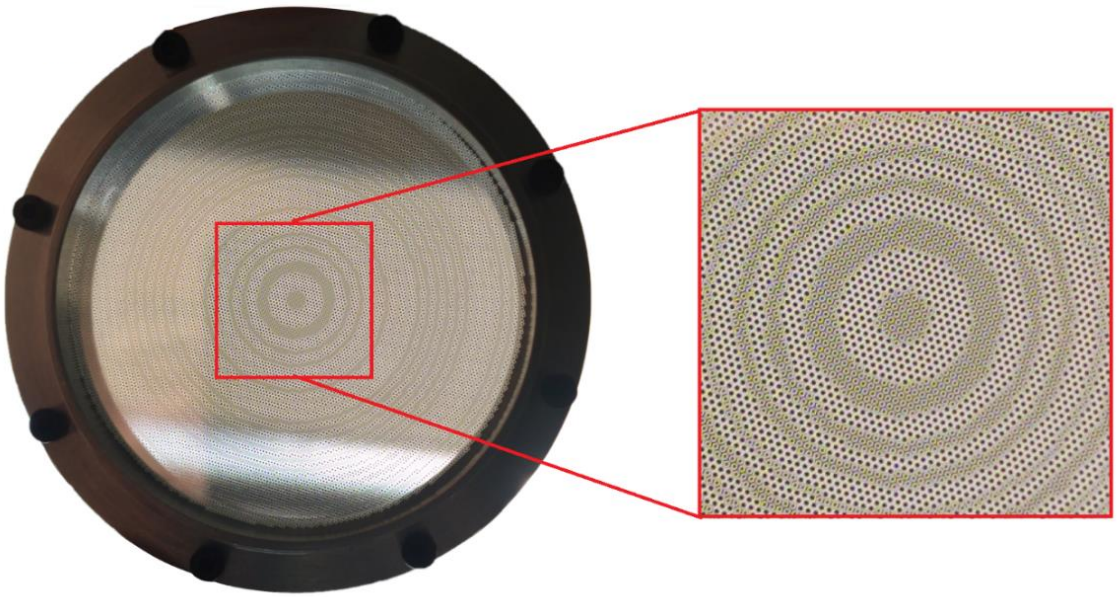

Figure 2.3. Constructed metalens tightened onto a ring-shaped aluminum holder and zoomed view.

After the CPhLT process, 3 SOL samples are obtained, being their quality good and defect-free, although for one sample there is one small imperfection because of metallization flaking (due to a large local microganule protruding from the PP surface). One of the better samples is then tightened onto a ring-shaped aluminum holder with a clear aperture diameter of 50 mm, as can be seen in Fig. 2.3d

2.3.2 Experimental setup.

The fabricated SOL was experimentally measured with the Vector Network Analyzer (VNA) available in the UPNA's THz laboratory located in the Jerónimo de Ayanz building. The VNA provides both the amplitude and phase of the transmitted and the resulting signal. The operational and logical control of the analyzer is done with a PC computer. The lens behaviour was measured in Near-Field, using 220-330 GHz probes in the configuration shown in Fig. 2.4. The source delivers power in the mW range, and it was set with an output power of 6.5 dBm; The meta-SOL was illuminated with a probe placed at a distance large enough to ensure uniform illumination. Thus, the lens was fed with quasi-planar vertically polarized radiation. An open waveguide was used as the receptor to detect the hotspot. Millimeter-wave absorbers were spread throughout the setup to mimic anechoic chamber conditions.

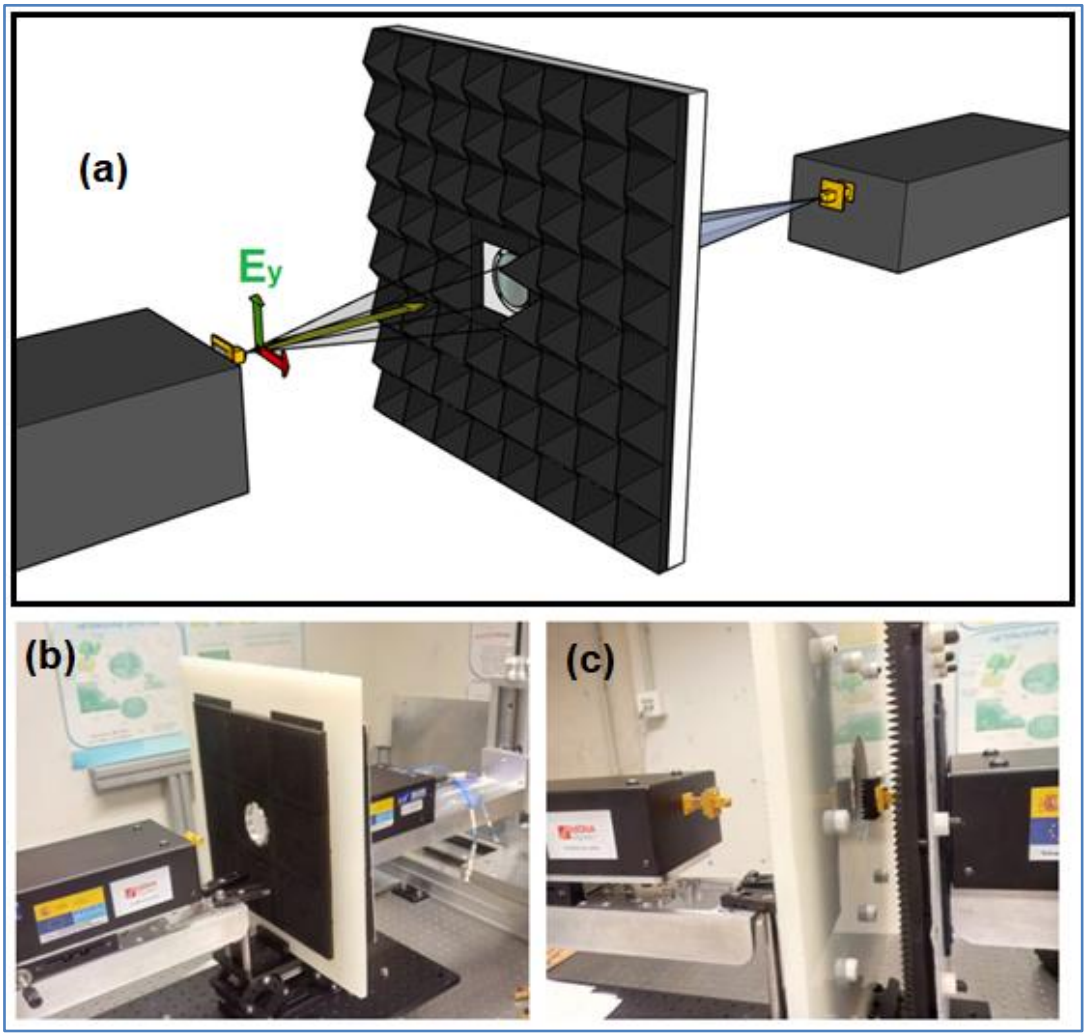

Fig. 2.4. (a) Experimental sketch: Transmitter (Vertical polarization, planewave), lens and detector. (b) and (c) Experimental setup. Both the lens and the detector are surrounded by absorbent material.

3. Results and discussions

3.1 Super-oscillatory lens.

When light passes through a lens with finite aperture, diffraction occurs, and the resulting diffraction pattern consists in a brighter region in the center along with a series of concentric rings of decreasing intensity around it. The brighter center is called the Airy Disk and the concentric rings are known as the Airy pattern. The Rayleigh criterion for resolving two source-points of light is that the center of the Airy disk for the first source occurs at the first minimum of the Airy disk of the second.

Due to diffraction, the smallest point at which a ray of light can be focused using a lens is the size of an Airy disk. An optical system in which the resolution is not limited by imperfections in the lenses but only by diffraction is said to be limited by diffraction.

Thus, for any conventional imaging instrument, the fine features of an object are permanently lost in the image due to the diffraction of light. Small details scatter light mostly into evanescent waves that exponentially decay away from the object and then cannot be captured by the device [69]. To overcome this diffraction limit, novel concepts have been proposed in the last years, such as metamaterials and metasurfaces [70–72], dielectric particles [73–75], and solid immersion lenses [76], to name a few. Within this realm, super-oscillatory devices have demonstrated their potential in imaging applications with an improved spatial resolution.

Super-oscillations were first introduced at the end of the last century to describe a phenomenon in which a band-limited signal can contain localized field variations with oscillations faster than those of the highest Fourier components of their spectrum [77], as explained in the introduction. In optics, the term super-oscillation refers to a near-destructive interference with fast phase variations and high local momenta in a small intensity region [78].

Recently, this phenomenon has been applied to improve the performance of imaging systems by implementing super-oscillatory lenses (SOLs) with subwavelength spatial resolution, defeating the diffraction limit [70,78–84].

Traditionally, SOLs are planar, multi-annular, and radial focusing devices composed of alternating transparent and opaque concentric rings, usually designed applying optimization techniques, such as genetic algorithms and vector designs [79–81]. The optical super-oscillation is controlled by tailoring the interference between the diffracted beams produced by each annular aperture [82]. The main drawback of this procedure is that it gives rise to high amplitude side lobes that reduce the intensity of the subwavelength focal spot generated at the output [78].

Moreover, even though there is no physical limit regarding the size of the focal spot along the transversal axes, it has been demonstrated that the efficiency of a SOL is dramatically reduced as the resolution is increased [83]. Thus, only a small fraction of light incident on the lens is focused on the hotspot and the largest fraction is distributed on the halo rings around the hotspot.

Since they were introduced several years ago, metamaterials (and metasurfaces as their 2D version) have opened new paths to synthesize and control wave propagation. Metamaterials have been demonstrated within a wide spectral range, from microwaves to optical frequencies, influencing other fields, like acoustics and mechanics. In particular, the field of lenses has greatly

benefited from the introduction of metamaterials and metasurfaces since the beginning of the topic.

Inspired by the features of metamaterials and metasurfaces, in this work we propose and demonstrate, both analytically and numerically, a binary SOL designed by alternating semitransparent concentric rings filled with two different metamaterial unit cells. Three objectives are pursued: (i) enhancement of the efficiency by reducing the reflection at the input and, therefore, increasing the amplitude at the focus; (ii) reducing the side lobes; and (iii) keeping a narrow focal spot below the diffraction limit.

To accomplish this, an advanced version of the binary particle swarm optimization (BPSO) algorithm, based on the method proposed [89], is developed (described in detail in Appendix A.3). The designed SOL is then implemented using only two different unit cells at the operation frequency of f_0 = 0.327 THz (λ_0= 917 μm).

As it will be shown below, an increased amplitude of the focal spot and reduced side lobes are obtained with the proposed structure, compared to conventional SOLs based on opaque–transparent zones, without affecting its performance in terms of the subwavelength resolution of the focal spot, with a width of $0.44\lambda_0$ and $0.50\lambda_0$ along the x and y axis, respectively. At the operation wavelength and at the design focal length (FL =$10\lambda_0$), the diffraction limit is $0.65\lambda_0$, considering the Rayleigh criterion.

3.1.1 Lens design and simulation results

Particle Swarm optimization has been used recently to design lenses with super resolution at optical frequencies by alternating opaque and transparent rings [90, 91, 92]. In this work, we aim at designing a metamaterial lens without using opaque plates to enhance transmission.

Only 2 particles are required because the binary PSO (BPSO) will be used. Both particles can be freely designed to obtain the required phase at the output and thus creating different optical paths for the even and odd zones. Moreover, an ultrathin metalens ($0.039\lambda_0$) is designed.

Considerations on the unit cells

As mentioned in the introduction, to create different optical paths for the even and odd zones, two different unit cells are used, see schematic in Fig. 3.1. Both are hexagonal ring slots with side length L_{hex} carved on a copper metallic film with conductivity $\sigma = 5.8\times10^7$ S/m and thickness h_m = 0.6 μm ($0.65\times10^{-3}\lambda_0$) laying on a polypropylene slab with relative permittivity ε_r = 2.25 and thickness h_d = 35 μm ($0.038\lambda_0$). Note that, for simplicity, we used the DC nominal conductivity of copper, although, in the terahertz band, this nominal value is usually lower due to granularity, etc.

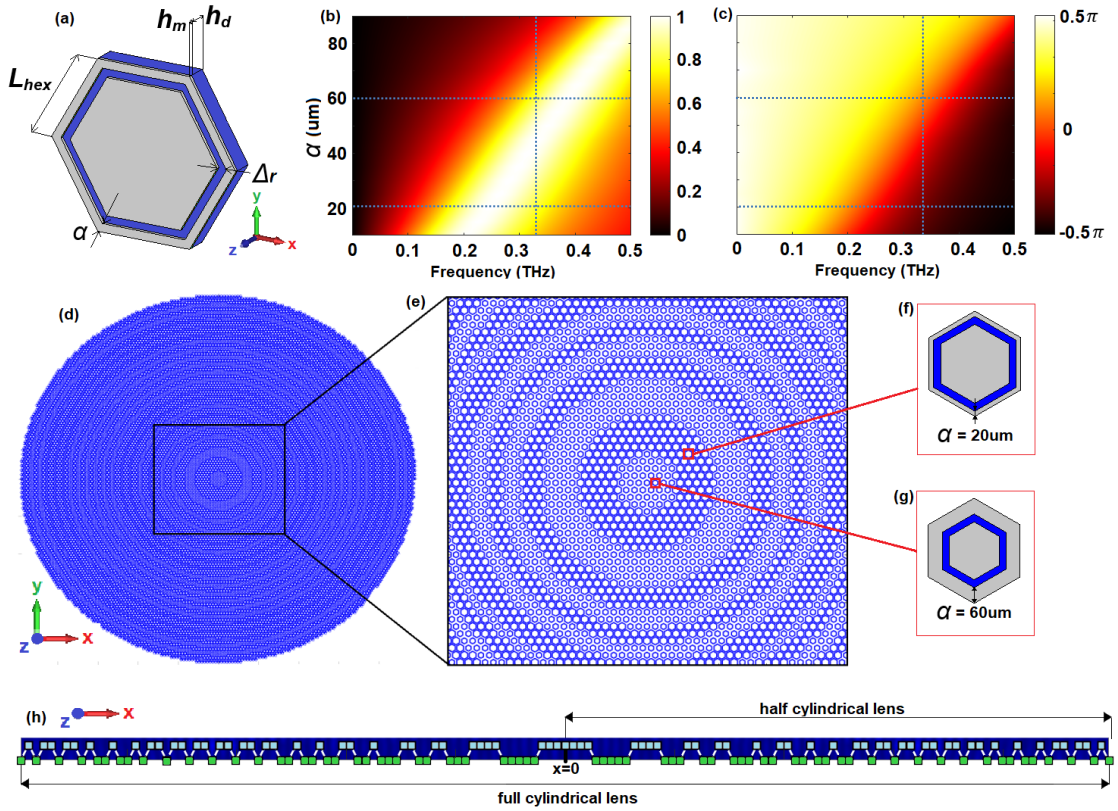

Fig 3.1. **(a)** Hexagonal unit cell proposed along with its geometrical parameters: L_{hex} = 200 μm, α varying from 20 to 80 μm, Δr = 30 μm, metal thickness h_m = 0.6 μm, dielectric height h_d = 35 μm. The metallic material (in grey) is copper, and the dielectric substrate (in blue) is polypropylene. **(b)** Normalized magnitude and **(c)** phase (in radians) maps of the transmission coefficient of the unit cell as a function of the parameter α and frequency. **(d)** Full metalens schematic and **(e)** zoomed view of the metalens central zones. In **(f,g)** are shown the unit cells of the even and odd zones, respectively. **(h)** Diagram showing the unit cell distribution of the designed cylindrical lens. Green and cyan squares represent a unit cell of type (f) or (g) respectively. For representation purposes, they have been shifted vertically, although, in the designed lens, they are all aligned along the x axis. The dark blue background is included only to enhance the contrast and help visualization.

Before engineering the unit cells for the even and odd zones, a preliminary analytical study is carried out using the Huygens-Fresnel principle considering homogeneous isotropic materials for the different regions of a cylindrical SOL, while imposing a focal length (*FL*) value of $10\lambda_0$. The Huygens-Fresnel principle states that any point where a wavefront hits, it acts as a secondary wave source [93]. For simplicity, each unit cell is analytically considered as a source-point that radiates a wave with the same amplitude and phase to its corresponding S21 coefficient. If reflection and absorption are neglected, the resulting field at each point of space (x, y, z) can be calculated by adding the fields of all sources. Mathematically, this can be written as:

$$A_{x,y,z} = \sum_{i=1}^{55} \frac{|S_{21,i}|}{\sqrt{l(x,y,z)}} e^{j(k_0 l(x,y,z) + arg\{S_{21,i}\})} \quad (3.1)$$

$$l(x,y,z) = \sqrt{(x-x_i)^2 + (y-0)^2 + (z-0)^2} \quad (3.2)$$

where $l(x,y,z)$ is the distance between the point source i and point in the space (x,y,z); k_0 is the wave vector in free space; (x_i, 0, 0) are the coordinates of the different unit cells, all ubicated along x axis. After calculating the fields, the power is derived using the well-known Poyinting theorem.

From the results of this preliminary study (shown in Fig. 3.2), it is found that a phase difference of at least π/6 radians between even and odd zones is necessary for the BPSO algorithm to converge and generate the focal spot at the design *FL*. In addition, since our aim is to increase the amplitude at the focus, both unit cells must be carefully engineered to ensure a high transmittance at the operation frequency. To achieve this, both the magnitude and phase of the transmission coefficient must be adjusted by varying the geometrical parameters of the unit cell. For simplicity, here only the width of the hexagonal slot (α) is modified, as we found that tuning this parameter is enough to achieve a satisfactory performance.

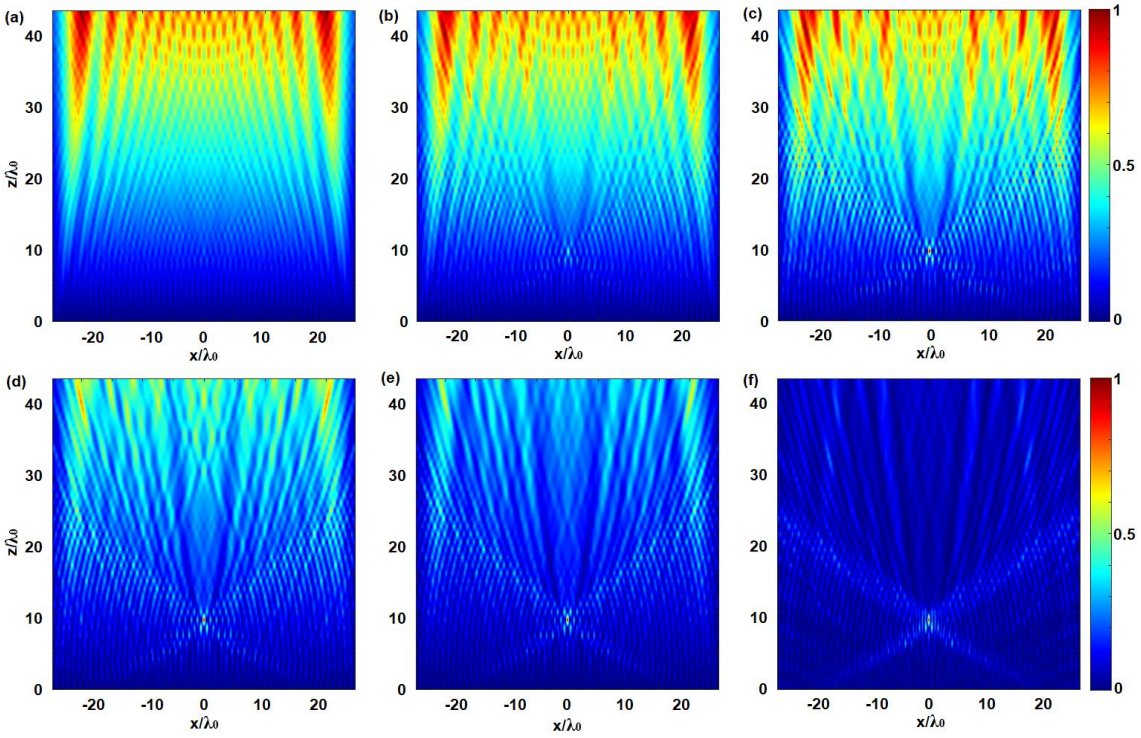

Fig. 3.2. Maps showing the normalized power distribution in the xz-plane considering a phase difference between the even and odd zones unit cells (in rads) of (a) π/90; (b) π/22; (c) π/11; (d) π/7.5; (e) π/6; (f) π/2.5. The transmission coefficient magnitude is set to 0.8.

The design is done using the frequency domain solver of the commercial software CST Microwave Studio®. Unit cell boundary conditions are applied on the transverse plane and open boundaries along *z* (see coordinate axis in Fig. 3.1). The structure is illuminated with the fundamental TE_{00} mode of a Floquet port, which corresponds to a vertically polarized plane wave (E_y), considering only normal incidence. With this setup, the contour maps of the magnitude and phase of the transmission coefficient as a function of α and frequency are calculated and shown in Fig.3.1b,c respectively. As observed, the phase of the unit cells can be tuned from –π/2 to π/2 rad within the spectral range under study. Note that the phase excursion does not cover the complete –π to π rad range, as required in a graded index lens design, for instance. To increase the phase excursion, one could either increase the frequency range or change the unit cell. However, this is not an issue in the proposed SOL as it only requires two unit cells with a small phase difference of π/6 between them.

Hence, from these results, we can determine the slot width of each unit cell taking into account the two design conditions mentioned above: to get the highest possible transmittance and a phase difference larger than π/6 at the design frequency of f_o = 0.327 THz (highlighted as a vertical dashed grey line in Fig. 3.1b,c). The selected unit cells correspond to the designs with α_1 = 60 μm ($0.065\lambda_0$) and α_2 = 20 μm ($0.022\lambda_0$) which have a relatively high transmission

coefficient of 0.8 and a phase of 0.12π and 0.28π, respectively, resulting in a phase difference of 0.16π, fulfilling both requirements. Both solutions have been highlighted with horizontal dashed gray lines in Fig. 3.1b,c.

Considerations on BPSO

Once the unit cells have been selected, the SOL design is carried out by implementing a modified BPSO algorithm, as explained in the introduction. In our calculations we consider the following constants: $V_{max} = 6$, as suggested in [94] to set a limit to further exploration after the population has converged; $c_1 = c_2 = 2$, to give equal weight to the social and the cognitive components; $w \in [0.4, 0.6]$, considering a time-varying inertial weight starting from 0.6 and decreasing proportionally after each iteration. The maximum number of iterations is set to 2000. In addition, a swarm of 100 particles is considered, being each of them a vector with 72 components. In order to reduce the computational burden, a cylindrical lens is first designed and its near field distribution at the operation frequency is calculated analytically with the Huygens-Fresnel approximation [87], [88]. Isotropic point sources with magnitude and phase taken from the selected unit cells are placed at each of the 72 positions with a separation of 350 μm ($0.381\lambda_0$).

The optimization of the SOL is done in two steps, see Fig. 3.3. In a first stage, an adapted weighted *sinc* is used as the goal function to get the desired profile of the target power distribution along the *x*-axis at $z = FL = 10\lambda_0$, starting with a random unit cell distribution [81]. The highest weight in the goal function is given to the focal spot. This makes the variance much bigger there than elsewhere, and the optimizer tries to reduce it, quickly developing a focus at the desired point, as shown in see Fig. 3.3. The second step consists in reducing the power distribution of the side lobes with a new weighted exponential goal function. Another optimization process is launched using particles derived from the best combination found in the first step, and varying, then, one position between two consecutive particles. After applying this two-step process, the found global best solution is 1111222211112221122112222122112212212211211211211211211212122121221211211212, where "1" and "2" stand for unit cells of type 1 and 2 (α_1 and α_2), respectively. This vector is the unit cell distribution along the *x*-axis, from the center of the lens to its rightmost edge (the left-hand side is obtained by simply mirroring the array, making use of the lens symmetry). Thus, after this procedure, the cylindrical metalens has a total length along the transversal *x*-axis of $D \approx 54\lambda_0$.

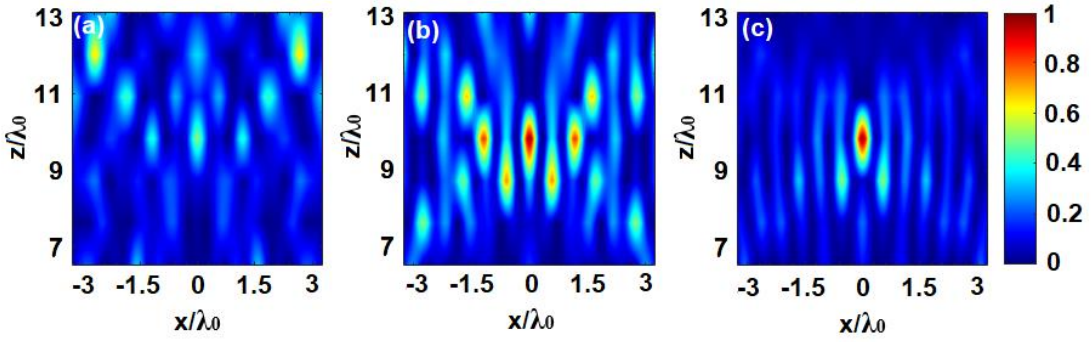

Fig. 3.3. Normalized power distribution after **(a)** random start; **(b)** end of 1st step; and **(c)** end of 2nd step.

Analytical results obtained from BPSO

The analytical normalized power distribution, obtained by applying the Huygens–Fresnel technique to the solution derived from our algorithm, is shown in Fig. 3.4. As observed there, a clear focus appears at $FL = 9.816\lambda_0$, very near the designed value of $FL = 10\lambda_0$. From the power distribution along the x-axis at $z = FL$, depicted in in Fig. 3.4., we see that the value of full width at half-maximum (FWHM, defined as the distance at which the power distribution has been reduced to half its maximum) in the transversal x direction is $FWHM_x = 0.36\lambda_0$, which is well below the diffraction limit ($0.65\lambda_0$).

In the next step, we implement a spherical lens by simply applying rotation symmetry to the cylindrical lens solution, obtaining radial zones. As before, we compute, first, the near field distribution with the Huygens-Fresnel approach. The normalized power profile along both *x*- and *y*-axes at *FL* is represented in Fig. 3.4b (both curves are identical). The focus in this case appears at $FL = 9.16\lambda_0$ and has a $FWHM = 0.46\lambda_0$ both along *x* and *y* directions, also below the diffraction limit.

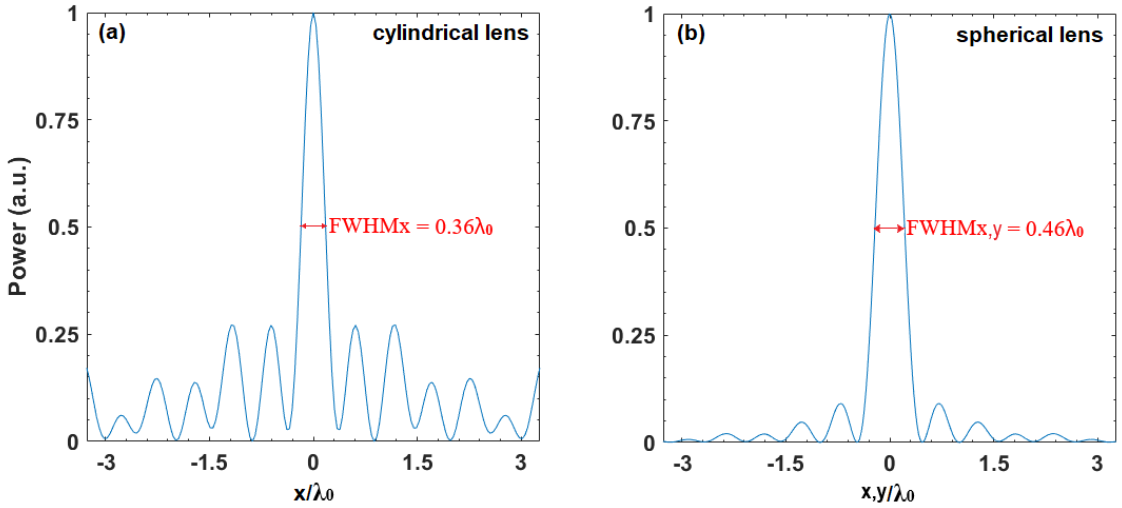

Fig. 3.4. **(a)** Numerical results of the normalized power distribution along the *x*-axis at $z = FL = 9.816\lambda_0$ for the cylindrical SOL **(b)** idem for the spherical SOL along both *x*- and *y*-axes at $z = FL = 9.162\lambda_0$

To verify that the focal spot generated in the spherical lens is, indeed, super-oscillatory we analyze the behavior of the local wavenumber, k_{local}. According to the definition of super-oscillation [82], k_{local} is equal to the phase gradient ($k_{local} = \nabla\mathbf{\Psi}$), where $\mathbf{\Psi}$ is computed as $\mathbf{\Psi} = \arg\{\mathbf{E}(r_o)\cdot\mathbf{E}(r_i)\}$; the function $\arg\{a\}$represents the argument of a complex number *a*, and $\mathbf{E}(r_o)\cdot\mathbf{E}(r_i)$ is the scalar product of the electric field at points r_o and r_i; r_o is the reference point with coordinates (0, 0, *FL*) and r_i has coordinates *(x, y, FL)*. In the super-oscillatory region k_{local} should be larger than the highest wavenumber component ($k_0 = 2\pi/\lambda_0$, in free space). We use the center of the lens as a reference point to calculate the phase of the electric field along the *x*-axis at the focus ($z = FL$). As shown in Fig 3.5, there are regions where the phase rapidly oscillates and k_{local} is much larger than k_0, demonstrating that the operation is based on super-oscillations. Moreover, these regions correspond to the electric field intensity minima, which is also a characteristic of super-oscillatory devices.

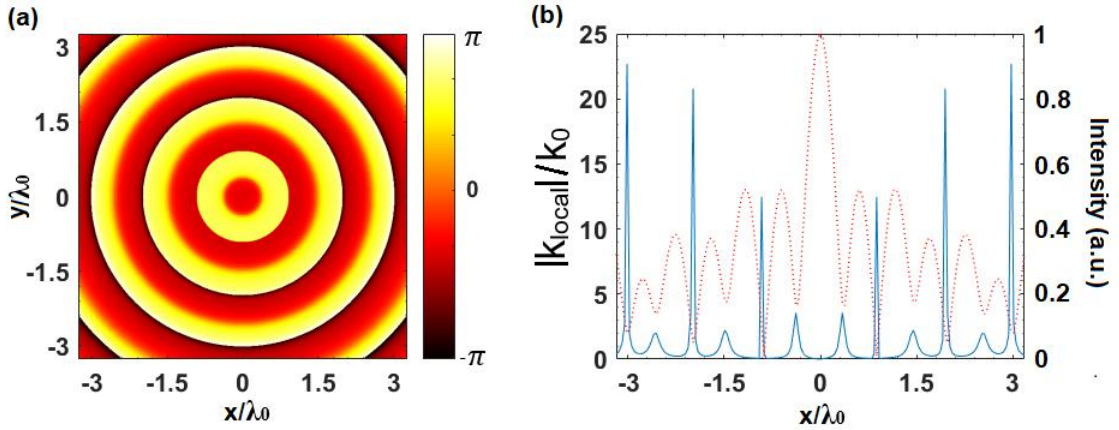

Fig. 3.5. (**a**) Phase distribution in radians at $z = FL = 9.162\lambda_0$, using the central point as phase reference. (**b**) Local wavenumber-vector distribution (blue) where the peaks indicate the super-oscillatory regions, and electric field intensity (dotted red) along radial direction, normalized to the maximum.

Simulation results

The transient solver of the commercial software CST Microwave Studio™ is used to evaluate the performance of the full metalens. The center of each unit cell is placed at the coordinates of the source points obtained in the Huygens-Fresnel analysis. A schematic of the final design is shown in Fig. 3.1d,e. The lens is illuminated using a plane wave under normal incidence assuming open boundary conditions in all directions. Moreover, magnetic and electric symmetries are applied on the *yz*-plane and *xz*-plane, respectively. A fine hexahedral mesh is used, with smallest and largest mesh cells of 17.8 μm ($\approx 0.019\lambda_0$) and 60 μm ($\approx 0.07\lambda_0$), respectively.

The simulation results of the power distribution on the *E*-plane (*yz*), *H*-plane (*xz*), and *xy*-plane (at $z = FL$), for the designed SOL at the operation frequency of 0.327 THz, are shown in Fig. 3.6 (right column), along with the analytical results of the spherical lens obtained with the Huygens–Fresnel method (left column). As observed, the agreement between both results is qualitatively good, although there are some differences, probably due to the simplifications assumed in the analytical models to speed up the analysis.

To better compare these results, a summary of the metalenses' performance is shown in Table 3.1. There, the values of the cylindrical SOL are also included for completeness.

	Cylindrical SOL (Analytical)	**Spherical SOL (Analytical)**	**Spherical SOL (Simulation)**
FL	$10\lambda_0$	$9.16\lambda_0$	$9.56\lambda_0$
$FWHM_x$	$0.36\lambda_0$	$0.46\lambda_0$	$0.44\lambda_0$
$FWHM_y$	-	$0.46\lambda_0$	$0.5\lambda_0$
Enhancement	-	18.4 dB	16.6 dB
Ellipticity	-	1	0.88
Depth of Focus	$1.14\lambda_0$	$1.28\lambda_0$	$1.51\lambda_0$

Table 3.1. Summary of the focusing properties of the studied SOL.

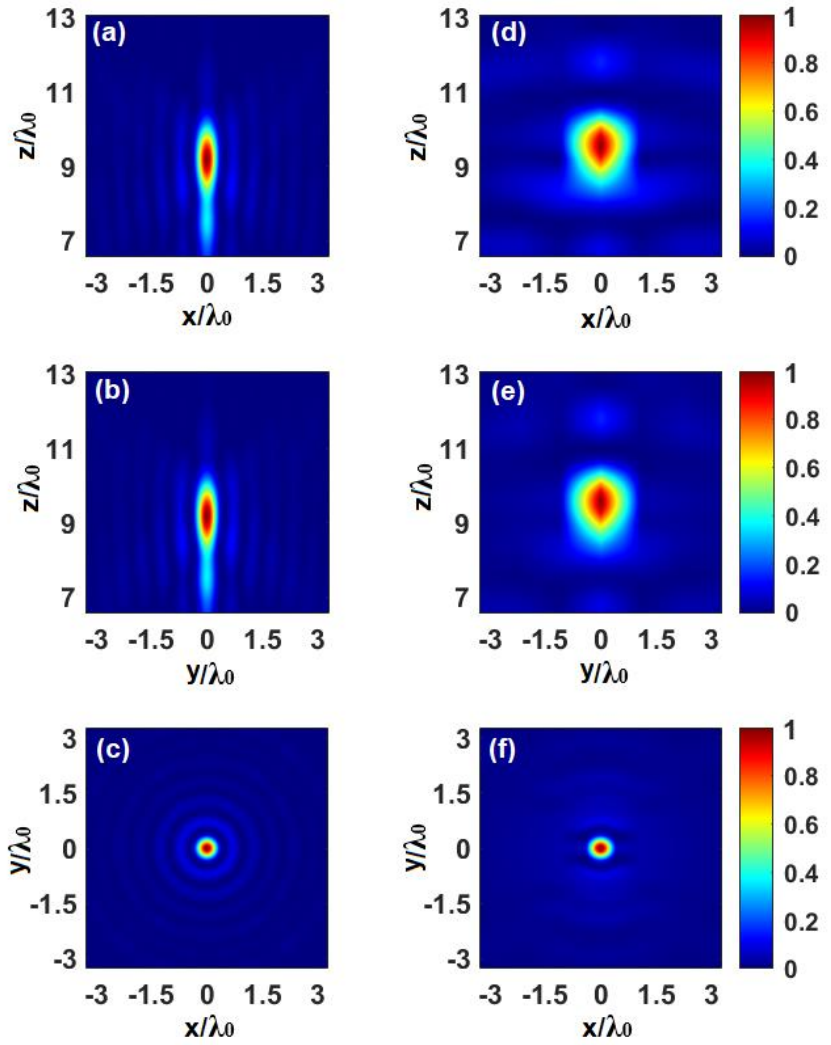

Fig. 3.6. Normalized power distribution on the *xz*-plane (**a**,**d**), *yz*-plane (**b**,**e**), and *xy*-plane (**c**,**f**), for both the simulated spherical lens (right column) and the analytical spherical lens (left column). The *xy*-plane is obtained at $z = FL$, with $FL = 9.56\lambda_0$ in the simulated lens, and $FL = 9.16\lambda_0$ in the analytical lens; the *xz*-plane is the H-plane, and the *yz*-plane is the E-plane.

For the simulated spherical SOL, the subwavelength focal spot is numerically found at a distance of 8.77 mm ($9.56\lambda_0$), which is near the designed value ($10\lambda_0$) with a transversal resolution of $FWHM_x = 0.44\lambda_0$ and $FWHM_y = 0.5\lambda_0$ along the *x*- and *y*-axis, respectively. Note that these values are below the diffraction limit ($0.65\lambda_0$).

Low side lobes are obtained in all cases, with a magnitude of the highest side lobe approximately 10% below of the main lobe in the simulated SOL. With respect to the depth of focus (DOF, defined as the distance along the *z*-axis where the power distribution has decayed half its maximum from the *FL*), the simulated spherical SOL shows a bigger value than the analytical spherical SOL ($1.51\lambda_0$ and $1.28\lambda_0$, respectively). This is an expected result because of the higher accuracy of the numerical analysis, done using the physical unit cells (taken from Fig. 3.1).

To compare, further, the focusing performance, the power enhancement (defined as the power amplitude at the *FL* with and without the SOL) is smaller in the numerical simulation. This can

be explained by considering that, in contrast to the analytical calculation, in the simulated model, both material loss and diffraction effects are considered. Finally, it can be noted that the focus ellipticity (defined as the ratio between $FWHM_x$ and $FWHM_y$) is very close to unity in both spherical lenses, which means an almost spherical focal spot in the *xy* plane.

3.1.2 Experimental results

The fabricated SOL is experimentally measured with the Vector Network Analyzer (VNA) model Agilent N5242A available in the UPNA's THz laboratory. The VNA provides both the amplitude and phase of the transmitted and the resulting signal. The operational and logical control of the analyzer is done with a PC computer. The lens behaviour was measured in Near-Field, using 220-330 GHz waveguide probes in the configuration shown in Fig. 3.7. The source delivers power in the mW range, and it is set with an output power of 6.5 dBm; The meta-SOL is illuminated with a probe placed at a distance enough to ensure uniform illumination. Thus, the lens is fed with quasi-planar vertically polarized radiation. Another probe is used as the receptor to detect the hotspot. Millimeter-wave absorbers are spread throughout the setup to mimic anechoic chamber conditions.

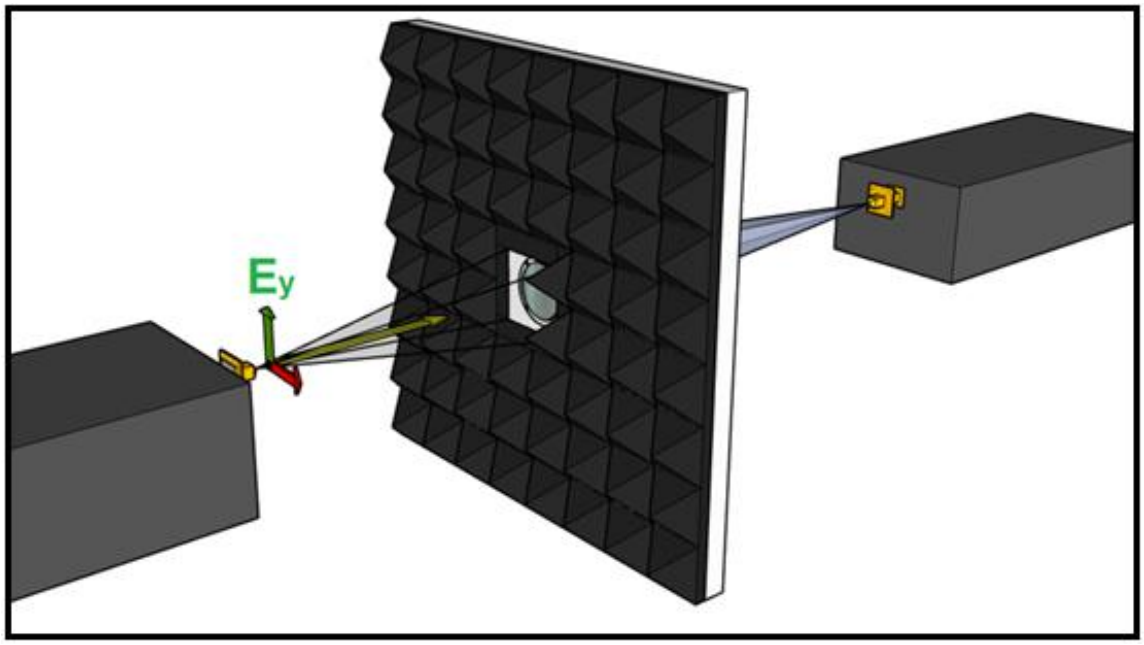

Fig. 3.7. Experimental sketch: Transmitter (Vertical polarization, planewave), lens and detector.

The measurement process, for the time being, has been been abruptly interrupted by the outbreak of the Covid-19 pandemic. The available measurements are three different raster-scans of the *xy*-plane at z = 12.9, 13.4 and 13.9mm, respectively, covering a frequency range from 307 to 347 GHz. The measurement process is expected to be resumed as soon as the Covid-19 confinement restrictions are lifted. The experimental results obtained are summarized in Fig. 3.8:

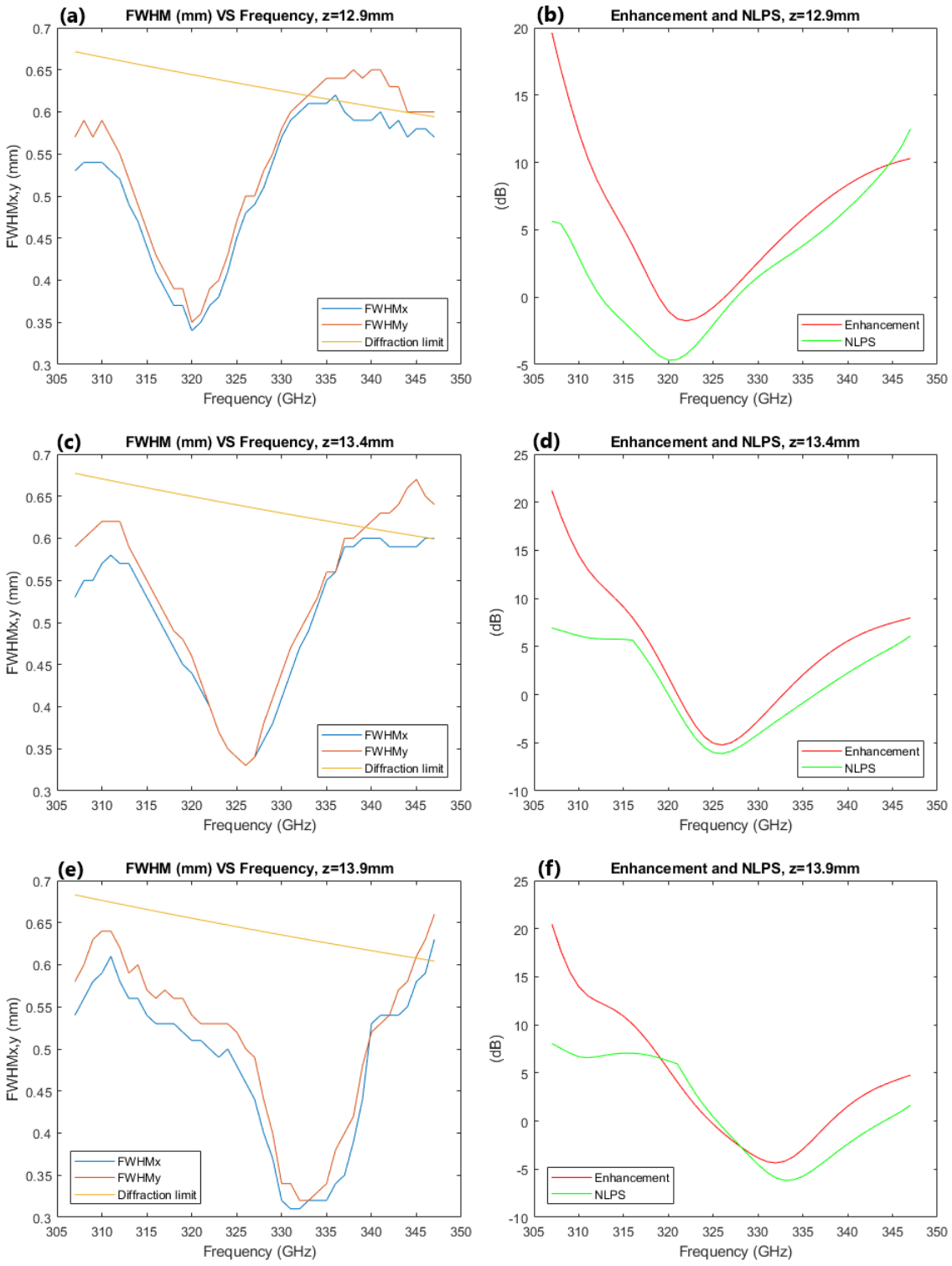

Fig. 3.8. (a,c,e) $FWHM_{x,y}$ (mm) with indication of the Rayleigh diffraction limit (mm); (b,d,f) E-field enhancement (dB) and NLPS (dB), obtained from the *xy*-planes measures at z = 12.9, 13.4 and 13.9 mm, respectively.

It must be noted that the theoretical focal length value is between $9.16\lambda_0$ and $9.56\lambda_0$, according to the analytical and simulation results, being $\lambda_0 \approx 0.917$mm. This means that the designed focal length is somewhere between 8.4 and 8. 8mm. This range of values are far away from the ones used to characterize the lens. It is expected to measure more *xy*-plane cuts to fully study the lens behaviour.

In any case, from the partial results obtained it is clearly shown that the designed metaSOL successfully achieves a factor of ≈ 2 improvement in the size of the focal spot, relative to that dictated by the Rayleigh diffraction limit, in the proximity of the design frequency (f_0 = 327GHz) for the three *xy*-plane cuts recorded. Of course, this superresolution comes at a price: higher side lobes, lower E-field enhancement and a limited FOV. In Fig. 3.9 a selection of diffraction patterns (*xy*-planes) experimentally obtained are shown.

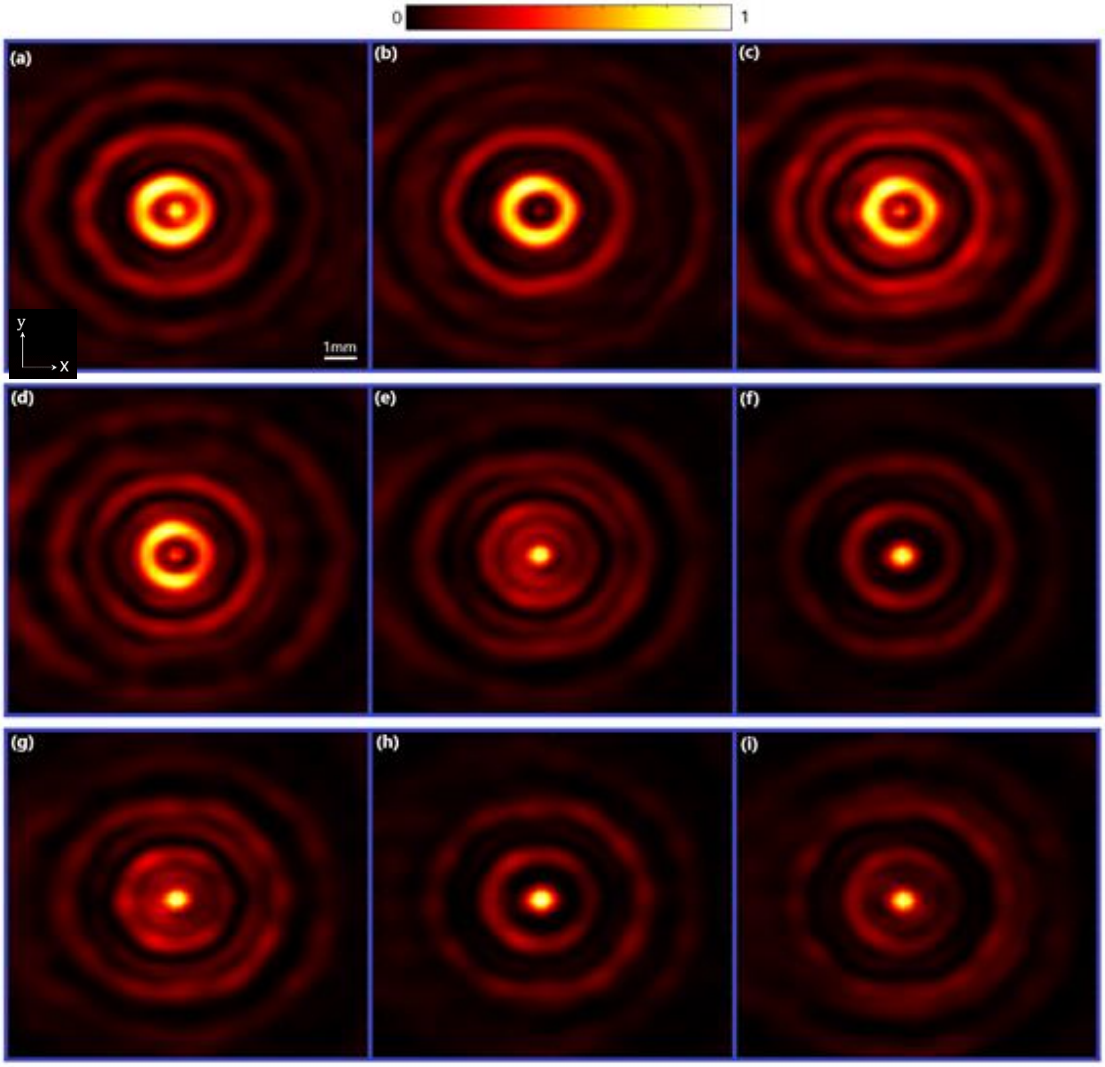

Fig. 3.9. Normalized power distribution in the *xy*-plane at z = 12.9 mm (a,d,g), z = 13.4 mm (b,e,h) and z = 13.9 mm (c,f,i), for f = 327, 316 and 307 GHz respectively. The different focusing properties of these foci can be consulted in Table 3.2.

Parameters \ #	**(a)**	**(b)**	**(c)**	**(d)**	**(e)**	**(f)**	**(g)**	**(h)**	**(i)**
Frequency (GHz)	327	327	327	316	316	316	307	307	307
FL (λ)	14.06	14.61	15.15	13.59	14.11	14.64	13.20	13.71	14.22
Diffraction limit (λ)	0.69	0.69	0.70	0.69	0.69	0.70	0.69	0.69	0.70
$FWHM_x$ (λ)	0.53	**0.37**	0.48	0.43	0.53	0.56	0.54	0.54	0.55
$FWHM_y$ (λ)	0.54	**0.37**	0.53	0.48	0.55	0.59	0.58	0.60	0.59
Ellipticity	0.98	1	0.91	0.89	0.96	0.95	0.93	0.90	0.93
NLPS (dB)	-0.01	-4.93	-0.82	-2.38	6.91	7.67	6.92	7.26	**8.05**
Enhancement (dB)	1.01	1.24	0.25	6.59	7.99	10.07	19.63	21.21	**20.47**
FOV (λ)	1.12	0.85	0.82	1.03	1.60	>10	2.80	>10	>10

Table 3.2. Summary of focusing properties of the different foci from Fig. 3.9.

As it can be observed from Table 3.2, clearly suppressed sidelobes can be found on some of the characterized foci. One of the most remarkable results is the metaSOL efficiency; nevertheless, the enhancement obtained is hard to compare because this is parameter is generally overlooked in the scientific literature. There is a good reason for this: efficiency is one of the most challenging issues when designing a SOL; so when the spot size is far below the superoscillation criterion value, there is an exponential decrease in the efficiency. One of the hotspots found at the design frequency f = 327GHz is sharper than $0.37\lambda_0$. Although it is surrounded by relatively high sidelobes, the E-field is intensely condensed in the hotspot.

This is a noteworthy feature, since the sub-diffraction-limit hotspots are achieved at a price of tremendous incident energy loss and this technique helps overcome the actual focusing efficiency of SOLs that it is found to be dissappointing when used in super-resolution imaging microscopy [101]. Even for the largest-sized state-of-the-art SOLs, the focusing efficiency is only 5% at most [102], while in our design the yield (fraction of energy concentrated in the central hotspot) is shown to be larger than 7% for the sharpest foci (Table 3.2, case b).

The simulated focal spot had an average of $0.47\lambda_0$, being the sidelobes intensity less than 10% of the focal spot intensity while the enhancement was 16.6dB. It is clearly seen in Table 3.2 that there are spots that clearly surpass the simulated enhancement and that are very close to the NLPS value (around 15% of the focal spot intensity).

Another promising feature is that, up to now, most of the reported SOLs are only applicable for a single wavelength. Although SOLs for several isolated wavelengths have been demonstrated, there are not many examples of broadband SOLs. In our work, the designed SOL can achieve a resolution below the diffraction limit over a broad range (>10% fractional bandwidth), although it is true that the focal parameters have a large variation.

A deeper study of the designed meta-SOL will be carried on in the near future.

3.2 Extended studies on the super-oscillatory lenses

In the previous chapter, the designed metalens has proven to offer a promising approach for focusing THz radiation. After exploring the capability of binary ultra-thin metalenses, based on super-oscillatory phenomena, to obtain highly compressed focal spots, here different solutions to improve the performance of these lenses are studied.

A binary lens can only control either intensity or phase in a discrete fashion, such as "yes/no" for intensity and "0/π" for phase. In the SOL previously designed, we fixed the intensity to a high level for both particles to enhance transmission and afterwards we induced the desired phase difference between them to develop the desired focus. This binary nature limits the attainable size of superoscillatory hotspots, and does not allow efficient trade-offs between focal points intensity, size and field of view.

The performance of any THz system based on lenses could be significantly improved if ultrathin lenses with strong focusing properties and low aberrations (chromatic, spherical…) were available. A flat and thin metalens does not show, in theory, spherical aberrations due to the lack of curved surfaces in the beam path. One of the most natural means to improve such lenses could be the use of graded index (GRIN) metamaterials, as has been proposed in different works [95–98].

Following this concept, new procedures have been developed for generating superoscillatory foci, by means of optimizing the hotspots with preset characteristics such as the size, intensity, field of view, etc. [99]. For instance, in [100] the authors designed a MTM superlens that allows full control of intensities and phases of the scattered waves. The proposed lens contains thousands of discrete sub-wavelength plasmonic metamolecules set in a cylindrically symmetric pattern. The desired superoscillatory focus is constructed using analytical band-limited functions (in this case, circular prolate spheroidal wavefunctions), so that it can be formed by the interference of free-space waves. Once the superoscillatory hotspot is chosen, the entire field in the focal plane is mathematically backpropagated to the chosen location of the mask. The amplitudes and phases of the back-propagated fields at the mask plane give the exact amplitude attenuation and phase distribution needed.

This section will explore the use of: a) molecules with high transmittance and different transmission phase to obtain binary, 4-ary, 8-ary and 16-ary metalenses; b) the combination of unit cells with multiple high transmission amplitude and phase retardation values; c) the overall effect of getting smaller unit cells while keeping the same lens size.

3.2.1 Combining super-oscillatory and graded index concepts in a single lens.

In this section we study the focusing properties of discrete metasurfaces acting as a SOL. Each metasurface now involves a fixed number of different metamolecules (2, 4, 8, 16 or 64), but, contrary to the strategy used in reference [100], where the transmission efficiency is always lower than 10%, all our metamolecules will be tailored to provide the highest possible transmission while attaining the needed phase at the output. This cannot be accomplished with a pre-established hotspot because the analytical equations involved demand different intensity values in the lens plane, so an optimization methodology will be implemented as an alternative.

The desired lenses, as in our previous SOL design, will be constructed from a large number of concentric rings, each containing metamolecules of the same type. The optimization is based

on the Genetic Algorithm (GA) because it is an intuitive way of solving *n*-ary optimization problems. Aside from that, the same basic strategy as the one followed in the previous chapter for our original binary SOL design will be applied here.

At this moment of the design process, we will not consider any specific kind of unit cell or metamolecule scheme but will consider instead arbitrary transmission coefficients. Later, we will study how to transfer the different theoretical metamolecules involved into feasible unit cells. Anyway, keeping always in mind the implementability of our devices, the number and size of the different metamolecules is in fact fixed and proportional (by a factor ≈ 3) to the wavelength range of interest (f = 270 to 340 GHz). The actual design of the unit cells that represent the metamolecules considered, will be carried on in a future study.

To start, GA generates an initial population containing *nPop* chromosomes, each one of them representing a candidate solution. Any chromosome is composed of 72 different genes (each gene being a metamolecule counting as one of the 72 particles that conform the semi-cylindrical lens used for optimization). Following the strategy seen in the previous chapter, each of the chromosome´s 72 binary dimensions is considered as a source-point that radiates a wave with the same amplitude and phase to the corresponding S21 coefficient considered. Each of the 72 dimensions is separated 350 μm from the others (exactly the width of the hexagonal unit cells seen in the previous chapter).

Then, the chromosomes are evaluated based on their fitness function values (which basically corresponds to the difference between the E-field distribution created by a chromosome and the stablished E-field targetted profile, both calculated following the Huygens-Fresnel Principle). The chromosomes with the better fitness values are selected as candidates for the next population. Next, GA operators, namely crossover and mutation, generate the next population based on the crossover rate of *pc* and mutation rate of *pm*, for which the roulette wheel selection method is employed. By repeating the above stages, GA terminates to a near-optimum solution.

Considering the vast number of optimizations to execute, the parameters of the meta-heuristic are calibrated using the Taguchi method to improve the quality of the solutions obtained. It is essential to segregate the individual effect of independent variables to find an optimal combination of them such that the response (the adjustment to the goal function) is optimized within the lesser possible time.

As stated in the introduction, the Taguchi method is based on 5 successive steps. 1) The parameters of GA with potential effects on the response are determined: hese are the number of chromosomes, *nPop*, the number of iterations, *It*, the crossover percentage, *pc* and the mutation percentage, *pm*. 2) A preliminar analysis is done to determine approximate levels of the mentioned parameters. 3) The L_9 orthogonal array is selected to understand the effect of 4 independent factors each having 3 factor level values. 4) The proposed design is used to carry on instances of the planned simulations. 5) For a minimization problem, the Taguchi method aims at maximizing the Signal to Noise Ratio (SNR) using equation 2.5.

The different simulations to be carried on are summarized in the Layout shown in Table 3.3.

L_9 Orthogonal array					
	Independent Variables				Goal function Values
Simulation #	***nPop***	***It***	***pc***	***pm***	
1	75	1000	0.75	0.2	g_1i, $i = 1…n$
2	75	2000	0.80	0.3	g_2i, $i = 1…n$
3	75	3000	0.85	0.4	g_3i, $i = 1…n$
4	100	1000	0.80	0.4	g_4i, $i = 1…n$
5	100	2000	0.85	0.2	g_5i, $i = 1…n$
6	100	3000	0.75	0.3	g_6i, $i = 1…n$
7	125	1000	0.85	0.3	g_7i, $i = 1…n$
8	125	2000	0.75	0.4	g_8i, $i = 1…n$
9	125	3000	0.80	0.2	g_9i, $i = 1…n$

Table 3.3 Layout of the L_9 orthogonal array. Each simulation is repeated $n = 10$ times.

Note that *nPop* and *It* are problem dependent as their optimum values must be obtained based on the size of the problem. The mean SNR values obtained and their plots for the different parameters are shown in Fig. 3.10. The tuned values of the GA parameters that maximize the SNR are: *nPop* = 100, *It* = 2000, *pc* = 0.8 and *pm* = 0.3.

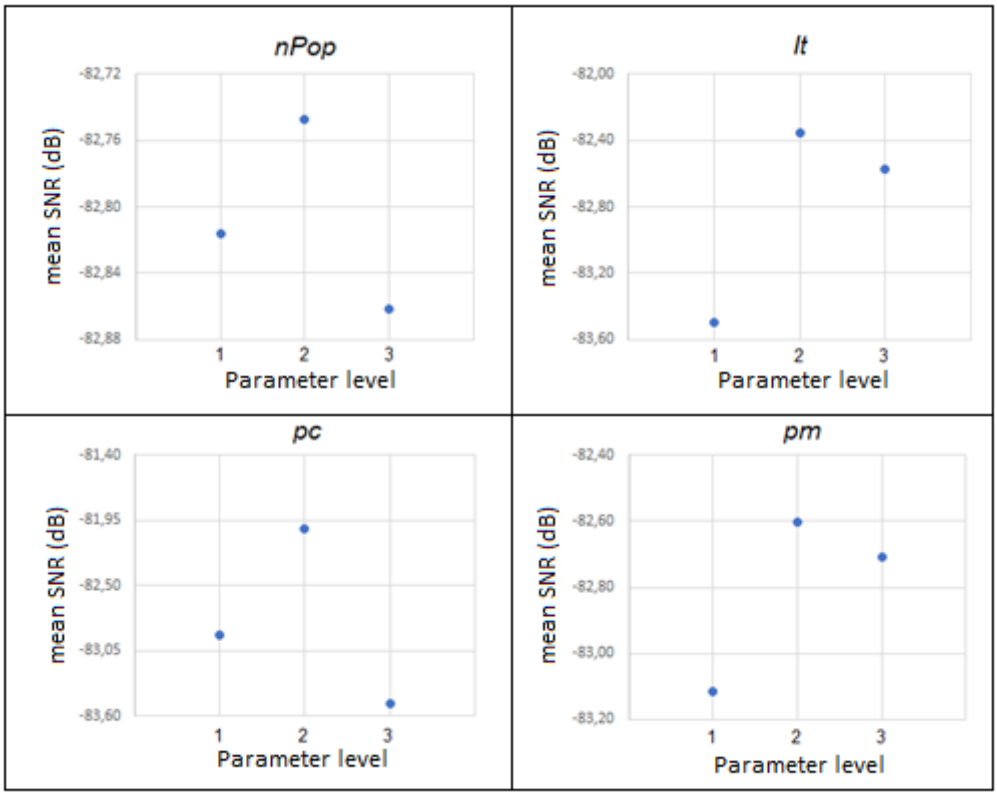

Figure 3.10. The mean SNR plot (in dB) for each level of the different GA parameters.

Having obtained the tuned values of the GA parameters to be used in the intense optimization labour ahead, in Table 3.4 we present the different optimization tasks proposed to complete a deep study of the possibilities of using high transmission metamolecules with different levels of transmission phase. At this stage, the amplitude level for all the metamolecules is set constant and equal to 0.8.

Number of Metamolecules	Phase levels (rads)	Amplitude level (0-1)	Frequency range (GHz)	Focal Lengths (mm)
2	[0, π/3]	0.8	270 - 340	4 - 12
2	[0, 2π/3]	0.8	270 - 340	4 - 12
2	[0, π]	0.8	270 - 340	4 - 12
4	[0, π/6, π/3, π/2]	0.8	270 - 340	4 - 12
4	[0, π/3, 2π/3, π]	0.8	270 - 340	4 - 12
4	[0, π/2, π, 3π/2]	0.8	270 - 340	4 - 12
8	[0, π/4, … 7π/4]	0.8	270 - 340	4 - 12
16	[0, π/8, …15π/8]	0.8	270 - 340	4 - 12

Table 3.4. MetaSOLs analytic study plan. The first column indicates the number of metamolecules considered in the respective SOL design (i.e. 4 metamolecules means that the SOL is built from 4 different zones, each having a different transmission phase but the same transmission magnitude). The frequency step Δf is 5 GHz and the focal length step is ΔFL = 1 mm.

It is clear that the designed plan considers 1080 different optimization processes: 8 different sets of metamolecules, each one of these sets being optimizated for 15 different frequency values and 9 different focal lengths. It is expected to obtain a deep insight in the behaviour of the different designs to perform a comprehensive comparison among them.

Considerations on GA

The design of the pseudo-GRIN metaSOLs is based on the powerful GA optimization (see Sec. 2.1.2). In our algorithm configuration, we will consider the following parameters tuned by the Taguchi method: $nPop$ = 100, It = 2000, pc = 0.8 and pm = 0.3.

It must be noted that the algorithm is significantly different than the code used in the first part of this work: a) The new algorithm is now based in the GA optimization and not in the BPSO and the goal functions used are different in both cases; b) The new algorithm is now run in just one phase, instead of the two original phases. This is done by means of introducing subtle changes in the goal function profile while the optimization is running. c) Although mutation operators provide the ability to overcome a local optimum point solution, to mitigate or even avoid more trapping into a local optimum solution, new mutated solutions based on the best candidates are generated when the algorithm is stuck in a plateau point. d) For the same reason, some GA parameters (mutation rate, η, and selection pressure, β) are dynamically modified during execution when the algorithm is stuck for a pre-fixed number of iterations.

It is noteworthy to mention that the chromosomes are no longer binary but n-ary, n=2,4,8,16. However, as in the binary case, we will consider that a chromosome has 72 genes, each one representing a fraction of half a cylindrical lens. This cylindrical lens approximation greatly reduces the computational burden of the optimization. Its near-field distribution at the operation frequency is calculated analytically with the Huygens–Fresnel approximation assuming isotropic

point sources, with magnitude and phase values pre-defined, that are placed at each of the 72 positions with a separation of 350 μm.

Analytical results obtained from GA

The GA algorithm has been implemented in Matlab® with all the parameters and optimization conditions described so far. A weighted exponential function is used as the goal function to get the desired profile of the target power distribution along the *x*-axis at $z = FL$.

After applying this process, the global best solution is a vector representing the kind of isotropic source placed along each position of the *x*-axis, from the center of the lens to its rightmost edge. Later, the left-hand side of the cylindrical lens is obtained by simply mirroring the array, making use of the lens symmetry. Next the spherical lens is implemented by simply applying rotation symmetry to the cylindrical lens solution, and thus obtaining radial zones. As before, we compute the near-field distribution with the Huygens–Fresnel approach.

In order to improve the clarity and coherence when showing the results obtained, we will study first the design with only two different particles (i.e, binary lenses). The results are shown in Fig. 3.11.

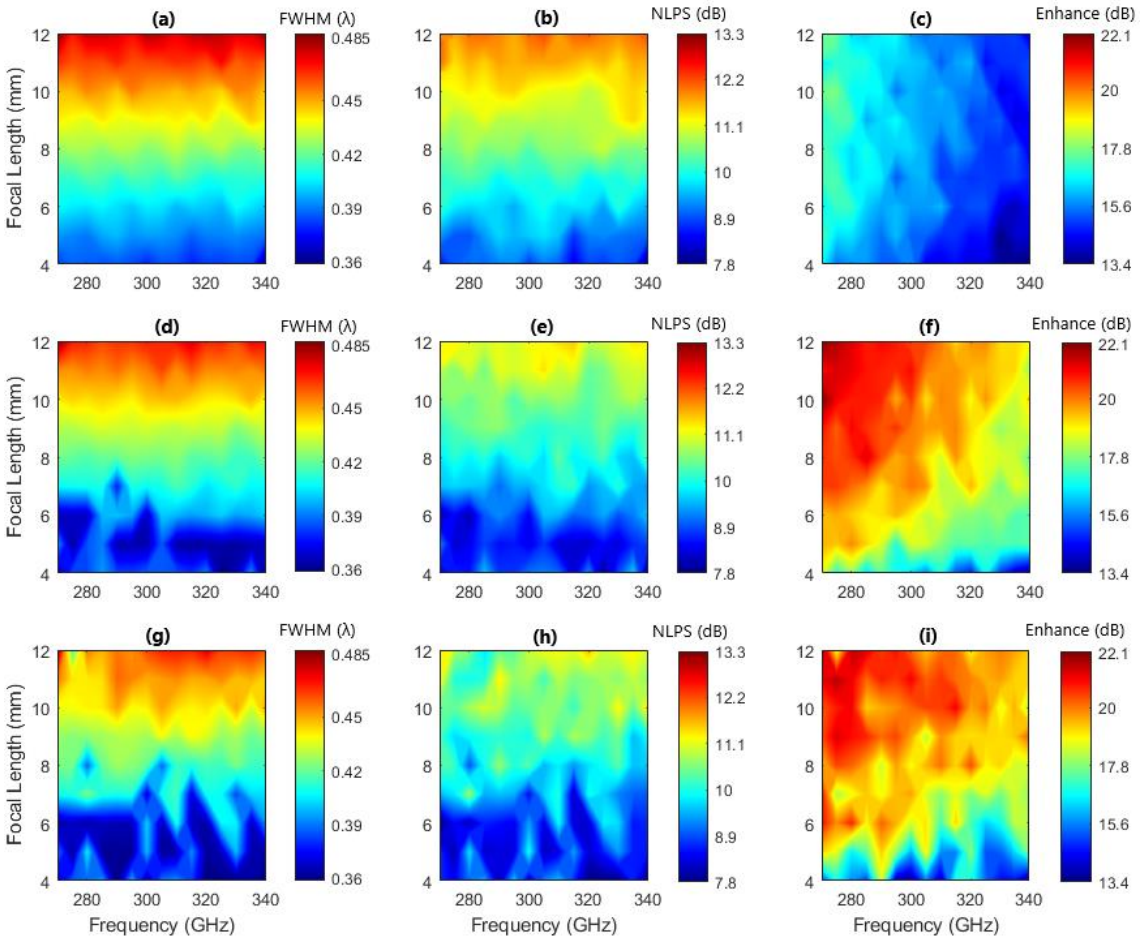

Figure 3.11. **(a,b,c)** Analytical results for $FWHM_{x,y}$ (normalized to λ), NLPS (dB) and enhancement (dB), respectively, for a binary spherical lens optimized considering two unit cells with $Amplitude_{1,2}$=0.8, $Phase_1$=0 rads and $Phase_2$=π/3 rads. **(d,e,f)** Idem, with unit cells designed with $Amplitude_{1,2}$=0.8, $Phase_1$=0 rads and $Phase_2$=2π/3 rads. **(g,h,i)** Idem, with unit cells designed with $Amplitude_{1,2}$=0.8, $Phase_1$=0 rads and $Phase_2$=π rads. The Focal Length axis accounts for the different FL values used in the optimization (9 different *FL* values) and does not represent a z-axis sweep.

These binary metalSOLs show the well-known tradeoff between the spot size and the side lobes level when the hotspot's *FWHM* becomes much smaller than the diffraction limit. In our study is clearly demonstrated that the phase difference between the two zones has a deep impact in the performance: increasing the difference between the phase responses (until a certain degree) in the two zones leads to an increasing chance of developing sharper focal spots at the cost of higher sidelobes. It can be also observed that the enhancement (and thus the transmission efficiency of the lens) is greatly improved when the phase difference of the two metamolecules is above $2\pi/3$ rads. This is coherent with the literature, having been reported that the use of binary phase masks in addition to amplitude masks increases the transmission efficiency of a lens [42]. Moreover, metamaterials allow the independent manipulation of the amplitude and phase of the transmission coefficient in one planar and thin metasurface and avoids the need of two different masks that are transmission inefficient.

Another fact worth mentioning is the almost-linear relationship between the focal length and the ability of getting a sharper focus: shortening the focal length leads to narrower foci. Of course, very small focal lengths could lead to impractical devices, but in the frequency range we are considering this is not an issue. To conclude the analysis of these binary SOLs, in table 3.5, the minimum and maximum values attainable for different hotspots parameters are shown. It is important to note that the hotspot is defined at the precise focal spot ($z = FL$) and, because of our design, it shows the highest SOL enhancement. This must be remarked, because when studying metaSOLs there are other focal spots (in fact, there is one *xy*-diffraction pattern at each z-position) that can have lower $FWHM_{x,y}$ or NLPS values. Anyway, foci sharper than the ones showed in Table 3.5. are perfectly attainable with our method, but one must relax the NLPS and Enhancement constraints to achieve them (i.e. it seems impossible today to obtain the sharpest hotspots attainable where the metaSOL concentrates the maximum E-field). Although the main purpose of this work is to surpass the diffraction limit with the highest possible NLPS and Enhancement values, those sharper foci, and the tradeoffs involved, will be studied later too.

Binary SOLs					
#	**Amplitude**	**Phases**	**$FWHM_{X,Y}$ (λ)**	**NLPS (dB)**	**Enhancement (dB)**
1	0.8	[0, π/3]	0,378 – 0,488	8,38 – 12,32	13,38 – 17,74
2	0.8	[0, 2π/3]	0,359 – 0,476	7,85 – 11,64	14,01 – 22,17
3	0.8	[0, π]	0,359 – 0,474	7,79 – 11,61	13,64 – 21,89

Table 3.5. Variation range for the different parameters studied in the three different binary SOLs studied.

From now on, the analysis with *n*-ary lenses ($n > 2$) will be carried on. To begin with, in Fig. 3.12 the results obtained with 4 different metamolecules are shown. As in the binary lens, three different cases with different phase steps are studied.

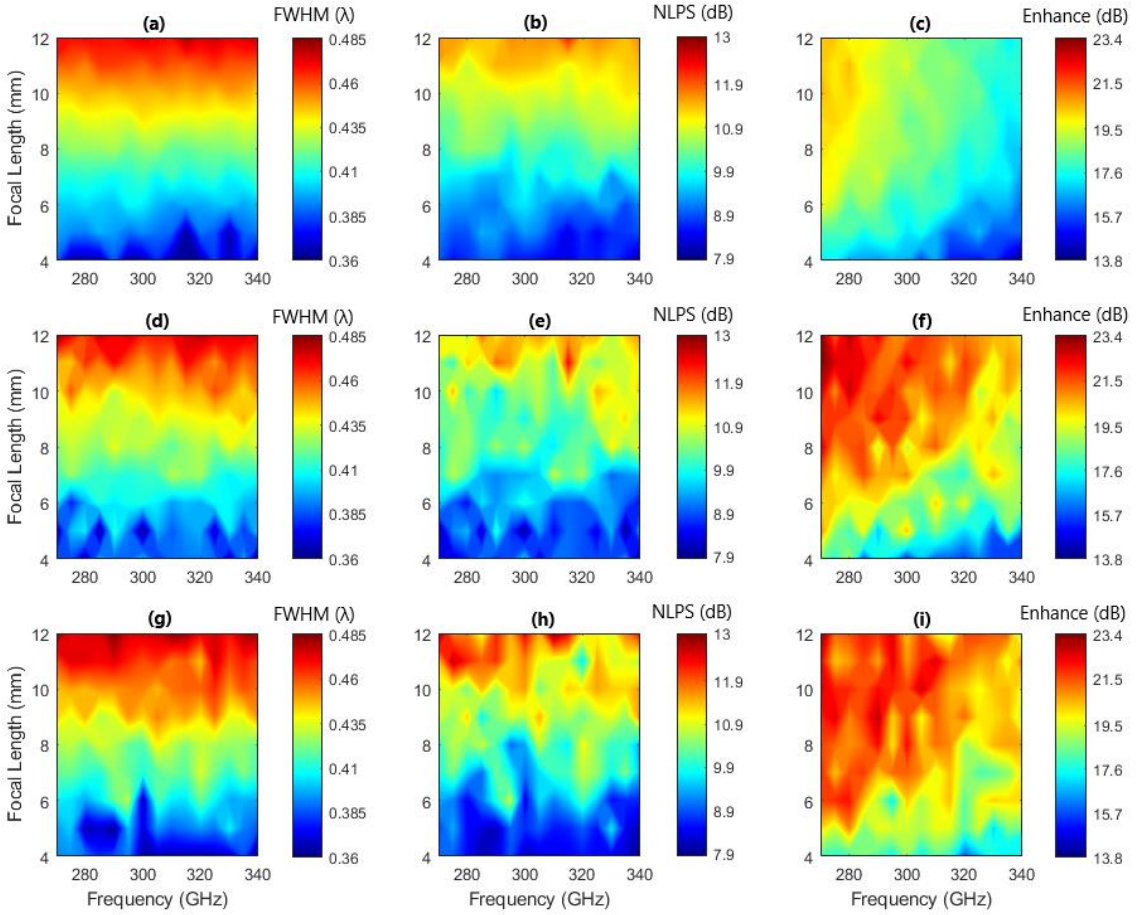

Figure 3.12. **(a,b,c)** Analytical results for $FWHM_{x,y}$ (normalized to λ), NLPS (dB) and enhancement (dB), respectively, for a 4-ary spherical lens optimized considering four unit cells with $Amplitude_{1\text{-}4}$=0.8, $Phase_1$=0 rads, $Phase_2$=π/6 rads, $Phase_3$=π/3 rads, $Phase_4$=π/2 rads. **(d,e,f)** Idem, with unit cells designed with $Amplitude_{1\text{-}4}$=0.8, $Phase_1$=0 rads, $Phase_2$=π/3 rads, $Phase_3$=2π/3 rads, $Phase_4$=π rads. **(g,h,i)** Idem, with unit cells designed with $Amplitude_{1\text{-}4}$=0.8, $Phase_1$=0 rads, $Phase_2$=π/2 rads, $Phase_3$=π rads, $Phase_4$=3π/2 rads.

These 4-ary SOLs show the same observed tradeoff between the spot size and the side lobes level (lower *FWHM* implies lower *NLPS*). It is also shown the same enhancement boost when the phase retardation step surpases certain value, but, contrary to the binary case, the NLPS is improved too. It is important to remark that this boost to NLPS values observed for 4-ary studies is not due to a reduction in the attainable focal size (unlike the binary case, the mean focus size does not vary statistically) but to a higher yield (the energy concentration in the airy disk with respect to all the transverse plane becomes higher).

To conclude the analysis of these 4-ary SOLs, in table 3.6. the minimum and maximum values at the hotspot are shown.

4-ary SOLs					
#	**Amplitude**	**Phases**	**$FWHM_{X,Y}$ (λ)**	**NLPS (dB)**	**Enhancement (dB)**
4	0.8	[0, π/6, π/3, π/2]	0,364 – 0,482	8,06 – 12,27	13,68 – 20,62
5	0.8	[0, π/3, 2π/3, π]	0,360 – 0,479	7,95 – 12,40	14,59 – 23,49
6	0.8	[0, π/2, π, 3π/2]	0,361 – 0,486	8,04 – 13,01	15,84 – 23,37

Table 3.6. Variation range for the different parameters studied in the three different 4-ary SOLs explored.

Next, the analytical results obtained for 8-ary and 16-ary lenses are plotted in Fig. 3.14 (along with the best binary and 4-ary results, for comparison sake). The trend observed before continues in this 8- and 16-ary SOLs: The size of the attainable hotspot is preserved while the Enhancement mean value clearly rises (it is important to observe that neither the lower nor the higher values actually rise too much, but the mean value does). For the sake of completeness, the extreme values attainable for the hotspot's parameters are shown in Table 3.7 while the mean values for all the cases considered can be observed in Fig. 3.13.

Binary SOL – Best case					
#	**Amplitude**	**Phases**	**FWHM$_{X,Y}$ (λ)**	**NLPS (dB)**	**Enhancement (dB)**
3	0.8	[0, π]	0,359 – 0,474	7,79 – 11,61	13,64 – 21,89
4-ary SOL – Best case					
#	**Amplitude**	**Phases**	**FWHM$_{X,Y}$ (λ)**	**NLPS (dB)**	**Enhancement (dB)**
6	0.8	[0, π/2, π, 3π/2]	0,361 – 0,486	8,04 – 13,01	15,84 – 22,97
8-ary SOL					
#	**Amplitude**	**Phases**	**FWHM$_{X,Y}$ (λ)**	**NLPS (dB)**	**Enhancement (dB)**
7	0.8	[0, π/4, … 7π/4]	0,363 – 0,490	7,82 – 12,89	15,73 – 23,89
16-ary SOL					
#	**Amplitude**	**Phases**	**FWHM$_{X,Y}$ (λ)**	**NLPS (dB)**	**Enhancement (dB)**
8	0.8	[0, π/8, …15π/8]	0,362 – 0,488	8,10 – 12,56	15,64 – 23,73

Table 3.7. Extreme values for the different parameters studied in the n-ary SOLs considered.

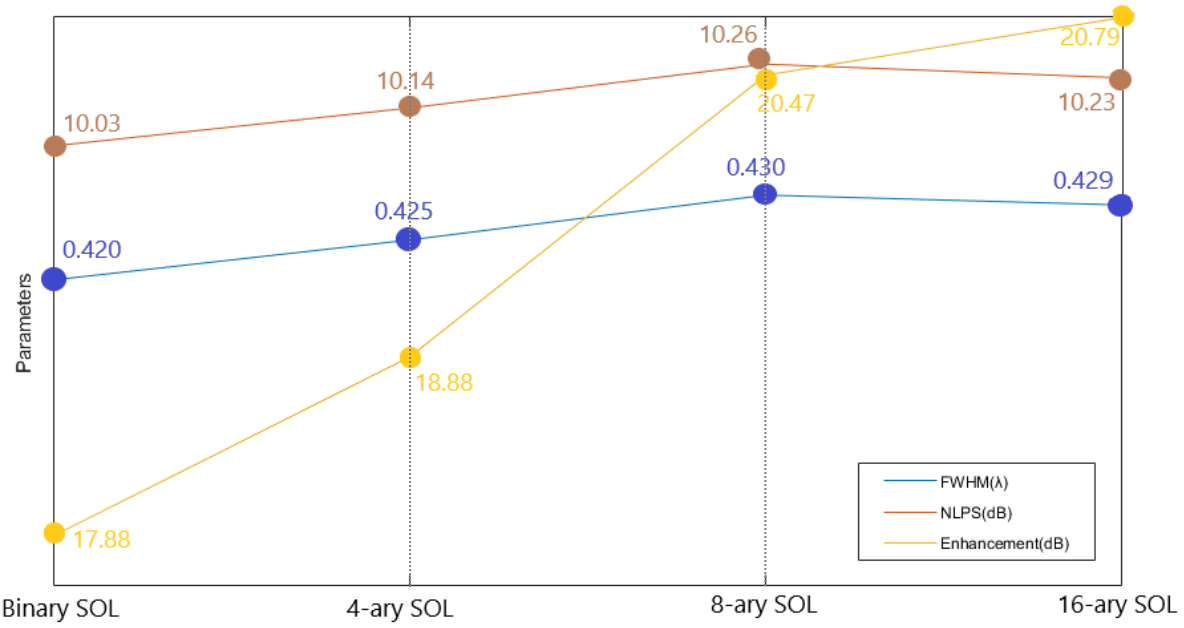

Figure 3.13. Mean values for the different parameters studied in the 2-, 4-, 8- and 16-ary SOLs.

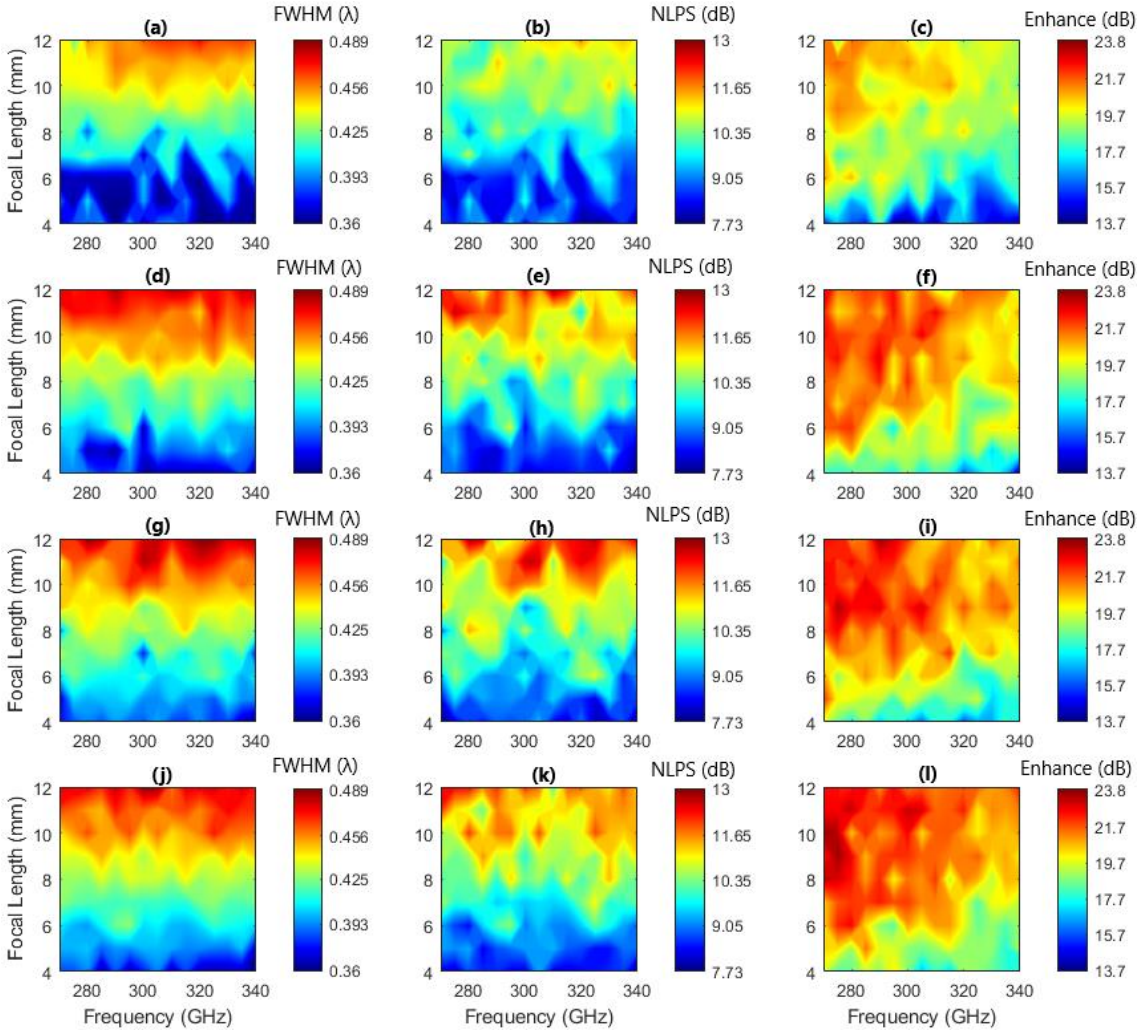

Figure 3.14. **(a,b,c)** Analytical results for $FWHM_{x,y}$ (normalized to λ), NLPS (dB) and enhancement (dB), respectively, for a binary spherical lens optimized considering two unit cells with $Amplitude_{1,2}$=0.8, $Phase_1$=0 rads and $Phase_2$=π rads. **(d,e,f)** Idem, for a 4-ary spherical lens whose unit cells are designed with $Amplitude_{1\text{-}4}$ =0.8, $Phase_1$=0 rads, $Phase_2$=π/2 rads, $Phase_3$=π rads, $Phase_4$=3π/2 rads. **(g,h,i)** Idem, for a 8-ary spherical lens whose unit unit cells are designed with $Amplitude_i$=0.8 and $Phase_i$= (*i*-1)π/4 rads, (*i*=1…8). **(j,k,l)** Idem, for a 16-ary spherical lens whose unit cells are designed with $Amplitude_j$=0.8 and $Phase_j$= (*j*-1)π/8 rads (*j*=1…16).

It can be observed in Fig. 3.13 that when the phase difference between the metamolecules is maximized (that is, the phase responses are equally distributed in the [0, 2π] range), there is a linear relationship between the mean size of the focus and the mean level of the secondary lobes, while the enhancement is improved when a bigger number of phase discretization states is considered.

Thus, applying metasurfaces to superoscillatory lenses enabling flexible control of the phase through multiples metamolecules with different transmission phase, helps improving the efficiency, which is one of the most challenging issues in this kind of devices. Our high-transmission phase-modulation metasurfaces stand therefore as candidates for overcoming this limitation of super-oscillatory lenses.

3.2.2 Amplitude and phase gradient-index meta-SOLs.

This section will explore the combination of unit cells with multiple levels of high transmission amplitude and different phase retardation values. Therefore, we will study the possible trade-off between slightly decreasing the lens efficiency and the attainable focal parameters.

A 64-ary metaSOL (that is, 64 possible unit cells) based on a combination of 8 different phase and amplitude levels will be implemented. The 8 possible amplitude levels are $A_i = 0.94 - (i-1)\times 0.04$ a.u. (i=1…8) and the 8 different phase values are $Phase_i = (i-1)\times\pi/4$ rads, (i=1…8).

Our GA code is modified to add the new metamolecules, but the same basic optimization process is carried on. The results obtained are shown in Fig. 3.15, where they are compared to the results already obtained and the results of Sec. 3.2.3. The discussion of all these results is done in the next section, for the sake of clarity.

3.2.3 A brief study on the effect of micro-pixelating a SOL

In this section, the overall effect of using smaller unit cells is studied. The full metalens size is kept and each zone is now more finely pixelated. Previous studies [100] about the effect of pixelation on focusing performance concluded that a thicker pixelation mainly increases the sidelobe level. The purpose of this section is to investigate the effect of reducing the pixel (i.e. the unit cell) on the sidelobe level or other parameters. The pixelation ratio will be 3.5:1 compared to the previous studies.

Regarding the GA, the finer pixelation implies that any chromosome is now composed of 251 different genes (each gen being a metamolecule, the addition of which conforms the half side of a cylindrical lens) instead of the 72 genes considered originally. The distance between metamolecules is 100 μm (instead of 350 μm). The same strategy already explained in previous chapters will be used here: each of the chromosome´s 251 binary dimensions is considered a source-point that radiates a wave with the same amplitude and phase to the corresponding S21 coefficient considered. The effect of micro-pixelating are studied for 8- and 16-ary designs and the results obtained are shown in Fig. 3.15, along with the 8-, 16- and 64-ary results from the previous sections for comparison purpose.

The effect of micropixelating the lens by a factor 3.5:1 inmediately boost the mean enhancement by a factor of nearly 12% and the mean NLPS by 6%, when the 8-ary and 16-ary metaSOLs are compared to their micropixelated equivalents. For illustration purposes, Fig. 3.16 shows the variation of the mean FWHM, NLPS and enhancement values for different target focal lengths (i.e. for FL = 4mm, the mean FWHM is the average value of FWHM for the SOLs designed with central frequency 270, 275 … 340 GHz and with the specified FL). The mean absolute values for the parameters studied can be observed in Fig. 3.17. From these two last figures, we can observe the almost linear relationship between the FWHM and the NLPS with the focal length; in Fig. 3.16c, it is interesting to note that the enhancement curve is nonlinear. In fact, around FL = 8mm, the curve becomes asymptotic and the enhancement saturates. It is interesting too that the mean results obtained with the 8-ary and 16-ary micropixelated versions differ very little.

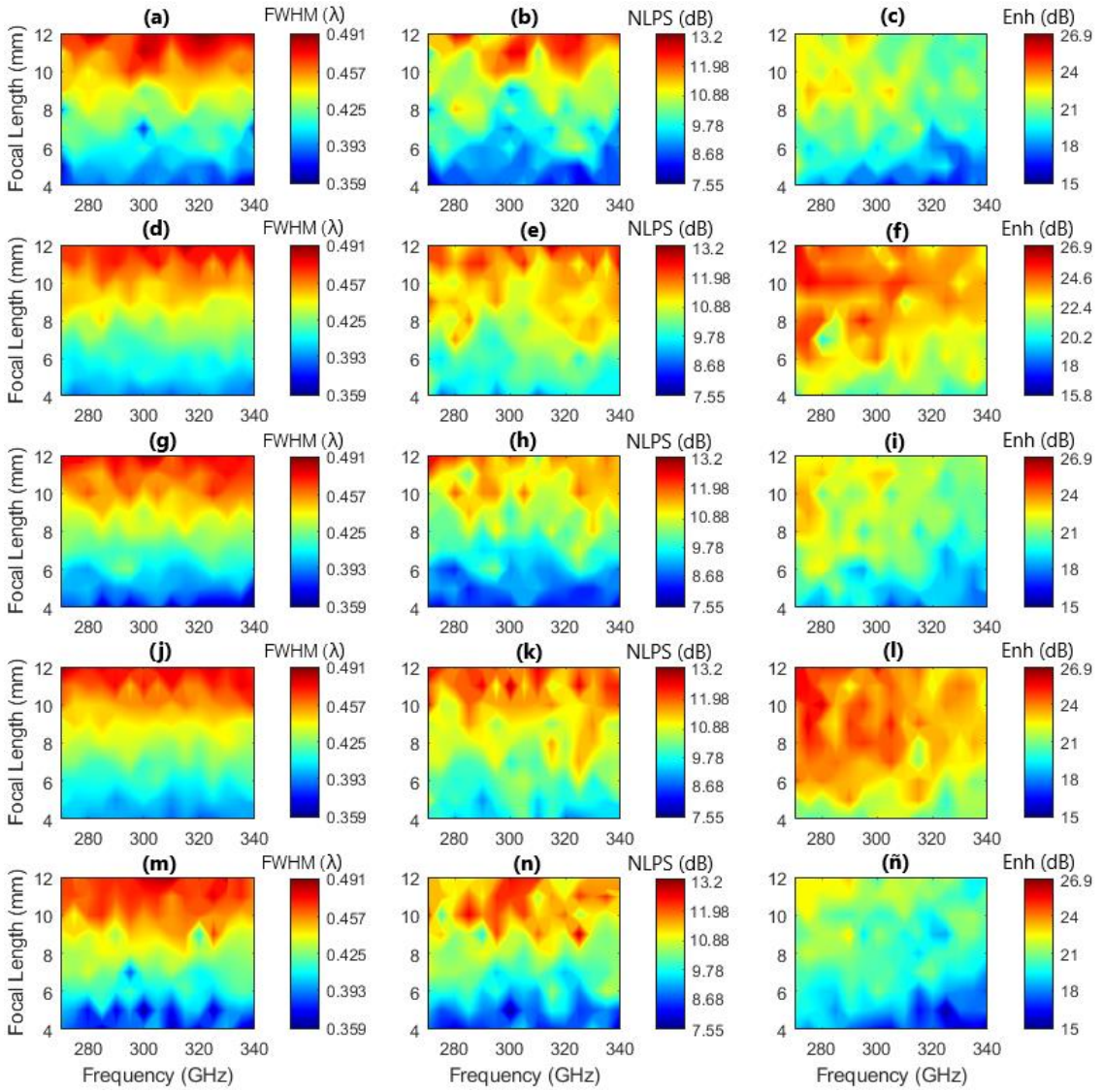

Figure 3.15. **(a,b,c)** Analytical results for $FWHM_{x,y}$ (normalized to λ), NLPS (dB) and enhancement (dB), respectively, for a 8-ary spherical lens whose unit cells are designed with $Amplitude_i$=0.8 and $Phase_i$= (i-1)π/4 rads, (i=1…8). **(d,e,f)** Idem, for a 8-ary micropixelated spherical lens considering the same unit cells than the 8-ary case. **(g,h,i)** Idem, for a 16-ary spherical lens whose unit cells are designed with $Amplitude_j$=0.8 and $Phase_j$= (j-1)π/8 rads (j=1…16). **(j,k,l)** Idem, for a 16-ary micropixelated spherical lens considering the same unit cells than the 16-ary case. **(m,n,ñ)** Idem, for a 64-ary spherical lens whose unit cells are a combination of 8 possible amplitude levels (0.94, 0.90, 0.86, 0.82, 0.78, 0.74, 0.72, 0.68) and 8 different phase values, $Phase_i$= (i-1)π/4 rads, (i=1…8).

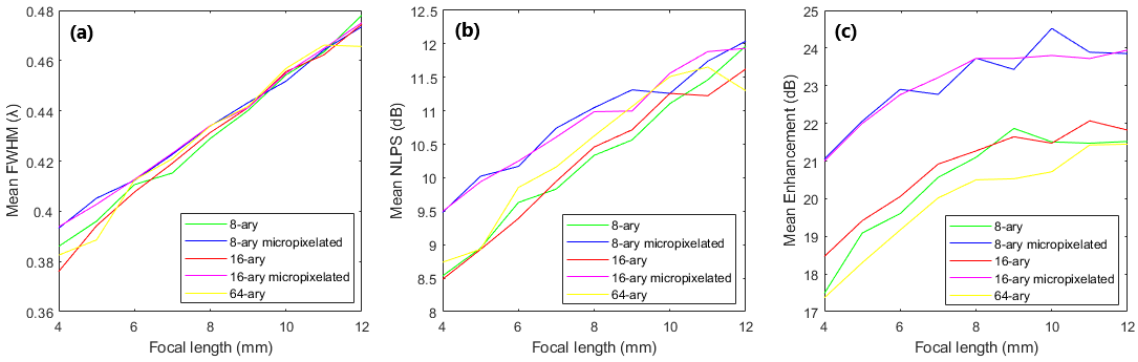

Figure 3.16. **(a)** Variation of the mean FWHM (normalized to λ) with the focal length (mm) for the 5 different metaSOLs studied in this section, **(b)** Idem, for the mean NLPS (dB), **(c)** Idem, for the mean Enhancement (dB).

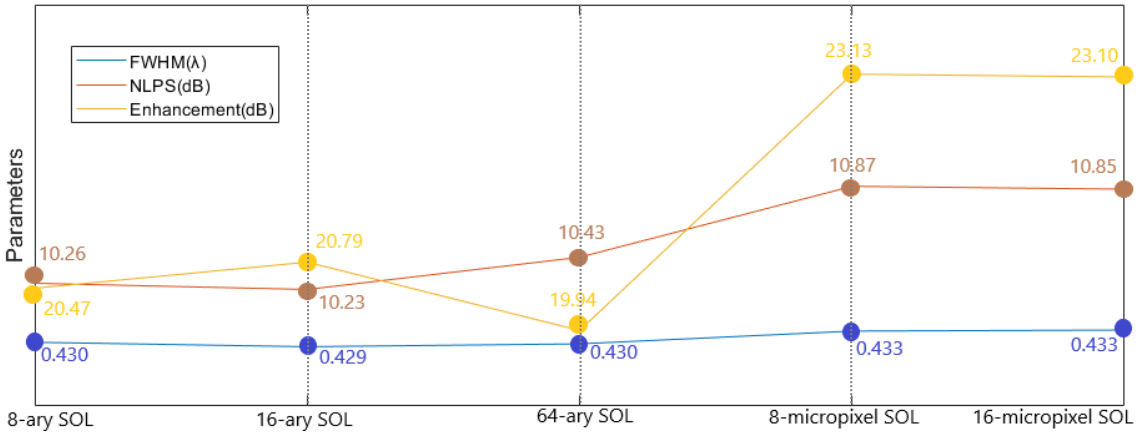

Figure 3.17. Mean values for the different parameters studied in the 8-, 16-, 64-ary SOLs and the micropixelated versions of the 8- and 16-ary SOLs.

Regarding the effect of using unit cells with multiple levels of amplitude and phase, the expected drop in the enhancement is observed and a tradeoff occurs between the NLPS and the enhancement, as can be seen in Fig. 3.17. The most intuitive way of comparing this lens is with the 8-ary version (since both share the same 8 phase levels).

Until now we have focused on achieving the best performance with the essential requirement of locating the hotspot where the field is more concentrated. This methodology limits the attainable focus size because it is a well-known issue in super-oscillatory devices that sharper foci are related to low intensity zones. In the next section we will study the size and properties of the focal parameters attainable when our design criteria is modified from a scheme that balances the different parameters prioritizing the electric field enhancement to a scheme where the focus size is prioritized.

3.2.4 Focal characterization

The first purpose of this section is to study the size of the hotspot and its properties with the different *n*-ary designs presented so far. Next, we will focus on the 8-ary lens and study its focal parameters at f = 280 GHz and $FL = 10\lambda_0$.

To finish this section, we will focus on the frequency of f = 300 GHz and a focal length of $FL = 8\lambda_0$ to carry out three different studies with respect to all the *n*-ary designs seen: 1) A study looking for the narrowest possible foci. 2) A study that will search for the properties of the foci with target FWHM between $0.360\lambda_0$ and $0.370\lambda_0$. 3) A study to search for foci with target FWHM between $0.420\lambda_0$ and $0.430\lambda_0$.

Study of achievable focus sizes

Another Analytical Optimization study is launched with the same frequency and *FL* sweep (f = 270, 275, …, 340 GHz & FL = 4, 5, … 12 mm).

In Fig. 3.18 the histograms of the foci size attained, for the different designs considered, are presented (limited to FWHM < $0.20\lambda_0$).

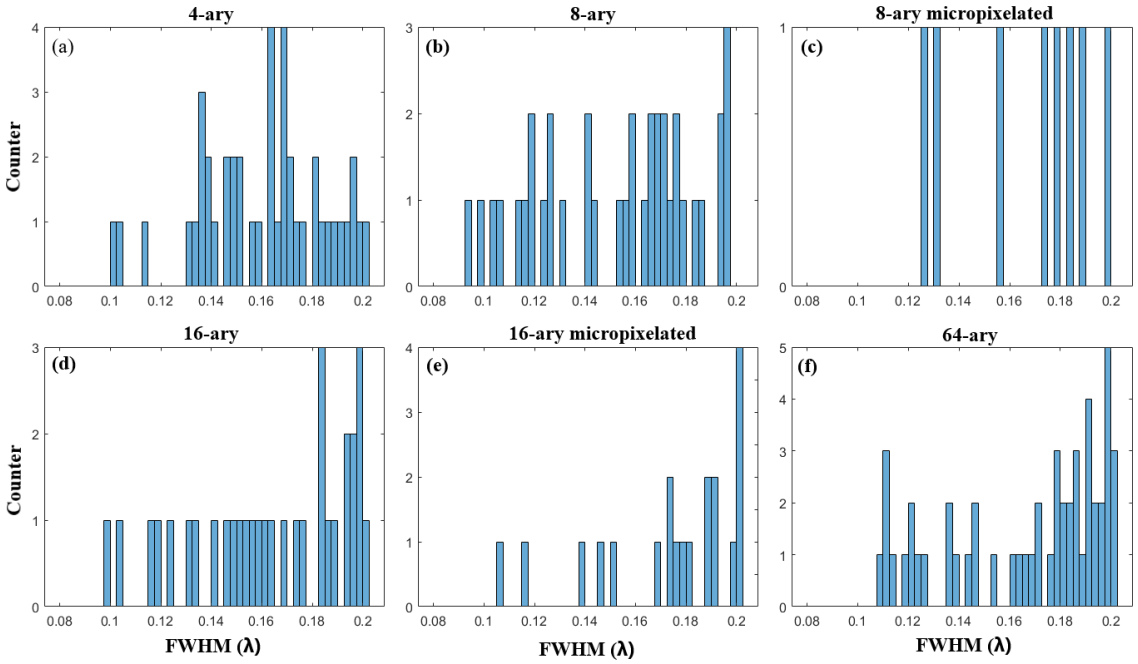

Figure 3.18. Histograms showing the number of cases and size of the foci sharper than $0.20\lambda_0$ obtained for different designs: **(a)** 4-ary SOL (constant amplitude and equally spaced phase respones in the full 2π rads range), **(b)** 8-ary SOL (idem). **(c)** 8-ary micropixelated SOL (idem). **(d)** 16-ary SOL (idem). **(e)** 16-ary micropixelated SOL (idem). **(f)** 64-ary SOL (8 amplitude levels (0.94, 0.90, 0.86, 0.82, 0.78, 0.74, 0.72, 0.68) and 8 phase values equally spaced in the full 2π range).

To analyze the results presented in Fig. 3.18, we will add the total number of cases in Table 3.8 to get a view about the ability of a particular design to obtain a very narrow focus.

SOL design	4-ary	8-ary	16-ary	8-ary µpxl	16-ary µpxl	64-ary
Cases	44	36	27	8	20	52

Table 3.8. Number of foci sharper than $0.20\lambda_0$ satisfactorily achieved in the study (each SOL scheme is evaluated through 15 different frequencies and 9 different focal lengths, adding 135 possible combinations).

Observing the count of cases for the 4-, 8- and 16-ary SOLs, it is evident that the ability to achieve better levels of enhancement goes hand in hand with the decrease in the probability of achieving narrow foci, as it has been reported in the literature [42, 45,45, 49, 101]. Moreover, this effect is even more sharply observed in the case of the two micro-pixelated designs, although the 16-ary version clearly shows a better probability of obtaining sharper focus (the opposite happens in the non-micro-pixelated counterparts). Finally, it should be noted that the 64-ary design gets the greatest number of narrow hotspots: Thus, increasing the number of phase and amplitude values can improve the chance of getting sharper focus while improving the sidelobes level at the same time at the cost of a low reduction of the lens efficiency.

Study of an 8-ary lens

As can be seen in Fig. 3.18, the sharpest foci are obtained with the 8-ary design. In this section we will focus on this design and will study its focal parameters at f = 280 GHz and $FL = 10\lambda_0$ for different target FWHM values. The results are shown in Fig. 3.19 and Table 3.9:

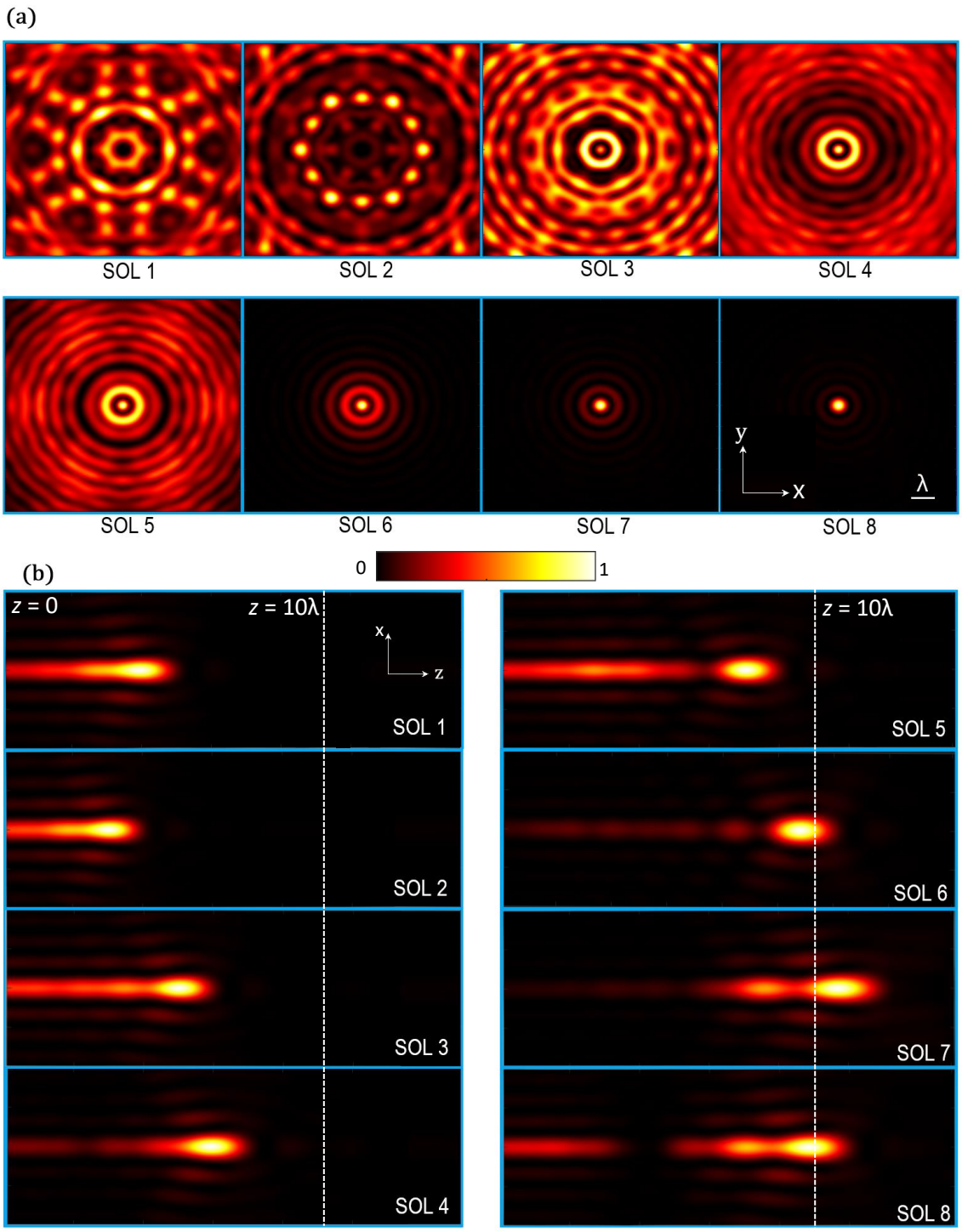

Figure 3.19. (a) Normalized diffraction pattern in the *xy*-plane ($z = 10\lambda_0$) and (b) normalized power distribution on the longitudinal *xz*-plane, produced by vertically polarized radiation (λ = 1.07 mm) diffracting from the 8 different 8-ary SOL designs explained in Table 3.9.

8-ary SOLs	FWHM	NLPS (dB)	Enhancement (dB)	FOV
SOL 1	$0.10\lambda_0$	-25.2	-86.9	$0.61\lambda_0$
SOL 2	$0.20\lambda_0$	-10.5	-73.3	$0.82\lambda_0$
SOL 3	$0.30\lambda_0$	-1.8	-36.6	$1.53\lambda_0$
SOL 4	$0.33\lambda_0$	0.6	-18.3	$1.77\lambda_0$
SOL 5	$0.36\lambda_0$	0.8	-3.6	$2.00\lambda_0$
SOL 6	$0.39\lambda_0$	4.1	9.1	$2.15\lambda_0$
SOL 7	$0.43\lambda_0$	8.1	19.6	$>50\lambda_0$
SOL 8	$0.45\lambda_0$	11.8	20.9	$>50\lambda_0$

Table 3.9. Focal parameters for the different target FWHM values at f = 280GHz and $FL = 10\lambda_0$. each SOL identifier is related to its equivalence in Fig. 3.19. All the designs are 8-ary, but, of course, the solution is different in each case.

The most relevant aspect is that, as have been proven, very narrow hotspots can be designed at will, until a certain point. Given a certain frequency and focal length, the achievable focal parameters vary a lot from one design to another. This will be studied in the next sections.

Search for the sharpest foci

To make a comparison possible and to establish an objective framework, a full relation of all the designs analyzed in this work are summarized here and used to optimize the sharpest foci attainable for each design at the central frequency f = 300GHz and at $FL = 8\lambda_0$. The results obtained are shown in Table 3.10 and Fig. 3.20.

	DESIGN	FWHM	NLPS (dB)	Enhancement (dB)	FOV
a	BINARY A	$0.249\lambda_0$	-6.8	-48.9	$0.64\lambda_0$
b	BINARY B	$0.240\lambda_0$	-1.3	-52.6	$0.66\lambda_0$
c	BINARY C	$0.198\lambda_0$	-12.6	-56.0	$0.42\lambda_0$
d	4-ARY A	$0.233\lambda_0$	-11.6	-51.8	$0.62\lambda_0$
e	4-ARY B	$0.209\lambda_0$	-11.7	-48.6	$0.42\lambda_0$
f	4-ARY C	$0.183\lambda_0$	-15.0	-42.9	$0.24\lambda_0$
g	4-ARY µpxl	$0.197\lambda_0$	-12.2	-35.4	$0.28\lambda_0$
h	8-ARY	$0.181\lambda_0$	-13.7	-41.4	$0.44\lambda_0$
i	8-ARY µpxl	$0.184\lambda_0$	-12.8	-35.9	$0.42\lambda_0$
j	16-ARY	$0.184\lambda_0$	-11.6	-36.8	$0.44\lambda_0$
k	16-ARY µpxl	$0.186\lambda_0$	-11.7	-39.3	$0.42\lambda_0$
l	64-ARY	$0.120\lambda_0$	-18.9	-73.2	$0.28\lambda_0$

Table 3.10. Focal parameters for the sharpest FWHM values obtained, at f = 300GHz and $FL = 8\lambda_0$, for different designs: **(a)** Binary SOL with $Amplitude_{1,2}$=0.8, $Phase_1$=0 rads and $Phase_2$=π/3 rads. **(b)** Binary SOL with same amplitude and $Phase_1$=0 rads and $Phase_2$=2π/3 rads. **(c)** Binary SOL with same amplitude and $Phase_1$=0 rads and $Phase_2$=π rads. **(d)** 4-ary SOL with $Amplitude_{1\text{-}4}$=0.8, $Phase_i$= (i-1)π/6 rads, (i=1…4). **(e)** 4-ary SOL with same amplitude and $Phase_i$= (i-1)π/3 rads, (i=1…4). **(f)** 4-ary SOL with same amplitude and $Phase_i$=(i-1)π/2 rads, (i=1…4). **(g)** 4-ary micropixelated SOLs with the same unit cells as case f. **(h)** 8-ary SOL with Amplitudei=0.8 and $Phase_i$= (i-1)π/4 rads, (i=1…8). **(i)** 8-ary micropixelated SOL. **(j)** 16-ary SOL $Amplitude_i$=0.8 and $Phase_i$= (i-1)π/8 rads (j=1…16). **(k)** 16-ary micropixelated SOL. (l) 64-ary SOL with 8 possible amplitude levels (0.94, 0.90, 0.86, 0.82, 0.78, 0.74, 0.72, 0.68) and 8 different phase values, $Phase_i$= (i-1)π/4 rads, (i=1…8).

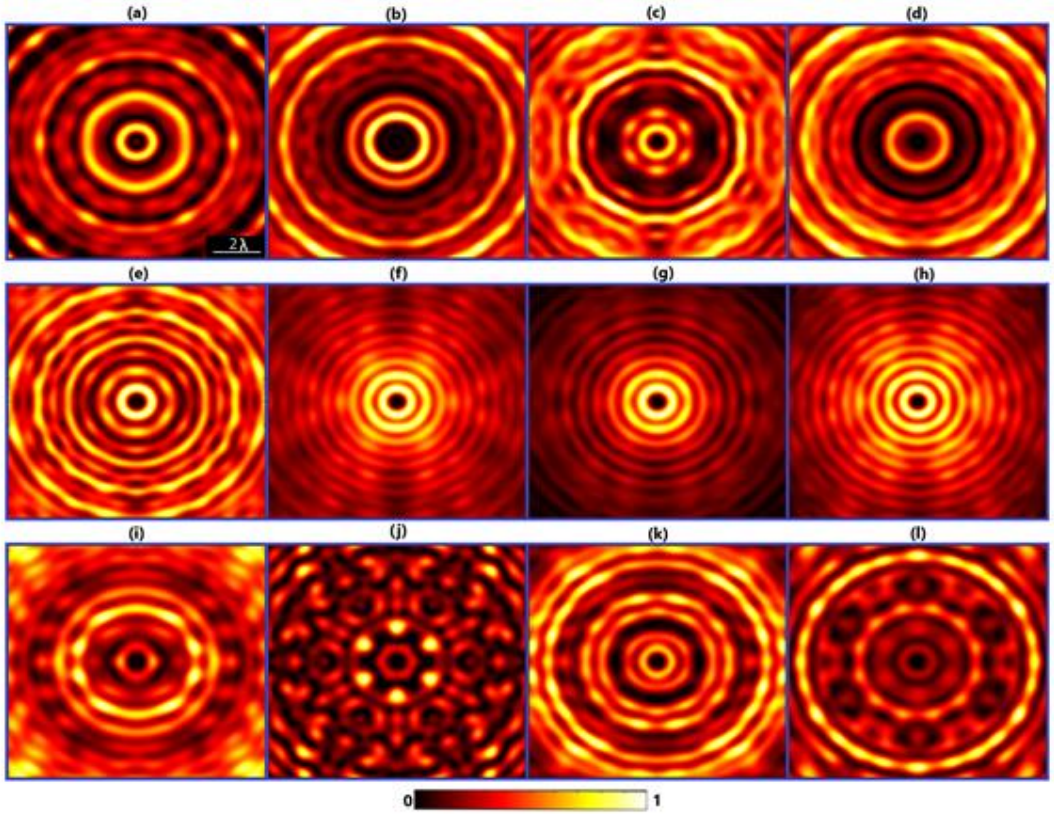

Figure 3.20. Normalized power map in the *xy*-plane ($z = 8\lambda_0$) produced by vertically polarized radiation (λ = 1mm) diffracting from the 16 different metaSOLs explained in Table 3.10. The different subindices are related to its equivalence in Table. 3.10. (i.e, (l) refers to the 64-ary SOL).

Table 3.10 shows clearly that increasing the number of phase and amplitude values improves the chance of getting sharper focus, but it is also observed the exponential decay in other focal parameters when the foci become narrower. The 64-ary SOL success in getting the narrower focus for the imposed conditions.

Search for other interesting foci

To end this study and enable a comprehensive comparison of the different designs, this section will show the optimizations done to obtain foci between a narrow range: First, foci between $[0.420\lambda_0, 0.429\lambda_0]$ will be forced at the central frequency f = 300GHz and at $FL = 8\lambda_0$ and the focal parameters will be compared. Next, foci between $[0.360\lambda_0, 0.369\lambda_0]$ will be forced at the same conditions. The results obtained are shown in Table 3.11 while the *xy*-diffraction patterns achieved for the second case are shown in Fig. 3.21 (in the first case, that is, FWHM is between $[0.420\lambda_0, 0.429\lambda_0]$, the *xy*-plane maps obtained are not interesting because they merely correspond to an airy disk, very similar to the SOL8 case shown in Fig. 3.19).

	DESIGN	FWHM	NLPS (dB)	Enhancement (dB)	FOV
a	BINARY A	$0.423\lambda_0$	10.3	16.4	$>50\lambda_0$
b	BINARY B	$0.420\lambda_0$	9.9	20.3	$>50\lambda_0$
c	BINARY C	$0.423\lambda_0$	10.4	18.3	$>50\lambda_0$
d	4-ARY A	$0.425\lambda_0$	10.2	18.7	$>50\lambda_0$
e	4-ARY B	$0.428\lambda_0$	10.0	21.0	$>50\lambda_0$
f	4-ARY C	$0.426\lambda_0$	9.9	21.4	$>50\lambda_0$
g	4-ARY µpxl	$0.425\lambda_0$	9.8	22.0	$>50\lambda_0$
h	8-ARY	$0.429\lambda_0$	10.8	20.5	$>50\lambda_0$
i	8-ARY µpxl	$0.428\lambda_0$	10.2	22.9	$>50\lambda_0$
j	16-ARY	$0.425\lambda_0$	10.3	21.8	$>50\lambda_0$
k	16-ARY µpxl	$0.422\lambda_0$	10.4	23.2	$>50\lambda_0$
l	64-ARY	$0.423\lambda_0$	10.0	20.1	$>50\lambda_0$

	DESIGN	FWHM	NLPS (dB)	Enhancement (dB)	FOV
a	BINARY A	$0.363\lambda_0$	4.9	2.9	$1.14\lambda_0$
b	BINARY B	$0.366\lambda_0$	5.0	4.6	$1.14\lambda_0$
c	BINARY C	$0.363\lambda_0$	5.4	4.5	$1.14\lambda_0$
d	4-ARY A	$0.370\lambda_0$	5.4	6.6	$1.16\lambda_0$
e	4-ARY B	$0.369\lambda_0$	5.2	8.0	$1.14\lambda_0$
f	4-ARY C	$0.367\lambda_0$	5.1	8.4	$1.12\lambda_0$
g	4-ARY µpxl	$0.367\lambda_0$	5.8	9.8	$1.18\lambda_0$
h	8-ARY	$0.362\lambda_0$	4.6	9.9	$1.10\lambda_0$
i	8-ARY µpxl	$0.368\lambda_0$	5.2	14.4	$1.14\lambda_0$
j	16-ARY	$0.369\lambda_0$	5.6	10.9	$1.18\lambda_0$
k	16-ARY µpxl	$0.368\lambda_0$	6.3	13.5	$>50\lambda_0$
l	64-ARY	$0.364\lambda_0$	5.8	11.5	$1.22\lambda_0$

Table 3.11. Focal parameters for the explicited FWHM target ranges at f = 300GHz and $FL = 8\lambda_0$, for different designs: **(a)** Binary SOL with $Amplitude_{1,2}$=0.8, $Phase_1$=0 rads and $Phase_2$=π/3 rads. **(b)** Binary SOL with same amplitude and $Phase_1$=0 rads and $Phase_2$=2π/3 rads. **(c)** Binary SOL with same amplitude and $Phase_1$=0 rads and $Phase_2$=π rads. **(d)** 4-ary SOL with $Amplitude_{1\text{-}4}$=0.8, $Phase_i$= (i-1)π/6 rads, (i=1…4). **(e)** 4-ary SOL with same amplitude and $Phase_i$= (i-1)π/3 rads, (i=1…4). **(f)** 4-ary SOL with same amplitude and $Phase_i$=(i-1)π/2 rads, (i=1…4). **(g)** 4-ary micropixelated SOLs with the same unit cells as case f. **(h)** 8-ary SOL with Amplitudei=0.8 and $Phase_i$= (i-1)π/4 rads, (i=1…8). **(i)** 8-ary micropixelated SOL. **(j)** 16-ary SOL $Amplitude_i$=0.8 and $Phase_i$= (i-1)π/8 rads (j=1…16). **(k)** 16-ary micropixelated SOL. (l) 64-ary SOL with 8 possible amplitude levels (0.94, 0.90, 0.86, 0.82, 0.78, 0.74, 0.72, 0.68) and 8 different phase values, $Phase_i$= (i-1)π/4 rads, (i=1…8).

For the $[0.429\lambda_0, 0.429\lambda_0]$ FWHM range, the difference between the designs is usually small, although it is observed the expected tendency to obtain a greater enhancement as the number of phase states considered increases. When the focal size restrictions are much more demanding (i.e, the FWHM is in the $[0.360\lambda_0, 0.369\lambda_0]$ range, the improvement found in the focal parameters, mainly the enhancement, is much more evident, being it possible to find improvements of factor 2-3 in the enhancement between the binary case and the high order designs.

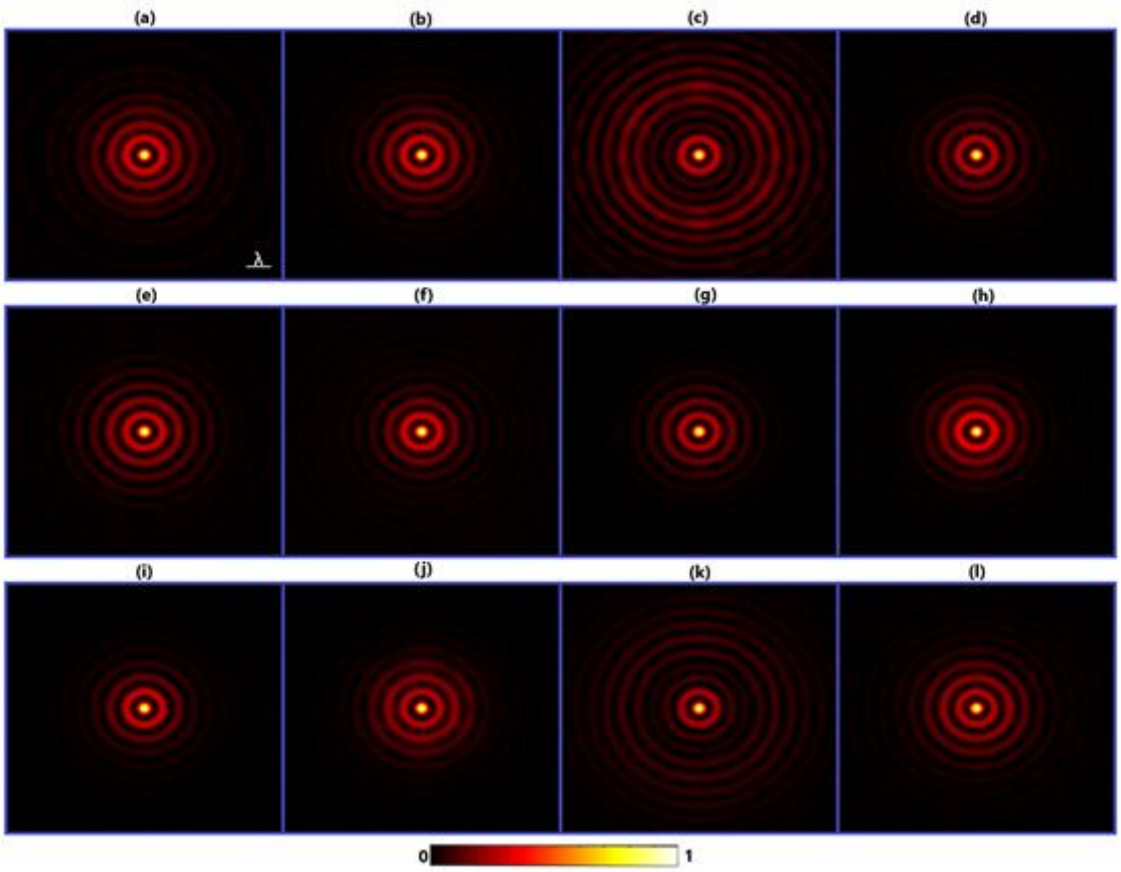

Figure 3.21. Normalized power map in the *xy*-plane ($z = 8\lambda_0$) produced by vertically polarized radiation (λ = 1mm) diffracting from the 16 different metaSOLs explained in Table 3.11 corresponding to the FWHM target range of $[0.360\lambda_0, 0.369\lambda_0]$. The different subindex are related to its equals in Table. 3.11. (i.e, (l) refers to the 64-ary SOL).

4. Conclusions and future work

In this chapter, a summary of the conclusions obtained during this work along with a list of future lines to be done in the future to give continuity to this work are presented.

4.1 Conclusions

1. In this work, we have engineered and evaluated analytically, numerically and experimentally a THz binary super-oscillatory metalens with the aim to improve the magnitude of the E-field at the focal spot with a reduction of its side lobes. As a result, an ultrathin metalens with thickness around 0.04λ0 has been demonstrated at 0.327 THz. The simulated focal spot had an average of 0.47λ0, being the sidelobes intensity less than 10% of the focal spot intensity while the enhancement was 16.6dB. The experimental measures shows that there are hotspots that clearly surpass the simulated enhancement and that are very close to the NLPS value (around 15% of the focal spot intensity).

2. Regarding the efficiency, the fabricated meta-SOL has been experimentally measured with the Vector Network Analyzer (VNA) model Agilent N5242A available in the UPNA's THz laboratory. Although the measurement process has been been abruptly interrupted by the outbreak of the Covid-19 pandemic, there are enough available measurements to show that the meta-SOL succesfully generates a narrow hotspot with reduced side lobes and high enhancement, demostrating that the ingenious use of metasurfaces helps overcome the actual SOLs' lack of focusing efficiency. When the largest-sized state-of-the-art SOLs shows a focusing efficiency of only 5% at most, in our design the energy concentrated in the central hotspot is shown to be larger than 7%.

3. We have evaluted the combination of graded-index (GRIN) and super-oscillation (SO) concepts to improve the original binary meta-SOL. The study has been carried out through an extense analytical process of optimization. The proposed super-oscillatory pseudo-graded-index metalens design offers a new technique to improve the focusing properties attainable with the state-of-the-art SOLs.

4. It has been shown that increasing the number of phase and amplitude values (and thus, considering a *n*-ary meta-SOL, $n>2$) can improve the chance of getting sharper focus boosting the sidelobes level. The most relevant aspect is that very narrow hotspots can be designed at will but, given a certain frequency and focal length, the achievable focal parameters vary a lot from one design to another so a carefully balancing engineering must be carried on, because it has been observed the exponential decay in the focal parameters when the foci become narrower. The 64-ary SOL (highest order meta-SOL studied) success in getting the narrower focus for the imposed conditions.

5. When the focal size restrictions are increasingly demanding (the FWHM becomes narrower), the improvement found in the focal parameters, mainly the enhancement, is much more evident, being it possible to find improvements of factor 2-3 in the enhancement between the binary case and the high order designs. Regarding the effect of micropixelating the meta-SOL by a factor 3.5:1, it inmediately boosts the mean enhancement by a factor of nearly 12% and the mean NLPS by 6% among the 8-ary and 16-ary metaSOLs and their micropixelated counterparts.

4.2 Future work

1. Resuming and finishing the measurement process of the constructed meta-SOL, interrupted for the time being by the outbreak of the Covid-19 pandemic.

2. Combining deep learning and pseudo-graded-index meta-SOLs as a rapid and efficient route to automatic improved designs.

3. Studing the design of different reconfigurable devices at the THz range using liquid crystal technology.

5. Bibliography and references

[1] E. T. F. Rogers, J. Lindberg, T. Roy, S. Savo, J. E. Chad, M. R. Dennis, N. I. Zheludev, Nature Materials, (5), pp-432-435, March 2012.

[2] E. T. F. Rogers, and N. I. Zheludev, Journal of Optics, (15), pp-094008-1-23, 2013.

[3] G. Yuan, E. T. F. Rogers, T. Roy, Z. Shen and N. I. Zheludev, Optics Express, (22), pp 6428-6437.

[4] N. Jin Y., Rahmat-Samii, "Advances in particle swarm optimization for antenna designs: Real-number binary single-objective and multiobjective implementations" IEEE Trans. Antennas Propag. vol. 55 pp. 556-567, 2007.

[5] R.P. Feynman. L.B. Leighton, M. Sands, “Lectures of Physics”, Addison-Wesley Publishing Company (1964).

[6] D. A. Hill, “Electromagnetic Fields in Cavities Deterministic and Statistical Theories”, IEEE Press Series on Electromagnetic Wave Theory (2009).

[7] “Permitividad”, available at http://iupsm.files.wordpress.com/2010/08/permitividad.pdf. [Online]. [Accessed: 8-may-2017].

[8] M. V. Akhterov, “Microwave Absorption in Nanostructures”, Doctoral thesis (2010).

[9] V. Komarov, S. Wang, J. Tang, “Permittivity and Measurements”, Encyclopedia of RF and Microwave Engineering, 308 1-20 (2004).

[10] R.C. Dorf. “Electrical Engineering Handbook”, Crc. Press (1997).

[11] G.W.C Kaye, T.H Laby, “Physical and Chemical Constants” (2003).

[12] J. A. Kong, “Electromagnetic Wave Theory”, John Wiley & Sons (1986).

[13] V. Pacheco-Peña (2016), “Metamaterials and plasmonics applied to devices based on periodic structures at high frequencies: microwaves, terahertz and optical range” (doctoral thesis), Universidad Pública de Navarra, Pamplona.

[14] R. Marqués, F. Martín, and M. Sorolla, Metamaterials with Negative Parameters: Theory, Design, and Microwave Applications (John Wiley & Sons, 2008).

[15] J. B. Pendry, A. J. Holden, D. J. Robbins and W. J. Stewart, "Magnetism from conductors and enhanced nonlinear phenomena," in IEEE Transactions on Microwave Theory and Techniques, vol. 47, no. 11, pp. 2075-2084, Nov 1999.

[16] V. Veselago, “The electrodynamics of substances with simultaneously negative values of ε and μ”. Sov. Phys. Usp. 10(4): 509-14, 1968.

[17] B. Orazbayev (2016), “Advanced metamaterials for high resolution focusing and invisibility cloaks” (doctoral thesis), Universidad Pública de Navarra, Pamplona.

[18] D. F. Filipovic, S. S. Gearhart and G. M. Rebeiz, “Double-slot antennas on extended hemispherical and elliptical silicon dielectric lenses,” IEEE Transactions on Microwave Theory and Techniques, 41, 10 (1993).

[19] S. Raman, N. S. Barker and G. M. Rebeiz, “A W-band dielectric-lens-based integrated monopulse radar receiver,” IEEE Transactions on Microwave Theory and Techniques, 46, 12 (1998).

[20] J. B. Pendry, "Negative Refraction Makes a Perfect Lens," Phys. Rev. Lett. 85, 3966–3969 (2000).

[21] J. Brown, "Artificial dielectrics having refractive indices less than unity," Proc. Inst. Electr. Eng. London 100, 51–62 (1953).

[22] N. Engheta, R.W. Ziolkowski, Metamaterials: Physics and Engineering Explorations (Wiley, New York, 2006).

[23] Zhang, Xiang, Liu, Zhaowei. “Superlenses to overcome the diffraction limit”. Nature Materials 7, 435 - 441 (2008).

[24] Dürig, U., Pohl, D. W. & Rohner, F. Near-field optical-scanning microscopy. J. Appl. Phys. 59, 3318–3327 (1986).

[25] Yang, H. et al. Super-resolution biological microscopy using virtual imaging by a microsphere nanoscope. Small 10, 1712–1718 (2014).

[26] Jacob, Z., Alekseyev, L. V. & Narimanov, E. Optical hyperlens: far-field imaging beyond the diffraction limit. Opt. Express 14, 8247–8256 (2006).

[27] E. T. F. Rogers, J. Lindberg, T. Roy, S. Savo, J. E. Chad, M. R. Dennis, and N. I. Zheludev, “A super-oscillatory lens optical microscope for subwavelength imaging,” Nat. Mater. 11(5), 432–435 (2012).

[28] Berry, M. V. & Dennis, M. R. Natural superoscillations in monochromatic waves in D dimensions. J. Phys. A: Math. Theor. 42, 022003 (2009).

[29] Rogers, E. T. F. & Zheludev, N. I. Optical super-oscillations: sub-wavelength light focusing and super-resolution imaging. J. Opt. 15, 094008 (2013).

[30] Huang, F. M. et al. Focusing of light by a nanohole array. Appl. Phys. Lett. 90, 091119 (2007).

[32] Slepian, D. & Pollak, H. O. Prolate spheroidal wave functions, fourier analysis and uncertainty—I. Bell Syst. Tech. J. 40, 43–63 (1961).

[31] Lin, J. et al. New hybrid genetic particle swarm optimization algorithm to design multi-zone binary filter. Opt. Express 24, 10748–10758 (2016).

[33] Huang, F. M. & Zheludev, N. I. Super-resolution without evanescent waves. Nano Lett. 9, 1249–1254 (2009).

[34] Beruete, Miguel & Navarro-Cia, Miguel & Sorolla Ayza, Mario & Campillo, Igor. (2008). Planoconcave lens by negative refraction of stacked subwavelength hole arrays. Optics express. 16. 9677-83. 10.1364/OE.16.009677.

[35] Orazbayev, Bakhtiyar & Beruete, Miguel & Navarro-Cia, Miguel. (2015). Wood zone plate fishnet metalens. EPJ Applied Metamaterials. 2. 8. 10.1051/epjam/2015014.

[36] V. Pacheco-Peña B. Orazbayev V. Torres M. Beruete M. Navarro-Cia "Ultra-compact planoconcave zoned metallic lens based on the fishnet metamaterial" Appl. Phys. Lett. vol. 103 pp. 183507-1-12 2013.

[37] M. Navarro-Cía, M. Beruete, M. Sorolla, and I. Campillo, Appl. Phys. Lett. 94. 144107 (2009).

[38] Wen, Z. Q. et al. Super-oscillation focusing lens based on continuous amplitude and binary phase modulation. Opt. Express 22, 22163–22171 (2014).

[39] He, Y. H. et al. Double-layer metallic holes lens based on continuous modulation of phase and amplitude. IEEE Photonics Technol. Lett. 26, 1801–1804 (2014).

[40] Rogers, E. T. F. et al. Super-oscillatory optical needle. Appl. Phys. Lett. 102, 031108 (2013).

[41] Yuan, G. H. et al. Planar super-oscillatory lens for sub-diffraction optical needles at violet wavelengths. Sci. Rep. 4, 6333 (2014).

[42] Chen, Gang & Wen, Zhongquan & Qiu, Cheng-Wei. (2019). Superoscillation: from physics to optical applications. Light: Science & Applications. 8. 56. 10.1038/s41377-019-0163-9.

[43] Wang, T. T. et al. Experimental verification of the far-field subwavelength focusing with multiple concentric nanorings. Appl. Phys. Lett. 97, 231105 (2010).

[44] Rogers, E. T. F. et al. A super-oscillatory lens optical microscope for subwavelength imaging. Nat. Mater. 11, 432–435 (2012).

[45] Li, M. Y. et al. Controllable design of super-oscillatory lenses with multiple sub-diffraction-limit foci. Sci. Rep. 7, 1335 (2017).

[46] Chen, G. et al. Super-oscillatory focusing of circularly polarized light by ultralong focal length planar lens based on binary amplitude-phase modulation. Sci. Rep. 6, 29068 (2016).

[47] Wan, X. W., Shen, B. & Menon, R. Diffractive lens design for optimized focusing. J. Opt. Soc. Am. A 31, B27–B33 (2014).

[48] Chen, G. et al. Super-oscillation far-field focusing lens based on ultra-thin width-varied metallic slit array. IEEE Photonics Technol. Lett. 28, 335–338 (2016).

[49] Chen, G. et al. Far-field sub-diffraction focusing lens based on binary amplitude-phase mask for linearly polarized light. Opt. Express 24, 11002–11008 (2016).

[50] He, Y. H. et al. Double-layer metallic holes lens based on continuous modulation of phase and amplitude. IEEE Photonics Technol. Lett. 26, 1801–1804 (2014).

[51] Huang, K. et al. Ultrahigh-capacity non-periodic photon sieves operating in visible light. Nat. Commun. 6, 7059 (2015).

[52] M.G. Silveirinha, A. Alú, B. Edwards, and N. Engheta, "Overview of theory and applications of epsilon-near-zero materials," URSI General Assembly (Chicago, IL, 2008).

[53] Pendry, J. B.; Holden, a. J.; Robbins, D. J.; Stewart, W. J. Magnetism from conductors and enhanced nonlinear phenomena. *IEEE Trans. Microwave Theory Tech.* 1999, 47, 2075-2084.

[54] J. Kennedy and R. Eberhart, "Particle swarm optimization," in Proc. IEEE Int. Conf. Neural Networks, 1995, vol. 4, pp. 1942–1948.

[55] J. Robinson and Y. Rahmat-Samii, "Particle swarm optimization in electromagnetics," IEEE Trans. Antennas Propag., vol. 52, no. 2, pp. 397–407, Feb. 2004.

[56] D. Gies and Y. Rahmat-Samii, "Particle swarm optimization for reconfigurable phase-differentiated array design," Microwave Opt. Technol. Lett., vol. 38, no. 3, pp. 172–175, Aug. 2003.

[57] J. Kennedy and R. Eberhart, «Particle Swarm Optimization». Proceedings of IEEE International Conference on Neural Networks, 1995, Vol. IV: 1942–1948.

[58] M. Gen, R. Cheng. "Genetic Algorithms and Engineering Design". Wiley, New York (2000)

[59] S. Shadrokh, F. Kianfar. "A genetic algorithm for resource investment project scheduling problem, tardiness permitted with penalty". Eur. J. Oper. Res., 181 (2007), pp. 86-101.

[60] C.B.B. Costa, M.R.W. Maciel, R.M. Filho. "Factorial design technique applied to genetic algorithm parameters in a batch cooling crystallization optimization". Comput. Chem. Eng., 29 (2005), pp. 2229-2241.

[61] A.A. Najafi, S.T.A. Niaki, M. Shahsavar. "A parameter-tuned genetic algorithm for the resource investment problem with discounted cash flows and generalized precedence relations". Comput. Oper. Res., 36 (2009), pp. 2994-3001.

[62] R. Roy. "A Primer on the Taguchi Method". Society of Manufacturing Engineers, New York (1990).

[63] S.H.A. Rahmati, V. Hajipour, S.T.A. Niaki. "A soft-computing Pareto-based meta-heuristic algorithm for a multi-objective multi-server facility location problem". Appl. Soft Comput., 13 (2013), pp. 1728-1740.

[64] T. Weiland, "A discretization method for the solution of Maxwell's equations for sixcomponent Field," Int. J. Electron. Commun., vol. 31, no. 3, pp. 116–120, 1977.

[65] I. Jaúregui (2016), "Design of terahertz sensors based on metasurfaces for fungal infection detection" (Graduation thesis), Universidad Pública de Navarra, Pamplona.

[66] “CST HELP”. Available: CST STUDIO SUITE 2016\Online\help\cststudio_suite_help.htm

[67] Ghanshyam Singh, “Device modelling and circuit simulation”, September 16, 2013. [SlideShare Presentation]. Available: https://es.slideshare.net/gkdelhi8/photolithography-26223763 [Accessed: 8-May-2017].

[68] M. Navarro-Cia, S. A. Kuznetsov, M. Aznabet, M. Beruete, F. Falcone, and M. S. Ayza, “Route for bulk millimeter wave and terahertz metamaterial design,” IEEE J. Quantum Electron, vol. 47, no. 3, pp. 375–385, Mar. 2011.

[69] Born, M.;Wolf, E. Principles Of Optics, 7th ed.; Cambridge University Press: New York, NY, USA, 1999.

[70] Huang, K.; Qin, F.; Liu, H.; Ye, H.; Qiu, C.W.; Hong, M.; Luk’yanchuk, B.; Teng, J. Planar Diffractive Lenses: Fundamentals, Functionalities, and Applications. Adv. Mater. 2018, 30, 1–22.

[71] Scheuer, J. Metasurfaces-based holography and beam shaping: Engineering the phase profile of light. Nanophotonics 2017, 6, 137–152.

[72]. Fang, N.; Lee, H.; Sun, C.; Zhang, X. Sub-diffraction-limited optical imaging with a silver superlens. Science 2005, 308, 534–537.

[73] Lee, J.Y.; Hong, B.H.; Kim, W.Y.; Min, S.K.; Kim, Y.; Jouravlev, M.V.; Bose, R.; Kim, K.S.; Hwang, I.-C.;Kaufman, L.J.; et al. Near-field focusing and magnification through self-assembled nanoscale spherical lenses. Nature 2009, 460, 498–501.

[74] Wang, Z.; Guo, W.; Li, L.; Luk’yanchuk, B.; Khan, A.; Liu, Z.; Chen, Z.; Hong, M. Optical virtual imaging at 50 nm lateral resolution with a white-light nanoscope. Nat. Commun. 2011, 2, 218.

[75] Pacheco-Peña, V.; Beruete, M.; Minin, I.V.; Minin, O.V. Terajets produced by dielectric cuboids. Appl. Phys. Lett. 2014, 105, 084102.

[76] Mansfield, S.M.; Kino, G.S. Solid immersion microscope. Appl. Phys. Lett. 1990, 57, 2615.

[77] Leggett, A.J. How the result of a measurement of a component of the spin of a spin -1/2 particle can turn out to be 100. Phys. Rev. Lett. 1988, 60, 1351–1354.

[78] Huang, F.M.; Zheludev, N.I. Super-resolution without evanescent waves. Nano Lett. 2009, 9, 1249–1254.

[79] Rogers, E.T.F.; Lindberg, J.; Roy, T.; Savo, S.; Chad, J.E.; Dennis, M.R.; Zheludev, N.I. A super-oscillatory lens optical microscope for subwavelength imaging. Nat. Mater. 2012, 11, 432–435.

[80] Yuan, G.H.; Rogers, E.T.; Zheludev, N.I. Achromatic super-oscillatory lenses with sub-wavelength focusing. Light Sci. Appl. 2017, 6, e17036.

[81] Liu, T.; Tan, J.; Liu, J.; Wang, H. Vectorial design of super-oscillatory lens. Opt. Express 2013, 21, 15090–15101.

[82] Chen, G.;Wu, Z.; Yu, A.; Zhang, K.;Wu, J.; Dai, L.;Wen, Z.; He, Y.; Zhang, Z.; Jiang, S.; et al. Planar binaryphase lens for super-oscillatory optical hollow needles. Sci. Rep. 2017, 7, 1–10.

[83] Rogers, E.T.F.; Zheludev, N.I. Optical super-oscillations: Sub-wavelength light focusing and super-resolution imaging. J. Opt. 2013, 15, 094008.

[84] Huang, K.; Ye, H.; Teng, J.; Yeo, S.P.; Luk'yanchuk, B.; Qiu, C.-W. Optimization-free superoscillatory lens using phase and amplitude masks. Laser Photon. Rev. 2014, 8, 152–157.

[85] Tseng, M.L.; Hsiao, H.H.; Chu, C.H.; Chen, M.K.; Sun, G.; Liu, A.Q.; Tsai, D.P. Metalenses: Advances and Applications. Adv. Opt. Mater. 2018, 6, 1–16.

[86] Pacheco-Peña, V.; Engheta, N.; Kuznetsov, S.; Gentselev, A.; Beruete, M. Experimental Realization of an Epsilon-Near-Zero Graded-Index Metalens at Terahertz Frequencies. Phys. Rev. Appl. 2017, 8, 034036.

[87] Orazbayev, B.; Beruete, M.; Pacheco-Peña, V.; Crespo, G.; Teniente, J.; Navarro-Cía, M. Soret Fishnet Metalens Antenna. Sci. Rep. 2015, 4, 9988.

[88] Pacheco-Peña, V.; Orazbayev, B.; Torres, V.; Beruete, M.; Navarro-Cía, M. Ultra-compact planoconcave zoned metallic lens based on the fishnet metamaterial. Appl. Phys. Lett. 2013, 103, 183507.

[89] Jin, N.; Rahmat-Samii, Y. Advances in Particle Swarm Optimization for Antenna Designs: Real-Number, Binary, Single-Objective and Multiobjective Implementations. IEEE Trans. Antennas Propag. 2007, 55, 556–567.

[90] E. T. F. Rogers, J. Lindberg, T. Roy, S. Savo, J. E. Chad, M. R. Dennis, N. I. Zheludev, Nature Materials, (5), pp-432-435, March 2012.

[91] E. T. F. Rogers, and N. I. Zheludev, Journal of Optics, (15), pp-094008-1-23, 2013.

[92] G. Yuan, E. T. F. Rogers, T. Roy, Z. Shen and N. I. Zheludev, Optics Express, (22), pp-6428-6437.

[93] B. Orazbayev, M. Beruete, V. Pacheco-Peña, G. Crespo, J. Teniente, M. Navarro-Cía, "Soret fishnet metalens antenna", Sci. Rep. 4 (2015), 9988.

[94] Kennedy, J.; Eberhart, R.C. A discrete binary version of the particle swarm algorithm. In Proceedings of the 1997 IEEE International Conference on Systems, Man, and Cybernetics, Computational Cybernetics and Simulation, Orlando, FL, USA, 12–15 October 1997; Volume 5, pp. 4104–4108.

[95] D. R. Smith, J. J. Mock, A. F. Starr, and D. Schurig, "Gradient index metamaterials", Phys. Rev. E 71, 036609 (2005).

[96] R. Liu, Q. Cheng, J. Y. Chin, J. J. Mock, T. J. Cui, and D. R. Smith, "Broadband gradient index microwave quasi-optical elements based on non-resonant metamaterials", Opt. Express 17, 21030–21041 (2009).

[97] O. Paul, B. Reinhard, B. Krolla, R. Beigang, and M. Rahm, "Gradient index metamaterial based on slot elements", Appl. Phys. Lett. 96, 241110 (2010).

[98] J. Neu, B. Krolla, O. Paul, B. Reinhard, R. Beigang, and M. Rahm, "Metamaterial-based gradient index lens with strong focusing in the THz frequency range," Opt. Express 18, 27748-27757 (2010).

[99] N. I. Landy, S. Sajuyigbe, J. J. Mock, D. R. Smith, andW. J. Padilla, “Perfect metamaterial absorber,” Phys. Rev. Lett. 100, 207402 (2008).

[100] G. Yuan, K. Rogers, E. T. F. Rogers, and N. I. Zheludev, "Far-field Metamaterial Superlens," in Conference on Lasers and Electro-Optics, OSA Terchnical Digest (online) (Optical Society of America, 2018), paper FM3J.2.

[101] W.Li, P. He, W. Yuan and Y. Yu, “Efficiency-enhanced and sidelobe-suppressed super-oscillatory lenses for sub-diffraction-limit fluorescence imaging with ultralong working distance”, Nanoscale, 2020,12, 7063-7071.

[102] Jing Wu, Zhixiang Wu, Yinghu He, Anping Yu, Zhihai Zhang, Zhongquan Wen, and Gang Chen, "Creating a nondiffracting beam with sub-diffraction size by a phase spatial light modulator," Opt. Express 25, 6274-6282 (2017).

6. Author's merits

Journal Papers

(Invited) **Legaria, S.**; Pacheco-Peña, V.; Beruete, M. "Super-Oscillatory Metalens at Terahertz for Enhanced Focusing with Reduced Side Lobes". Photonics 2018, 5, 56.

International Conferences

S. Legaria, V. Pacheco-Peña, M. Beruete, "Performance enhancement of binary Fresnel lenses using metamaterials", The 11th International Congress on Engineered Material Platforms for Novel Wave Phenomena, Metamaterials 2017, Marseille, (2017). Oral presentation.

National Conferences

S. Legaria, V. Pacheco Peña, JM. Escudero, M. Beruete, "Perfeccionamiento de lentes binarias de Fresnel utilizando metamateriales", XXXII Simposium Nacional de la Unión Científica Internacional de Radio, URSI 2017, Cartagena (2017). Oral presentation.

Academic merits

Bachelor's degree in Engineering in Telecommunication Technologies (UPNA, 2017) with Extraordinary End of Studies prize upon graduation.

Currently finishing the Master's in Telecommunications Engineering.

7. Annex I: CST Templates

For the simulation of the different unit cells used in this work, the template "periodic structures" inside the "MW & RF & Optical" section is chosen. The workflow selected is "Phase Reflection Diagram" inside "Frequency Selective Surfaces (FSS), metamaterial – unit cell". With this template, the following simulation parameters and conditions are considered:

-Template: FSS - Unit Cell / Units: mm, GHz / Frequency range: 0 to 150GHz
-Solver: Frequency Domain Solver / Meshing: tetrahedral meshing
-Background: vacuum
-Boundary conditions: E_t=0 (X_{min} and X_{max}), H_t=0 (Y_{min} and Y_{max}) and open (Z_{min} and Z_{max}).
-No simmetry planes /ports 1 and 2 with no shielding and number of ports equal to one.

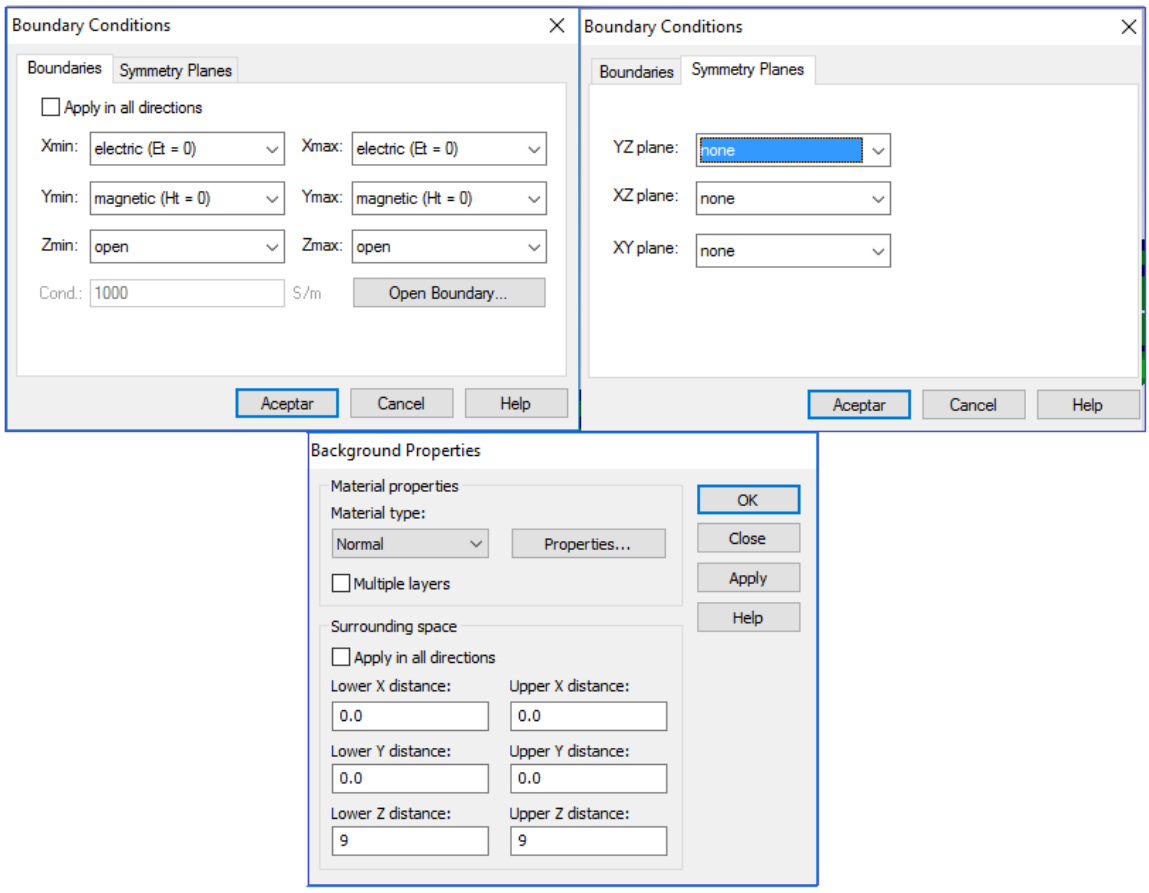

Figure 2.1. Simulation settings for the different unit cells analyzed

It can be observed from Fig. 2.1 that boundary conditions are defined to expedite calculations. The exciting signal is a plane wave vertically polarized. After simulation, a templated based post processing is applied to retrieve the Scattering parameters (S_{11}, S_{21}) and to extract the material properties (μ_{eff}, ε_{eff}, n …).

For simulating the electrically large elements (full lenses and cylindrical approximation lenses), the template "periodic structures" inside the "MW & RF & Optical" section is selected. The workflow chosen is "Metamaterial – full structure". With this template, the following simulation parameters are considered:

-Template: Metamaterial – full structure / Units: mm, GHz / frequency range: 0 - 150GHz
-Solver: Time Domain Solver
-Meshing: hexaedral meshing
-Background: vacuum

-Boundary conditions: E_t=0 (X_{min} and X_{max}) and H_t=0 (Y_{min} and Y_{max}), open add space (Z_{min} and Z_{max}).
- Given the two-fold symmetry of the problem, electric and magnetic symmetries were imposed in the *xz*-plane ($y = 0$) and *yz*-plane ($x = 0$), respectively, to reduce computation time.
-ports 1 and 2 with no shielding and number of ports equal to one.

After the preliminary adjustments are done, the simulation is ready to start. The most important stages once the simulation is started are listed below:

(i) Analyzing port domains: During this first step, the port regions are analyzed for the port mesh adaptation to follow.

(ii) Port mode calculation: Here, the port modes are calculated during the port mesh adaptation. This step is performed several times for each port until a defined accuracy value or a maximum number of passes has been reached.

(iii) Calculating matrices: Processing CAD model: During this step, the input model is checked and processed.

(iv) Calculating matrices: Computing coefficients: During this step, the system of equations which will subsequently be solved is set up.

(v) Data rearrangement: Merging results: For larger models the matrices are calculated in parallel and the results are merged at the end.

(vi) Transient analysis (1): Calculating port modes: In this step, the solver calculates the port mode field distributions and propagation characteristics as well as the port impedances if they have not been previously calculated. This information will be used later in the time domain analysis of the structure.

(vii) Transient analysis (2): Processing excitation: During this stage, an input signal is fed into the stimulation port. The solver then calculates the resulting field distribution inside the structure as well as the mode amplitudes at all other ports. From this information, the frequency dependent S-parameters are calculated in a second step using a Fourier transformation.

(viii) Transient analysis (3): Transient field analysis: After the excitation pulse has vanished, there is still electromagnetic field energy inside the structure. The solver continues to calculate the field distribution and the S-parameters until the energy inside the structure and the port signals has decayed below a certain limit (specified by the Accuracy setting in the solver dialog box). All simulations are executed with accuracy of -50dB and the number of pulses is incremented to 1000 to ensure the simulation runs enough time.

For our unit cell structure, the entire parametric sweep analysis takes only a few minutes to complete while the different full structures simulations took between one and four days, due their relatively large electrical size.

The fields can be recorded at arbitrary frequencies during a simulation. However, it is not possible to store the field patterns at all available frequencies as this would require a tremendous amount of memory. In this work, many E-field and H-field probes are placed along the optical axis, and power flow / E-field monitors are configured at the frequencies of interest.